國立臺灣大學工學院土木工程學系

博士論文

Department or Graduate Institute of Civil Engineering
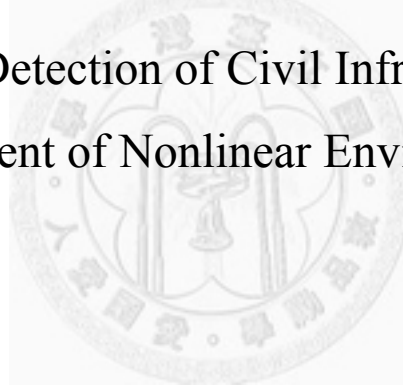
College of Engineering

National Taiwan University

Doctoral Dissertation

土木基礎結構損壞偵測技術：含非線性環境影響之考慮

Damage Detection of Civil Infrastructures

Including Treatment of Nonlinear Environmental Effects

許丁友

Ting-Yu Hsu

指導教授： 羅俊雄 教授

Advisor: Chin-Hsiung Loh, Professor

中華民國 九十九 年 十二 月

December, 2010

ACKNOLEDGEMENTS

ABSTRACT

The objective of this thesis is to develop techniques to localize and quantify damage in civil structures under nonlinear environmental effects. The damage that is aimed at to detect in this thesis is the damage that causes stiffness reduction in a structure.

The modified modal strain energy change (MSEC) method is developed to overcome some difficulties when applying MSEC method to a 3D steel building structure. The modifications include: (i) adding sensitivity equations between eigenvalue and elemental stiffness variation ratios to the damage identification equation which contains only sensitivity equations between MSEC and elemental stiffness variation ratios; (ii) expanding these sensitivity equations from "elemental stiffness variation ratios" to "elemental sectional property variation ratios"; (iii) a new iteration process which updates the targets in every iterating step; (iv) using the non-absolute MSEC ratio while selecting suspected damage elements; (v) using dynamic expansion to obtain mode shapes with complete degree of freedoms (DOFs) from the meausred imcomplete mode shapes; (vi) setting thresholds to avoid elements causing abnormal results. The feasibility of the modified MSEC method is verified through numerical studies and experimental studies.

The frequency response function change (FRFC) method to detect damage locations and extents based on the change of the frequency response functions (FRFs) of a structure under ground excitation is proposed in this thesis. The system matrices of the intact system and the FRFs both prior and posterior to an occurrence of damage are required for the FRFC method. The feasibility of the FRFC method is verified by numerical studies and experimental studies of a 6-story steel building structure with several damage cases.

Besides, an operational scheme for integrating the FRFC method with wireless sensing systems is developed. By imbedding algorithms necessary for the FRFC method into wireless sensing units, the advantage of collocated computing resources of wireless sensing systems is taken effect and at the same time the energy consumed by wireless sensing units is greatly reduced. The on-line automatic damage localization and quantification of the 6-story steel building structure is successfully accomplished.

The feasibility of the local flexibility method (LFM) to detect damage of a shear-type low-rise building structure and a flexible high-rise building structure is studied with numerical and experimental cases. The comparison of using flexibility matrices constructed by two different algorithms to detect damage using the LFM is also conducted.

The stiffness variation of the structural components is identified from the measured data within a short duration where environmental factors are assumed nearly constant. In practice, the stiffness variations identified at different time fragments always fluctuate with environmental factors. The stiffness variation caused by damage may be smeared by these environmental effects. A new method which deals with environmental effects on the identified damage extent of each component without measuring the environmental factors is proposed, especially for nonlinear environmental effects. This is achieved by training an auto-associative neural network (AANN) to perform nonlinear principal component analysis (NPCA) to extract the underlying environmental trend. Then the damage extent can be estimated more accurately by a proposed prediction model.
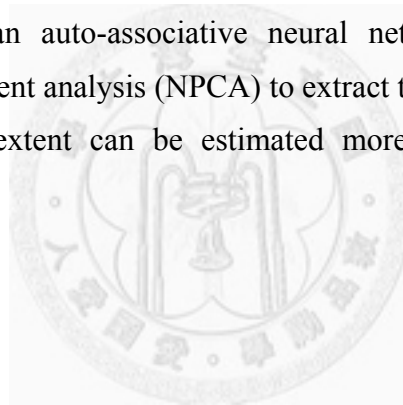
中文摘要

本論文之目標在於發展可偵測土木結構損壞位置與損壞程度的方法，並考慮結構受到環境的非線性影響。本論文所欲偵測之結構損壞係指結構勁度折減之情形。

本論文改進「模態應變能改變法」(modal strain energy change method)，以克服其應用於三維鋼構建築結構所遭遇之困難，改進的部分包括：(1) 於識別方程式中加入特徵值與模態應變能改變之關係，以增加求解識別方程式之數值穩定性；(2) 由偵測「桿件概損程度」擴充至「桿件斷面性質概損程度」；(3) 於每步迭代時根據上一步之結果更新迭代之目標；(4) 利用未取絕對值之模態應變能變化來決定可能的損壞桿件；(5) 利用動力擴展法來擴展自由度不完全之模態形狀；(6) 藉由設置門檻值避免桿件模態應變能過低造成之數值問題。改進後之模態應變能改變法係利用上述三維鋼構建築結構之數值案例與實驗案例進行驗證。

本論文提出「頻率響應函數變化法」(frequency response function change method)來偵測結構損壞的位置與程度，該法須使用的資訊包括結構破壞前受地表激振下之頻率響應函數、破壞後受地表激振下之頻率響應函數，以及結構破壞前之系統矩陣。頻率響應函數變化法係利用六層鋼構建築結構之數值案例與實驗案例進行驗證。

此外，本論文將頻率響應函數變化法與無線感測系統進行整合。將頻率響應函數變化法所需之演算法植入無線感測元件，發揮無線感測系統分散運算之優勢，同時大幅節省無線感測元件之耗電量。此一透過無線感測系統之線上(on-line)自動化偵測損壞位置與損壞程度的概念，已成功應用於上述六層樓鋼構建築結構之實驗案例。

本論文亦探討「局部柔度法」(local flexibility method)應用於建築結構損壞偵測之可行性，其應用案例包括低樓層剪力型建築與高樓層柔性建築之數值模型及上述六層樓鋼構建築結構之實驗案例。此外，亦比較運用兩種不同演算法所得之柔度矩陣於局部柔度法損壞偵測之結果。

在工程實務上，結構損壞偵測必須克服環境影響而造成的困難，因此本論文提出一處理識別之桿件損壞程度受到環境影響的方法，並強調可在不量測環境變數下處理非線性的環境影響。該法係藉由訓練自相關類神經網路(auto-associative neural

network)來進行非線性主成分分析(nonlinear principal component analysis)，以萃取
環境變數的影響方式。之後，藉由所提出之預測模式可更精確的識別桿件損壞程
度。

CONTENTS

LIST OF TABLES

LIST OF FIGURES

1. INTRODUCTION

Structural health monitoring (SHM) makes structures alive by endowing mechanisms with sensing and reacting ability. One of the main purposes of SHM is to monitor the performance of an engineering structure/system under construction or operation. The observed information can be useful to control the construction process, to assist with maintenance of structures, to characterize loads in situ and to validate structural design philosophy/parameters. The other main purpose of SHM is to detect damage. Issuing an alarm before the damage reaches a critical Level-Increases the safety to the public. Detecting damage in its early stage can reduce the costs and down-time associated with repair of damage. This thesis focuses on developing damage detection techniques and mainly relates to the second main purpose of SHM.

Generally, damage detection techniques can be categorized as **global** or **local**. Local techniques concentrate on a small part of the structure due to limited sensing range. The non-destructive testing (NDT) based on eddy currents, magnetic fields, radiography, X-rays *etc.* falls into this category. Because these techniques are often time consuming and expensive, only critical components of a structure are evaluated by NDT with a relatively long period, *e.g.* every 2 years, unless a suspected damaged region has been identified. Other local techniques based on electro-mechanical impedance, guided waves, acoustic emission and local strain *etc.* use relatively small sensors which are possible to be instrumented on part of a structure; hence some critical regions of a structure can be monitored in a continuous way using these local damage detection techniques. On the other hand, global techniques measure the response of a structure to determine the integrity of the whole structure. While a few researches use response due to static loads, the majority interests in the vibration-based damage detection technique which assumes that local damage may change dynamic response of a whole structure. The damage to a structure may be detected through the variation of the structural features such as eigenfrequencies, modal damping, mode shapes, modal strain energy, frequency response functions (FRFs), stiffness and flexibility matrices, *etc.* A continuous and automatic global monitoring of a structure is usually desired to identify damage in the structure while it is in service as well as after a major event.

Damage detection can be classified as four levels as described in Rytter (1993):

- ➢ Level-I - Detection: Is there damage in the system?
- ➢ Level-II - Localization: Where is the damage in the system?
- ➢ Level-III - Quantification: How severe is the damage?
- ➢ Level-IV - Prediction: What is the remaining service life of the system?

Global damage detection techniques try to detect and to localize the damage of a structure, and to give a roughly idea of how severe is the damage. With the help of localization of damage using global damage detection techniques, local damage detection techniques especially NDT can achieve Level-III damage detection with much less effort and give more information about how severe is the damage. Therefore, global and local damage detection techniques are both necessary and can complement each other. To achieve Level-IV damage detection, estimation of future loading and usually an analytical model are necessary to predict the remaining service life of the system.

1.1. Damage Detection of Civil Structures

Aerospace and offshore oil industries made considerable effort to develop vibration-based damage detection techniques during the late 1970s and early 1980s (Farrar and Doebling 1999). Civil engineering community followed rapidly since the early 1980s. The majority of the literature focuses on bridges, while others concentrate on wind turbines and buildings *etc*. Unlike the successful experience of damage detection on rotary machinery, damage detection of civil structures faces significant challenges due to environmental and condition variability in situ, as well as physical size, diversity and material variability of a civil structure. More efforts are still needed to find a reliable, fast and cost-efficient damage detection technology.

Currently, damage detection methods for civil structures are either visual inspection or NDT methods. Visual inspection is costly, time consuming and affected by subjective judges. NDT methods require that the location of damage is known in advance, and are also costly and time consuming. The time required by these methods makes prompt evaluation of critical civil infrastructures, *e.g.* bridges, hospitals and nuclear power

plants, not possible after a catastrophic event. Unfunctionality or unnecessary closure of these critical civil infrastructures not only impact on economy but also damage the resilience of the disaster area. The period of inspecting the civil structures using these methods is usually several years; hence early warning before collapse of a structure is not possible. Early detection of damage can prevent loss of human life and reduce maintenance costs of civil structures. The need to develop a cost-effective, reliable and real-time damage detection technology is evident for civil engineering community.

1.2.   Environmental Effects in Civil Infrastructure

Many studies had reported that the variations of structural features due to varying environmental conditions can be much larger than those caused by structural damage. The environmental conditions concerned in this section include temperature, humidity, loading conditions, and the change of boundary conditions of structural systems.

Many field tests reported that the temperature was the major factor that affects the eigenfrequencies of structures. Therefore, most of the previous studies were interested in developing the relationship between structural eigenfrequencies and temperature. Generally, as reported by Rohrmann *et al.* (2000) and Askegaard and Mossing (1988), it is believed that temperature change may affect the eigenfrequencies of concrete bridges about 10%. Xia *et al.* (2006) performed an experimental study of a reinforced concrete slab and the result indicated that the eigenfrequencies decrease by 0.13% to 0.23% when temperature increases by $1°C$. The elastic modulus of asphalt is also affected by temperature. Peeters and De Roeck (2001) had reported that the asphalt contributed to the stiffness of the Z-24 Bridge significantly if the temperature was under 0°C and the effect was nonlinear (see Figure 1-1). The nonlinear relationship between Young's modulus of asphalt pavement and temperature was confirmed by an experimental test (Watson and Rajapakse 2000). As for wood, it was also reported by Kullaa (2001) that the eigenfrequencies of wooden bridges were affected by the change of temperature.

The boundary conditions may also be altered during the changing environmental conditions, especially due to the change of temperature. Alampalli (1998) reported that

about 50% to 70% change of eigenfrequencies is observed due to the frozen hinge and roller supports of a bridge. Rushton *et al.* (1999) also reported that even in the warm period, the eigenfrequencies may increase as the expansion joint squeezes because of expanding of decks caused by temperature-raising. The scouring around the bridge piers during the flood caused by hurricanes changes the boundary conditions and affects the dynamic properties of the bridge. The relationship between the structural parameters and the boundary conditions may be nonlinear and remains further studies.

The humidity and the loading conditions including traffic, wind, rainfall, snow, flood *etc.* may affect the dynamic properties of structures. Wood (1992) reported that Concrete bridges in United Kingdom absorbed considerable amount of moisture during damp weather, thus the mass of the bridges increased and the structural eigenfrequencies were altered. Bendat and Piersol (1980) also reported that the bridges absorbed considerable amount of moisture and the mass of bridge increased approximately by 3% to 6%. Sohn *et al.* (1999) believed that approximate 1.6% of mass was increased due to moisture and rainfall in the Alamosa Canyon Bridge in America. However, Peeters and De Roeck (2001) concluded that the humidity had no relation to eigenfrequencies for the Z24-bridge. The effect of humidity to structural features seems to be case-dependent. The experimental study of a RC slab conducted by Xia *et al.* (2006) showed that the eigenfrequencies decrease only by 0.03% when relative humidity increases by 1%. Totally approximately 2% decrease of eigenfrequencies when the relative humidity ranges from 25% to 90%. Besides, Kim *et al.* (1999) reported that the eigenfrequencies of a simply supported bridge decreased by 5.4% due to heavy traffic.

In summary, some of the above mentioned environmental effects on structural parameters have been massively studied, *e.g.* the temperature effect on eigenfrequencies of a RC bridge. The nonlinear environmental effect of temperature on the influence of eigenfrequencies of a RC bridge covered with asphalt had been reported. However, most of the above mentioned studies focus on the environmental effects on eigenfrequencies of a structural system, which is only part of the structural features relating to damage.
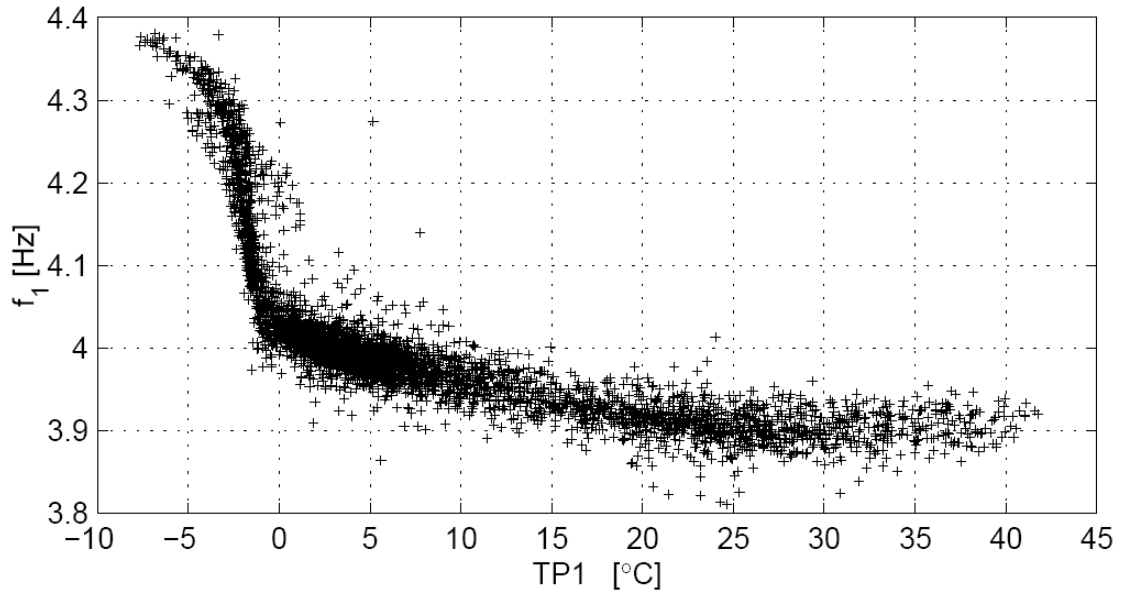
Figure 1-1: The 1st eigenfrequency vs. asphalt layer temperature of the Z24 bridge. (from Peeters and De Roeck 2001).

1.3.   Classification of Vibration-based Damage Detection Techniques

In order to distinguish between damaged and intact structures using measured response, feature extraction is a key process which tries to extract damage-sensitive features from the measurement. According to the properties of extracted structural features, damage detection techniques can be classified as *time-domain*, *frequency-domain* and *modal-domain*.

Time-domain damage detection methods focus on the time-history measured by a variety of sensors, *e.g.* accelerometers and strain-gauges *etc*. Although no information is lost because no converting from time-domain data to frequency-domain or modal-domain data is necessary, usually feature exaction is still conducted. The methods based on empirical mode decomposition, wavelet transform, wave propagation and autocorrelation of time history *etc.* belong to time-domain methods.

Time-domain data can be converted to frequency-domain data using Fourier transform algorithm. Modal-parameters can be extracted in frequency-domain data or directly from time-domain data. As reported by many researchers, the frequency-domain

5

damage detection algorithms may have some advantages over the modal-domain ones. First, the extraction of modal parameters leads to errors and omissions, while there is little loss of information between time and frequency domains (Friswell and Penny 1997). Furthermore, the increased modal density at high frequencies can pose a problem for damage detection (Araujo dos Santos *et al.* 2005). The close modes within a narrow frequency band may not easy to be identified. Second, the FRFs in frequency-domain can provide much more information in a desired frequency range than modal data because modal data are extracted mainly from a very limited number of FRF data round resonance (Lin and Ewins 1994). Third, more equations can be obtained at different frequencies in frequency-domain while the use of modal data usually leads to fewer equations. Consequently, better results may be obtained when the number of unknown parameters or updating parameters is increased (Araujo dos Santos *et al.* 2005).

Probably because eigenfrequencies, damping ratio and mode shapes are easily interpreted than other features extracted in time-domain and frequency-domain, the majority of the damage detection methods in literature belong to the modal-domain. However, as reported by Doebling *et al.* (1996), there is disagreement among researchers about whether the sensitivity of features in modal domain is sufficient or not for damage detection. Since modal information is a reflection of the global system properties while damage is a local phenomenon, some modal-domain features, *e.g.* eigenfrequencies, are not sensitive to damage (Carden and Fanning 2004). Researchers also tried to find a sensitive modal-domain feature, *e.g.* mode shape curvature and modal strain energy (MSE), and to develop corresponding algorithms for damage detection.

Damage detection techniques can also be classified based on the dependence of an analytical model as ***model-based*** and ***non-model-based***, also called parametric and non-parametric, respectively.

Finite element (FE) model updating is one typical model-based damage detection method. The parameters of a model are updated by minimizing the difference between analytical features computed with the model and measured features. Usually, the model-domain features, *e.g.* eigenfrequencies and mode shapes, are used. However, the optimization problem of model updating process is often non-convex, which may result

in a non-uniqueness solution, even though global iterative optimization methods such as coupled local minimizers (Teughels *et al.* 2003) and genetic algorithms (Holland 1975) can help reduce this problem. Furthermore, the use of large number of updating parameters, coupled with limited amount of measured features, may lead to difficulties in convergence of the optimization problem (Carden and Fanning 2004). In addition, the results of the optimization problem may be very sensitive to the measured modal parameters, thus the obtained parameters are consistent with the measured modal data, but they may be unrelated to their true values (Reynders and De Roeck 2010). Another type of model-based methods assume that an analytical model of the structure with acceptable accuracy is obtained, and damage detect can be conducted according to the analytical model. However, as pointed out by Chang *et al.* (2003), availability of data to obtain an accurate analytical model for civil structures is often not possible. Modelling errors of the model-based method are inevitable, which make model-based damage detection of civil structures a challenge.

On the other hand, non-model based damage detection methods do not need a detailed model of the structure; hence the above-mentioned difficulties about optimization problem and modelling errors in model-based methods can be circumvented. Most of the non-model-based damage detection methods are based on changes in eigenfrequencies, mode shapes, mode shape curvatures or dynamically measured flexibilities assembled from the measured modes. However, without the help of an analytical model, the ability to perform Level-III and Level-IV damage detection is limited.

1.4. State-of-the-art of Vibration-based Damage Detection Techniques

Doebling *et al.* (1996) presented an extensive literature review of modal-domain damage detection methods before 1996. Another two profound literature review of global damage detection methods and vibration-based damage detection methods were presented by Sohn *et al.* (2004) and Carden and Fanning (2004), respectively. These reviews gave an overall summary of the state-of-the-art of vibration-based damage

detection methods. Therefore, this chapter only focuses on the discussion of the damage detection methods based on modal strain energy (MSE), frequency response function (FRF), dynamic flexibility matrix and the damage detection methods treating environmental effects.

1.4.1. Methods Based on MSE

Modal strain energy (MSE), *i.e.*, a function of mode shape and elemental stiffness, has been adopted initially as an indicator for modal selection, and has later been considered as a damage indicator. Moreover, the sensitivity of the modal strain energy change (MSEC) with respect to the local damage is derived, and is applied to identify the location and quantity of damage.

Lim and Kashangaki (1994) employed modal strain energy to select the candidate elements before applying the best achievable eigenvectors to detect damage location and magnitude. For an eight-bay space truss structure, only 50 struts among 104 struts had modal strain energy over 1% for the first five modes, therefore the other 54 struts with small MSE were considered undetectable for damage detection.

Doebling *et al.* (1997) employed modal strain energy to select a subset of identified structural vibration modes to be used in FE model correlation and structural damage detection. The results indicate that using the maximum modal strain energy over the entire structure as a criterion provides more accurate update results than using the minimum modal frequency. This phenomenon was explained that the modes that yield the highest value of strain energy are the modes that tend to "stretch" the stiffness matrix the most.

Stubbs and Kim (1996) proposed a damage index based on modal strain energy to locate damage and also to estimate the extent of damage. The feasibility of damage detection using this damage index without baseline modal parameters was also studied, based on the assumption that an analytical model had already been updated to fit the test structure. A two-span continuous aluminum beam with only one damage location was used as the test structure. It was claimed that damage can be localized by using very few

modes by this method, while the damage extent was overestimated.

A two-step modal strain energy change (MSEC) damage detection algorithm was proposed by Shi *et al.* (2000). In the first step, the change in modal strain energy before and after damage was used to locate the damage. Next, the extent of damage was quantified by employing the calculated sensitivities of the modal strain energy based on an analytical model in intact state. The information necessary for this method included the measured mode shapes in damage state, the intact analytical mode shapes, and the intact analytical elemental stiffness matrix. Because the calculation of MSE in each element relied on the analytical mode shapes and analytical elemental stiffness matrix, the MSEC method was evidently a highly model-based method. The MSEC method was applied to a 2-story portal steel frame structure with dense measurement. The results indicated that damage localization and quantification were detected successfully while the quantification of damage was noise-sensitive. The MSEC method was later improved by reducing the modal truncation error in the computation (Shi *et al.* 2002). The modal truncation errors as well as the finite-element modeling error in higher modes were reduced.

1.4.2. Methods Based on FRF

The FRFs had been applied to damage detection for various structures. Wang *et al.* (1997) proposed a damage detection algorithm based on nonlinear perturbation equations of receptance FRF data and applied it to a frame structure. Both an analytical model of structure and FRF data measured prior and posterior to damage for structural damage detection were used. Damage location and extent were detected based on complete measurement of the receptance matrix at many frequencies. Because complete measurement at all DOFs is not possible in practice, analytical receptance matrix at unmeasured DOFs was used. From experimental study of a 3-bay frame structure with two slot cuts, damage location and extent were detected with errors attributed to inaccurate modeling of the joint elements and inaccurate representation of slot cut damage.

Lee and Shin (2002) presented a damage detection algorithm applied to an analytical

cantilever beam and improved the effectiveness with a reduced-domain based method. The dynamic stiffness matrix of the structure in intact state and the FRF data measured from the damaged structure were required for the damage detection algorithm. Experimental studies were conducted for a cantilevered beam with damage caused by introducing three slots of different depths. Damage was fairly well located and quantified, and the effects using different excitation frequency and different measurement DOFs were studied.

Araujo dos Santos *et al.* (2005) proposed a FRF sensitivies based damage detection algorithm to an analytical laminated rectangular plate. The change between measured FRFs and the analytical FRFs of the intact structure were utilized to detect damage locations and extent. The influence of the number of eigenfrequencies and mode shapes used to compute the FRF, as well as the frequency range, the excitation location and the number of measured DOF were studied. The damage detection equations were solved by the bounded-variables least-squares algorithm, and it was claimed that the proposed method presented better results than those obtained when using a technique based on modal data sensitivities.

Furukawa *et al.* (2005) utilized FRFs from a harmonic excitation force to detect damage location and extent. The damage detection equation required the structural parameters of the analytical baseline model and the FRF of the real structure. Both the variation of damping and stiffness of each element were obtained from the damage detection equations, thus Level-III damage detection was achieved. A statistical procedure based on bootstrap method was employed to cope with uncertainty due to measurement noise and modelling errors in the baseline model. This technique was verified by an experimental study on a three-story steel frame structure with damage simulated by removing 2 bracings.

All the above-mentioned FRF-based damage detection approaches must generate artificial vibration by exciters or actuators. Although artificial excitation is controllable and accurate, for a civil engineering structure, it is usually expensive or impractical because of the large scale. Natural excitations such as an earthquake or traffic are free and seem to be a possible alternative provided the amplitude of the ground excitation is much larger than the other excitation sources. Besides, a finite element model is always

required for the FRF-based methods; this makes the FRF-based method highly model-based.

1.4.3. Methods Based on Dynamic Flexibility Matrix

Dynamic flexibility matrix can be computed from the measured data without reference to an analytical model of the structure. It was found as a better indicator for damage localization comparing to eigenfrequencies, damping ratio and mode shapes (Toksoy and Aktan 1994). The location of damage of a reinforced concrete bridge subjected to a progressive damage test was successfully identified by comparing the deflections obtained from a combination of a measured flexibility matrix with a loading before and after damage. Many similar algorithms were proposed and applied to real bridges or beams (Mayes 1995; Aktan *et al.* 1994; Zhang and Aktan 1995). However, the theoretical background of these algorithms was not clear.

Bernal (2002) developed the damage locating vector (DLV) approach based on changes in measured flexibility with solid theoretical background. The damage was localized by finding the null space of the change in flexibility matrix. The physical meaning is that if a load configuration exists for which the displacements before and after damage are the same, the stress caused by the loading are zero in the damaged zones.

The above-mentioned techniques based on dynamic flexibility matrix are valid for damage detection (Level-I) and localization (Level-II), but not for damage quantification (Level-III). Reynders and De Roeck (2010) proposed a local flexibility method (LFM) to not only localize damage but also to quantify damage. A virtual displacement was obtained by combining dynamic flexibility matrix with a virtual load that caused stresses only in a local region. For a linear elastic structure, it was derived that the ratio of a linear combination of the virtual displacements before and after damage equaled to the inverse local stiffness ratio based on the principle of virtual work. Theoretically, this general principle was applicable to any structures. The applicability of LFM was illustrated using beam structures. The LFM was validated by numerical simulation beams, a laboratory beam structure and a real bridge. For a simple supported beam structure with a single damage location, only the lowest mode was enough to

estimate damage accurately. The number of modes needed to detect damage was found dependent on the properties of the structure (boundary conditions, stiffness distribution, *etc*.), density of the measurement grid and the location, type and extension of the damage. One of the advantages of the LFM was that the requirement of mass-normalized mode shapes may be circumvented supposed that the mass of the structure was approximately equally distributed.

1.4.4. Methods Treating Environmental Effects

The damage of structure may be detected through the variation of the structural features such as eigenfrequencies, modal damping, mode shapes, damage indexes, stiffness matrices, *etc*. However, in most of the previous studies, these identified structural features were assumed under a constant environmental or operational condition. Many studies had reported that the variations of structural features due to varying environmental conditions, *e.g.* temperature, humidity, loading conditions, and boundary conditions, can be much larger than those caused by structural damage. The variation of the identified structural features may smear the changes caused by structural damages due to the varying environmental conditions; therefore, cause false damage diagnosis.

There are three situations of damage detection of a structure under environmental effects. The first one is that the structural features are sensitive to environmental factors and the trend of structural features due to change of environmental factors is analogous with the trend of structural features due to damage. The second situation is that the structural features are still sensitive to environmental factors but the trend of structural features due to change of environmental factors is distinct from the trend of structural features due to damage. The third situation is that the structural features are not sensitive to environmental factors but sensitive to damage.

On the other hand, there are three kinds of approaches to detect damage of a structure under environmental effects. The first kind of approach is to establish the correlation between the structural features and the environmental factors; therefore the environmental factors which affect the structural features should be recognized and measured. This approach can solve the first two situations. Peeters and De Roeck (2001)

used a black-box model to describe the variations of eigenfrequencies as a function of temperature. The damage can be detected if the eigenfrequency of the new data exceeds certain confidence intervals of the model. Sohn *et al.* (1999) constructed a linear adaptive model to discriminate the changes of eigenfrequencies due to temperature changes from those caused by structural damage or other environmental effects. These approaches need to measure the varying environmental factors and establish the correlation between the environmental factors and structural features. As mentioned by Yan *et al.* (2005a), these methods face many practical issues. Firstly, the researchers need to define the environmental factors which affect the structural features. Secondly, once the correlation between the environmental factors and the measured features has been established, the failure of any of the sensors that measure the environmental factors may cause problems for structural damage detection afterwards.

The second kind of approach is to extract the trend of the structural features under varying environmental conditions without measuring the environmental factors. This approach can only solve the second situation, *e.g.* it assumes that the variation of structural features due to damage behaves in different manner from those due to varying environmental conditions. Yan *et al.* (2005a) proposed the principal component analysis (PCA) to extract the intrinsic environmental factors, and then adopted the novelty analysis to detect structural damage. This approach is limited to only linear or nearly-linear case, and further expanded to deal with piecewise-linear case (Yan *et al.* 2005b). If the environmental effect is highly nonlinear, Sohn *et al.* (2001) proposed to train an auto-associative neural network (AANN) to perform nonlinear principal component analysis (NLPCA). The existence of damage can then be successfully detected based on outlier analysis. However, these methods are only limited to perform "Level-I" damage detection. Giraldo *et al.* (2006) had further shown that the "Level-II" and "Level-III" damage detection under environmental effect is possible provided that the environmental effects are linear or nearly linear. They applied the technique developed by Caicedo *et al.* (2004) to identify the stiffness of structural components, and a 3-steps technique was proposed to obtain the stiffness loss under nearly linear environmental effect.

The last kind of approach is a special case which deals with mainly the third situation by identifying the features which are sensitive to damage but insensitive to

environmental factors without measuring the environmental factors. Manson (2002) developed a novelty detection method for damage identification of a composite plate with Lamb-wave propagation data. A temperature-insensitive feature was found by projecting the original feature space on to a reduced feature space using minor principal components corresponding to the smallest singular values. Sohn *et al.* (2003) developed a damage detection algorithm based on wavelet transform of lamb wave propagation data to extract features that are less sensitive to temperature variations. However, Note that these techniques which had found the environmental-insensitive structural features were limited to Lamb-wave propagation data of specific thin-plate structures.

1.5.   Remaining Challenges

Based on the review of state-of-the-art of vibration-based damage detection algorithms in the last section, and also some review papers about damage detection and SHM in the literature (Carden & Fanning 2004; Chang *et al.* 2003; Sohn *et al.* 2004; Doebling *et al.* 1996), some remaining challenges for vibration-based damage detection are summarized here.

First of all, no universal algorithm applicable to any type of damage in any type of structure has yet been proposed, which implies the algorithms proposed in the literature are case-dependent. Although many modal-domain approaches were claimed promising for damage localization and quantification for some cases, the sensitivity and measurability of the modal parameter shifts due to localized damage seems still an issue argued in the research community. More efforts are needed to develop algorithms for damage localization and quantification using vibration signals. The Level-IV damage detection, *i.e.* prediction of the remaining service life of the structure, is clear a remaining challenge because little attempt was made in the research community.

One of the objectives of structural health monitoring is to ascertain if damage is present or not based on measured features of a structure, and then take necessary reactions in time. In reality, structures are subject to changing environmental conditions such as temperature, humidity, loading conditions, and boundary conditions *etc.*, as well as

operational conditions such as traffic load and human activities *etc.*, that affect measured signals. For simplicity, the term "environmental condition" in the following content becomes a general term which refers to both environmental conditions and operational conditions. Subtle changes of structural features caused by damage can often be masked by the changes due to these ambient variations of the structure, and then false damage diagnosis may be concluded. In the existing literature, many approaches successfully detect damage of a numerical model under the assumption of a constant environmental condition. Lots of damage detection approaches are verified using laboratory tests where environmental conditions and structural state remains steady. Only a few damage detection approaches are applied to a real structure which is subjected to changing environmental conditions. The unbalance among the amount of algorithms verified by real-structure tests, laboratory tests and numerical simulations implies that the environmental effects is still a challenge to face by the research community. It is also concluded by the above-mentioned review papers that filtering environmental effects from measured features for SHM purpose has not been tackled comprehensively in the literature; therefore the method for damage detection to accommodate environmental conditions needs further investigation.

Cost of sensors has been a limitation on the number of sensors instrumented on a structure. In the past, only one to three accelerometers on a structure was common practice. Today, thanks to new technology and lower price, hundreds of sensors are possible to be instrumented on a single structure. Ultimately, it is foreseeable that sufficient number of sensors on a structure can make global monitoring approach local monitoring, and leads to a greater success in SHM. Follow this trend, wireless sensing technology for SHM becomes an emerging interesting research topic in the last decades which tries to make sensors inexpensive, easy to install and smart. While wireless sensing systems (WSS) eradicates extensive lengths of coaxial wires in a structure, which lower both the cost and labor of installation, the collocated computational resources for processing data in wireless sensing units endow the wireless sensing systems intelligence. However, a summary review of wireless sensing technology (Lynch and Loh 2006) indicates the wireless sensing technology, in some respects, is in its infancy. More research is needed to use the advantage of collocation of computational power of wireless sensing systems.

1.6. Focus and Outline of the Thesis

The objective of this thesis is to develop techniques to localize and quantify damage in civil structures, including the treatment of environmental effects. Similar to the majority in the literatures of vibration-based damage detection, the damage that is aimed at to detect in this thesis is the damage that causes stiffness reduction in a structure. In other words, the methodologies in this thesis are limited to stiffness variation identification.

The main original contributions of the thesis are the following:

➢ A new frequency-domain, Level-III damage detection approach is developed in this thesis, called Frequency Response Function Change (FRFC) method. It is derived from the motion of equations of a linear system subjected to a ground motion both before and after damage. The system matrices of the intact system and the FRFs both prior and posterior to an occurrence of damage are required for the FRFC method. The feasibility of the FRFC method is verified using a 6-story steel building structure with several damage cases in a laboratory. (Hsu and Loh 2009)

➢ An operational scheme for integrating the FRFC method with wireless sensing systems is developed. By imbedding algorithms necessary for the FRFC method into wireless sensing units, the advantage of collocated computing resources of wireless sensing systems is taken effect and at the same time the energy consumed by wireless sensing units is greatly reduced. The on-line damage localization and quantification of the 6-story steel building structure is successfully accomplished.

➢ A new method which deals with environmental effects on the identified damage extent of each component without measuring the environmental factors is proposed, especially for nonlinear environmental effects. This is achieved by training an auto-associative neural network (AANN) to perform nonlinear principal component analysis (NPCA) to extract the underlying environmental trend. Then the damage extent can be estimated more accurately by a proposed prediction model, which is achieved by solving an optimization problem. The

approach is verified using a synthetic bridge model. (Hsu and Loh 2010)

➢ The modified MSEC method is developed by adding sensitivity equations between eigenvalue and elemental stiffness variation ratios to the damage identification equation which contains only sensitivity equations between MSEC and elemental stiffness variation ratios as well as by expanding these sensitivity equations from "elemental stiffness variation ratios" to "elemental sectional property variation ratios". A new iteration process which updates the targets in every iterating step is also proposed. Some difficulties while applying the original and modified MSEC methods to a 3D steel building structure are solved by suggesting the non-absolute MSEC ratio while selecting suspected damage elements, by using dynamic-expanded mode shapes and by setting thresholds to avoid elements causing abnormal results. (Hsu and Loh 2008)

➢ The local flexibility method (LFM) has been successfully applied to detect damage of beam structures and a real bridge (Reynders and De Roeck 2010). Therefore, the feasibility of LFM to detect damage of a shear-type low-rise building and a flexible high-rise building is studied. The comparison of using flexibility matrices constructed by two different algorithms to detect damage using LFM is also conducted. A suggestion is proposed to use one of the algorithms to avoid ill-posed problem while constructing a flexibility matrix. Furthermore, it is also suggested to construct the flexibility matrix for LFM with non-mass-normalized mode shapes using the same algorithm to circumvent the troublesome work of obtaining a mass matrix by establishing a finite element model.

The content of the chapters in this thesis is briefly described here:

Chapter 1: The introduction of SHM and the orientation of vibration-based damage detection in civil structures are described at first. Next, the environmental effects in civil structures in the existing literature are summarized. The classification of damage detection techniques is discussed and the state-of-the-art of the damage detection techniques is summarized, especially the methods based on MSE, FRF and dynamic flexibility matrices as well as the methods treating environmental effects. Finally the remaining challenges of damage detection in civil structures and the focus of this thesis

are derived. The main original contributions and content of the thesis are listed lastly.

Chapter 2: The theoretical basis of the modal identification techniques utilized in this thesis is summarized. The data-driven stochastic subspace identification (SSI) method or combined deterministic-stochastic subspace identification (CSI) method which identifies modal parameters of a structure using output-only or input-output data respectively are described at first. The algorithm to identify stiffness matrices and damping matrices directly from the system matrix and the output matrix identified by SSI or CSI techniques is introduced. The theoretical bases to obtain flexibility matrices from modal parameters based on three different algorithms are summarized. The algorithms to estimate the reliability of the identified mode shapes and to perform expansion and reduction of mode shapes and system matrices are also described.

Chapter 3: The algorithms of damage detection methods are explained in detail. In the first section, the methodologies of the original MSEC method and the proposed modified MSEC method are described. In the second section, the methodology of the proposed FRFC method is introduced. The operational scheme to integrate FRFC method with wireless sensing systems is also presented. Finally, the methodology of the LFM is summarized in the third section.

Chapter 4: The damage detection algorithms introduced in Chapter 3 are verified through numerical and experimental studies. The modified MSEC method is mainly verified by a full-scaled 3-story steel building structure with a damage simulated by cutting the flanges of the columns in the 1st story which made the stiffness reduction ratio of the column different in DOFs. Besides numerical studies, the FRFC method and LFM are mainly verified by a 1/4-scaled 6-story steel building structure with several damage cases simulated by replacing or removing special-designed connecting plates between bracings and floors. The operational scheme for integrating the FRFC method with wireless sensing systems is also realized by imbedding necessary algorithms in wireless sensing units installed in the 1/4-scaled 6-story steel building structure.

Chapter 5: The proposed method to treat environmental effects is presented in this chapter. The methodology of NPCA and the optimization problem for applying the prediction model of NPCA are introduced and the concept is explained using a simple

example. The efficiency of the proposed approach is illustrated using a synthetic bridge model with designated element stiffness reductions and also the element stiffness changes due to varying environmental conditions including temperature, gradient of temperature, humidity and frozen of supports.

Chapter 6: The work done in this thesis is summarized at first. The results derived from the implementation of the methodologies and algorithms in Chapter 4 and Chapter 5 are concluded. Finally, some possibilities for future research in the area of damage detection for civil structures are provided.

2. MODAL IDENTIFICATION TECHNIQUES

Modal identification techniques intend to understand global modal parameters of a structure (*i.e.* eigenfrequencies, damping ratios and mode shapes) from vibration data. Because modal identification is a necessary step for most of the structural health monitoring techniques, the accuracy of identified modal properties becomes an essential issue for SHM of a structure. Classically, an artificial and measurable excitation is inputted to the system and both the input excitation and output responses are measured. From these measurements, the experimental model can be obtained by a variety of parameter estimation methods. Many existing textbooks provide an extensive overview of input-output modal parameter estimation methods (Heylen *et al.* 1997; Ewins 2000; Allemang 1999). However, in the world of civil engineering, it is very difficult and expensive to excite the bridges and buildings to the vibration levels that exceed the vibrations due to traffic or wind. Perhaps except occasional earthquake excitations, one has to rely upon available ambient excitation sources which are practically almost impossible to measure. In this case, the output-only modal analysis (operational modal analysis) is useful to identify the modal parameter of a system. The overview and the application of the output-only modal analysis techniques can be found in (Peeters and De Roeck 2001; Hermans *et. al.* 1999). In the output-only modal analysis, the input is assumed as white noise. This theoretical assumption is not too strict in practical applications as long as the input spectrum is quite flat.

The International Modal Analysis Conference (IMAC) organized a special session with the objective to compare the modal analysis techniques applied to the Z24-Bridge, a three-span reinforced concrete bridge in Switzerland. Three data sets with different types of excitation source including ambient vibration, drop weight and shakers were provided for the research community. Many papers were published by using their preferred methods and excitation types, thus resulted in a fair comparison for different modal analysis algorithms. Based on results of these conference papers, a comparative study of the modal analysis techniques was conducted (Peeters and Ventura 2003). In this paper, both the frequency domain and time domain modal analysis techniques which are usually employed by 6 different research teams are compared. One of the conclusions of this study is that the subspace identification technique applied to all data sets yields the most complete and consistent modal parameter estimates. Beside this

comparative study, another statistical comparative study compared three most popular time-domain output-only modal identification techniques in an entirely automated environment. Both analytical simulated data and experimental acceleration records from a scaled four-story steel frame were used. It was concludes that subspace identification technique is both user friendly and highly robust to sensor noise (Giraldo 2006).

As a result, according to the conclusions above and the author's experience, the subspace identification technique is chosen as the modal identification technique to obtain the modal parameters of the structures in this thesis. Although subspace identification technique is a general name of the approaches which identify the state-space model and involve a singular value decomposition truncation step, the subspace identification method in this thesis mainly refers to the data-driven stochastic subspace identification (SSI) and combined deterministic-stochastic subspace identification (CSI) method summarized in the book (Van Overschee and De Moor 1996). The methodologies to construct the stiffness matrices, damping matrices and flexibility matrices from subspace identification results are also introduced. After the modal parameters of a structure are identified, there can be still a gap between the experimental results and the analytical model of the structure. Therefore, some relating techniques which are helpful for linking experimental and analytical data such as modal assurance criterion (MAC) and mean phase deviation (MPD) of an identified mode shape as well as modal expansion/reduction are also briefly introduced in this chapter.

2.1. Data-Driven Subspace Identification Technique

In the first two subsections in section 2.1, the data-driven stochastic subspace identification technique and combined deterministic and stochastic subspace identification technique summarized in the book (Van Overschee and De Moor 1996) are introduced. The techniques to obtain the stiffness matrices, damping matrices and flexibility matrices of the identified system are also introduced in the last two subsections.

2.1.1. Stochastic Subspace Identification

Consider a n_1 degrees of freedom (DOF) physical system consisting of mass connected through springs and dampers as described by the following matrix differential equation:

$$M\ddot{x}(t) + C_1\dot{x}(t) + Kx(t) = f(t) = B_1u(t) \tag{2-1}$$

where $x(t) \in \mathbb{R}^{n_1}$ is the displacement vector at continuous time t; $M, C_1, K \in \mathbb{R}^{n_1 \times n_1}$ represent the mass, damping and stiffness matrices; A dot over a time function denotes the derivative with respect to time; The vector $f(t) \in \mathbb{R}^{n_1}$ is the excitation force. Afterward the force vector is represented by a vector $u(t) \in \mathbb{R}^{m \times 1}$ describing the m inputs on the DOFs designated according to the transfer matrix $B_1 \in \mathbb{R}^{n_1 \times m}$. Eq. (2-1) can be transformed into the state form:

$$\dot{s}(t) = A_c s(t) + B_c u(t) \tag{2-2}$$

where

$$s(t) = \begin{pmatrix} x(t) \\ \dot{x}(t) \end{pmatrix} \in \mathbb{R}^{n \times 1},$$

$$A_c = \begin{pmatrix} 0 & I_{n_1} \\ -M^{-1}K & -M^{-1}C_1 \end{pmatrix} \in \mathbb{R}^{n \times n} \quad \text{and}$$

$$B_c = \begin{pmatrix} 0 \\ M^{-1}B_1 \end{pmatrix} \in \mathbb{R}^{n \times m}$$

Eq. (2-2) is called state equation, $s(t)$ is the state vector, A_c is the state matrix and B_c is the input matrix. The number $n = 2n_1$ is the order of the system which is also the number of independent elements of the state space vector.

It is always known that not all the DOFs of the system are monitored and assume that there are only l DOFs measured. These sensors can be acceleration, velocity or

displacement types and then the output vector $y(t) \in \mathbb{R}^{l \times 1}$ would be defined:

$$y(t) = C_a \ddot{x}(t) + C_v \dot{x}(t) + C_d x(t) \tag{2-3}$$

where $C_a, C_v, C_d \in \mathbb{R}^{l \times n_1}$ are the output matrices for acceleration, velocity, displacement. The output vector $y(t)$ is related to the state and input vector in state-space from Eq. (2-3):

$$y(t) = Cs(t) + Du(t) \tag{2-4}$$

where

$$C = \begin{bmatrix} C_d - C_a M^{-1} K & C_v - C_a M^{-1} C_1 \end{bmatrix} \in \mathbb{R}^{l \times n} \quad \text{and} \quad D = C_a M^{-1} B_1 \in \mathbb{R}^{l \times m}$$

Eq. (2-4) is called observation equation, C is the output matrix and D is the direct transmission matrix. Since both the input and output data can be measured at discrete time instants only, Eq. (2-2) and Eq. (2-4) should be rewritten as the discrete-time state-space model:

$$\begin{aligned} s_{k+1} &= As_k + Bu_k \\ y_k &= Cs_k + Du_k \end{aligned} \tag{2-5}$$

where

$$A = \exp(A_c \Delta t) \in \mathbb{R}^{n \times n} \quad \text{and} \quad B = [A - I] A_c^{-1} B_c \in \mathbb{R}^{n \times m}$$

A is called the discrete state matrix, B is the discrete input matrix, $s_k = s(k\Delta t)$ is the discrete time state vector, Δt is the sample time and $k \in \mathbb{N}$. Eq. (2-5) is also called deterministic model which means that the input u_k and output y_k can be measured exactly. In fact, it is not possible to measure them without any noise. The approximate way to model the systems is to make some assumption for the noises and take the noises into account for consideration as the following equation which is known as discrete-time combined deterministic-stochastic state-space model:

$$s_{k+1} = As_k + Bu_k + w_k$$
$$y_k = Cs_k + Du_k + v_k \qquad (2\text{-}6)$$

where $w_k \in \mathbb{R}^{n\times 1}$ is the process noise due to disturbances or modelling error and $v_k \in \mathbb{R}^{l\times 1}$ is the measurement noise due to disturbances or sensor error. The noise vectors are both unmeasurable vector signals assumed to be zero mean, white and with covariance matrices:

$$E\left[\begin{pmatrix} w_p \\ v_p \end{pmatrix}\begin{pmatrix} w_q^T & v_q^T \end{pmatrix}\right] = \begin{pmatrix} Q & S \\ S^T & R \end{pmatrix}\delta_{pq} \qquad (2\text{-}7)$$

where E is the expected value operator; δ_{pq} is the Kronecker delta.

Now consider a special case of Eq. (2-6) with no external input ($u_k \equiv 0$). This case is called discrete-time stochastic state-space model:

$$s_{k+1} = As_k + w_k$$
$$y_k = Cs_k + v_k \qquad (2\text{-}8)$$

The main steps to identify the system matrices, $\mathbf{A}$ and $\mathbf{C}$, and the modal parameters of the system from the output measurements $\mathbf{y}_k$ using Stochastic Subspace Identification (SSI) method are given below:

1. Construction of the Hankel matrix: Using output measurement data, the Hankel matrix, $\mathbf{H}$, can be constructed:

$$\mathbf{H} \equiv \left[\begin{array}{cccc} y_0 & y_1 & \cdots & y_{j-1} \\ y_1 & y_2 & \cdots & y_j \\ \cdots & \cdots & \cdots & \cdots \\ y_{i-1} & y_i & \cdots & y_{i+j-2} \\ \hline y_i & y_{i+1} & \cdots & y_{i+j-1} \\ y_{i+1} & y_{i+2} & \cdots & y_{i+j} \\ \cdots & \cdots & \cdots & \cdots \\ y_{2i-1} & y_{2i} & \cdots & y_{2i+j-2} \end{array}\right] \equiv \left[\begin{array}{c} Y_p \\ \hline Y_f \end{array}\right] \in \mathbb{R}^{2li\times j} \qquad (2\text{-}9)$$

where i is a user-defined index and must be larger than the order n of the system. Since there are l DOFs measured, the output vector y_k contains l rows and the matrix H contains $2li$ rows. Here, j corresponds to the number of columns of the Hankel matrix. To ensure all of the r time samples of the output vector y_k populate the Hankel matrix, the number j can be equal to $r - 2i + 1$. According to the expression of Eq. (2-9), the Hankel matrix is divided into the past, $Y_p \in \mathbb{R}^{li \times j}$, and the future, $Y_f \in \mathbb{R}^{li \times j}$, parts.

2. Row space projections: The orthogonal projection of the row space of the matrix Y_p on the row space of the matrix Y_f is defined as O_i^t which can be calculated by the following formula:

$$O_i^t = Y_f \big/ Y_p \equiv Y_f Y_p^T (Y_p Y_p^T)^\dagger Y_p \in \mathbb{R}^{li \times j} \tag{2-10}$$

where " $/$ " denotes the projection operator, ^{T} denotes the transpose operator and † denotes the pseudo-inverse operator. The projection operator can also be computed quickly by using QR-decomposition (Van Overschee and De Moor 1996).

3. Singular value decomposition (SVD) of the orthogonal projection O_i^t: Choose the system order n and split the singular vectors and the singular values in two parts:

$$O_i^t = USV^T = \begin{pmatrix} U_1 & U_2 \end{pmatrix} \begin{pmatrix} S_1 & 0 \\ 0 & S_2 \end{pmatrix} \begin{pmatrix} V_1^T \\ V_2^T \end{pmatrix} \approx U_1 S_1 V_1^T \tag{2-11}$$

in which S_1 contains the first n singular values.

4. Calculate the extended observability matrix, Γ_i :

$$\Gamma_i = U_1 S_1^{1/2} \equiv \begin{bmatrix} C \\ CA \\ \vdots \\ CA^{i-1} \end{bmatrix} \in \mathbb{R}^{li \times n} \tag{2-12}$$

which contains information of the system matrix, A .

5. Calculate the system parameter matrices A and the output matrix C from Γ_i:

$$A = \underline{\Gamma}_i^{\dagger} \overline{\Gamma}_i \tag{2-13}$$

where $\underline{\Gamma}_i \in \mathbb{R}^{l(i-1) \times n}$ denotes Γ_i without the last l rows and $\overline{\Gamma}_i \in \mathbb{R}^{l(i-1) \times n}$ denotes Γ_i without the first l rows. The matrix C can be determined from the first l rows of Γ_i as shown in Eq. (2-12).

6. Calculate the modal parameters of the system: Determine the un-damped eigenfrequencies f_i, the damping ratios ξ_i and the mode shapes φ_i of the structure from the following equations:

$$A = \Psi \Lambda \Psi^{-1}, \quad \Lambda = diag(\lambda_i) \in \mathbb{C}^{n \times n}, \quad i = 1, \dots, n \tag{2-14}$$

$$\lambda_i^c = \ln(\lambda_i) / \Delta t, \quad i = 1, \dots, n \tag{2-15}$$

$$f_i = \left| \lambda_i^c \right| / 2\pi = \omega_i / 2\pi \tag{2-16}$$

$$\xi_i = real(\lambda_i^c) / \left| \lambda_i^c \right|, \quad i = 1, \dots, n \tag{2-17}$$

$$\Phi = C\Psi, \quad \Phi = (\varphi_1 \dots \varphi_n) \tag{2-18}$$

where $|\cdot|$ denotes the taking absolute value; λ_i denotes the discrete-time complex eigenvalue of the ith mode; λ_i^c denotes the continuous-time complex eigenvalue of the ith mode.

2.1.2. Combined Deterministic - Stochastic Subspace Identification

Similar to the discrete-time stochastic state-space model, the discrete-time combined deterministic-stochastic model as shown in Eq. (2-6) can also be used to identify the parameter matrices. It is different from the stochastic model by using not only the

output data y_k but also the input data u_k. Similar to the output Hankel matrix, the input Hankel matrix can be constructed using the input data u_k as:

$$
U \equiv \left[\begin{array}{cccc}
u_0 & u_1 & \cdots & u_{j-1} \\
u_1 & u_2 & \cdots & u_j \\
\cdots & \cdots & \cdots & \cdots \\
u_{i-1} & u_i & \cdots & u_{i+j-2} \\
\hline
u_i & u_{i+1} & \cdots & u_{i+j-1} \\
u_{i+1} & u_{i+2} & \cdots & u_{i+j} \\
\cdots & \cdots & \cdots & \cdots \\
u_{2i-1} & u_{2i} & \cdots & u_{2i+j-2}
\end{array}\right] = \left[\frac{U_p}{U_f}\right] = \left[\begin{array}{cccc}
u_0 & u_1 & \cdots & u_{j-1} \\
u_1 & u_2 & \cdots & u_j \\
\cdots & \cdots & \cdots & \cdots \\
u_i & u_{i+1} & \cdots & u_{i+j-1} \\
\hline
u_{i+1} & u_{i+2} & \cdots & u_{i+j} \\
u_{i+2} & u_{i+3} & \cdots & u_{i+j+1} \\
\cdots & \cdots & \cdots & \cdots \\
u_{2i-1} & u_{2i} & \cdots & u_{2i+j-2}
\end{array}\right] \equiv \left[\frac{U_p^+}{U_f^-}\right] \in \mathbb{R}^{2mi \times j}
$$

(2-19)

where $U_p \in \mathbb{R}^{mi \times j}$ is the past input Hankel matrix and $U_f \in \mathbb{R}^{mi \times j}$ is the future input Hankel matrix. The matrices $U_p^+ \in \mathbb{R}^{m(i+1) \times j}$ and $U_f^- \in \mathbb{R}^{m(i-1) \times j}$ are defined by shifting the border between U_p and U_f one block row down. The shifted output Hankel matrices, $Y_p^+ \in \mathbb{R}^{l(i+1) \times j}$ and $Y_f^- \in \mathbb{R}^{l(i-1) \times j}$, are defined in the same way. The main steps to identify the system matrices, A, C and the modal characteristics from the system input and output measurements are given below:

1. Construction of the Hankel matrices consisting of inputs and outputs as:

$$
Z_p \equiv \left[\frac{U_p}{Y_p}\right] \in \mathbb{R}^{(m+l)i \times j}, \quad Z_p^+ \equiv \left[\frac{U_p^+}{Y_p^+}\right] \in \mathbb{R}^{(m+l+2)i \times j}
$$

(2-20)

2. Compute the oblique projections: The oblique projection of the row space of Y_f along the row space of U_f on the row space of Z_p is defined as O_i^b which can be calculated by the following formula:

$$
O_i^b = Y_f \big/_{U_f} Z_p \equiv (Y_f - Y_f / U_f)(Z_p - Z_p / U_f)^\dagger Z_p \in \mathbb{R}^{li \times j}
$$

(2-21)

3. Singular value decomposition (SVD) of the oblique projection O_i^b: Choose the system order n and split the singular vectors and the singular values in two parts:

$$O_i^t = USV^T = \begin{pmatrix} U_1 & U_2 \end{pmatrix} \begin{pmatrix} S_1 & 0 \\ 0 & S_2 \end{pmatrix} \begin{pmatrix} V_1^T \\ V_2^T \end{pmatrix} \approx U_1 S_1 V_1^T \tag{2-22}$$

4. Calculate the system parameter matrices A, the output matrix C and the modal parameters of the system by Eq. (2-12) to (2-18).

One of the advantages of the state-space description is that the contributions of the different modes to the total response of the system can be easily decoupled. This starts with similarity transform of the system matrix A as:

$$\begin{aligned} s_{k+1}^m &= A s_k^m + B^m u_k \\ y_k &= C^m s_k^m + D u_k \end{aligned} \tag{2-23}$$

where

$$A = \Psi \Lambda \Psi^{-1}, \quad s_k^m = \Psi^{-1} s_k, \quad B^m = \Psi^{-1} B \quad \text{and} \quad C^m = C \Psi .$$

The parametric estimation of the FRF matrix of the system can be calculated from the identified system matrices by taking the Fourier transform of Eq. (2-8) and eliminating the states (Juang 1996) as:

$$H(\omega) = C(zI - A)^{-1} B + D, \quad z = e^{i\omega \Delta t} \tag{2-24}$$

From Eq. (2-4), it is clear that if the measurement outputs are displacement or velocity, the Eq. (2-24) can also be represented in the modal coordinates as:

$$H(\omega) = C^m (zI - \Lambda)^{-1} B^m = \sum_{j=1}^{n} \frac{c_j b_j^m}{z - \lambda_j} = \sum_{j=1}^{n} \frac{\varphi_j b_j^m}{z - \lambda_j}, \quad z = e^{i\omega \Delta t} \tag{2-25}$$

with c_j^m the jth column of C^m and b_j^m the jth row of B^m. If the measurement outputs are accelerations, the Eq. (2-24) can be decoupled as (Reynders and De Roeck, 2010):

$$H(\omega) = C^m \left((zI - \Lambda)^{-1} + (\Lambda - I)^{-1} \right) B^m = \sum_{j=1}^{n} \frac{(z-1)\boldsymbol{\varphi}_j \boldsymbol{b}_j^m}{(\lambda_j - 1)(z - \lambda_j)}, \quad z = e^{i\omega\Delta t} \tag{2-26}$$

For a mechanical system, the receptance matrix $\boldsymbol{H}_r(\omega)$, FRF between nodal displacement and nodal forces, of the measurement grid can be decomposed into the contribution of the different modes as:

$$\boldsymbol{H}_r(\omega) = \sum_{j=1}^{n/2} \frac{q_j \boldsymbol{\varphi}_j \boldsymbol{\varphi}_j^T}{i\omega - \lambda_j} + \frac{\overline{q}_j \overline{\boldsymbol{\varphi}}_j \overline{\boldsymbol{\varphi}}_j^H}{i\omega - \overline{\lambda}_j} \tag{2-27}$$

with $\overline{\bullet}$ the complex conjugate, $\bullet^H$ the Hermitian transpose and q_j the modal scaling factor of mode j. When at least one output DOF measurement coincides with an input DOF, the modal scaling factor can be determined. If the measurement outputs are displacements, the modal decompositions of Eq. (2-25) and Eq. (2-27) should match:

$$\frac{q_j \boldsymbol{\varphi}_j \boldsymbol{\varphi}_{je}^T}{i\omega - \lambda_j} = \frac{\boldsymbol{\varphi}_j \boldsymbol{b}_j^m}{z - \lambda_j}, \quad z = e^{i\omega\Delta t} \tag{2-28}$$

with $\bullet_e$ selecting only the excitation DOFs. If the measurement outputs are velocities, the modal decompositions of Eq. (2-25) should match the modal decomposition of the receptance in Eq. (2-27), weighted by $i\omega$:

$$\frac{q_j i\omega \boldsymbol{\varphi}_j \boldsymbol{\varphi}_{je}^T}{i\omega - \lambda_j} = \frac{\boldsymbol{\varphi}_j \boldsymbol{b}_j^m}{z - \lambda_j}, \quad z = e^{i\omega\Delta t} \tag{2-29}$$

If the measurement outputs are accelerations, the modal decompositions of Eq. (2-26) should match the modal decomposition of the receptance in Eq. (2-27), weighted by $-\omega^2$:

$$\frac{q_j \omega^2 \boldsymbol{\varphi}_j \boldsymbol{\varphi}_{je}^T}{\lambda_j - i\omega} = \frac{\boldsymbol{\varphi}_j \boldsymbol{b}_j^m}{z - \lambda_j}, \quad z = e^{i\omega\Delta t} \tag{2-30}$$

The decomposition procedure is very robust because different modes do not influence each other in the estimation. The modal mass of each mode mm_j can be calculated from (Heylen *et al.* 1997):

$$mm_j = \frac{1}{2q_j i\omega_j}$$

(2-31)

with ω_j the un-damped circular eigenfrequency obtained from Eq. (2-16). This formula also allows the mode shapes φ_i of the structure to be scaled to the mass matrix. Rescaling the mode shapes is performed by putting the modal mass equal to unity.

For a mechanical system under ground excitation, the input vector and the transfer matrix in Eq. (2-1) is $u(t) = \ddot{u}_g(t)$ (for uni-axis ground excitation) and $B_1 = -ML_1$, respectively. The FRF between nodal displacement and ground acceleration of the measurement grid can be decomposed into the contribution of different modes as:

$$H_{x/\ddot{x}_g}(\omega) = \sum_{j=1}^{n/2} \frac{q_j \varphi_j}{i\omega - \lambda_j} + \frac{\bar{q}_j \bar{\varphi}_j}{i\omega - \bar{\lambda}_j}$$

(2-32)

The modal scaling factor can also be determined by comparing Eq. (2-25) and Eq. (2-32) as:

$$\frac{q_j \varphi_j}{i\omega - \lambda_j} = \frac{\varphi_j b_j^m}{z - \lambda_j}, \quad z = e^{i\omega \Delta t}$$

(2-33)

with b_j^m as a scalar for uni-axis ground excitation. However, it should be noted that the mass-normalized mode shape cannot be obtained under ground excitation because the FRF between nodal displacement and ground acceleration under ground excitation is independent of the modal mass.

2.1.3. Determining Stiffness and Damping Matrices

Once the system parameter matrix A and output matrix C have been obtained from

the SSI algorithm or CSI algorithm with output-only data or input-output data, respectively, the system damping and stiffness matrices can also be obtained by the technique proposed by (Xiao *et al.* 2001) for acceleration sensing as:

$$\begin{bmatrix} K & C_1 \end{bmatrix} = -MCR^{-1}, \quad R = \begin{bmatrix} CA^{-2} \\ CA^{-1} \end{bmatrix} \tag{2-34}$$

For velocity sensing or displacement sensing, similar equations in (Xiao *et al.* 2001) can be utilized.

This technique needs a reasonable system mass matrix which can be obtained from the finite element model of the system. However, when the system mass matrix is not available, the mass-normalized system damping and stiffness matrices can also be obtained as (Weng 2010):

$$\begin{bmatrix} KM^{-1} & C_1 M^{-1} \end{bmatrix} = -CR^{-1}, \quad R = \begin{bmatrix} CA^{-2} \\ CA^{-1} \end{bmatrix} \tag{2-35}$$

The mass-normalized system damping and stiffness matrices may be useful for the damage detection if the system mass matrix is assumed unchanged after the system is damaged.

It should be noted that the dimension of the estimated system damping and stiffness matrices equals to the number of the physical modes obtained from the SSI or CSI algorithms. In practice, the higher modes of the structure are not easy to be identified, hence only the lower modes can be identified from the experimental data. As a result, the dimension of the system damping and stiffness matrices are restricted. Moreover, the value of the stiffness matrix is proportion to eigenvalue of A, which means the value in the stiffness matrix is controlled by higher modes with larger eigenvalue. Unfortunately, the accuracy of identified higher modes is generally worse than the one of identified lower modes. As a result, highly reliable stiffness matrix with larger dimension is not easy to access; this also restricts the dimension of the system stiffness matrix even when higher modes are identified from the experimental data.

2.1.4. Determining Flexibility Matrices

Consider the linear physical system in Eq. (2-1) again:

$$M\ddot{x}(t) + C_1\dot{x}(t) + Kx(t) = f(t) \tag{2-36}$$

The orthogonal property of mode shapes with respect to the mass and stiffness matrix leads to

$$\tilde{M} = \boldsymbol{\Phi}^{\mathrm{T}}M\boldsymbol{\Phi} \quad \text{and} \quad \tilde{K} = \boldsymbol{\Phi}^{\mathrm{T}}K\boldsymbol{\Phi} \tag{2-37}$$

where $\tilde{M}$ and $\tilde{K}$ is the mass matrix and stiffness matrix in the modal coordinate, respectively. The square of the un-damped eigenfrequency of the system can be expressed in matrix sense as

$$\omega^2 = \tilde{M}^{-1}\tilde{K} \tag{2-38}$$

Combining Eq. (2-37) and Eq. (2-38) leads to

$$\boldsymbol{\Phi}^{\mathrm{T}}K\boldsymbol{\Phi} - \boldsymbol{\Phi}^{\mathrm{T}}M\boldsymbol{\Phi}\omega^2 = \boldsymbol{0} \tag{2-39}$$

If the mode shapes are already mass-normalized, *i.e.* $\boldsymbol{\Phi}^{\mathrm{T}}M\boldsymbol{\Phi} = \boldsymbol{I}$, then based on Eq. (2-39) the stiffness matrix can be expressed as

$$K = (\boldsymbol{\Phi}^{\mathrm{T}})^{-1}\omega^2\boldsymbol{\Phi}^{-1} \tag{2-40}$$

Therefore, the flexibility matrix can be derived from the relationship between stiffness matrix and flexibility matrix as

$$H = K^{-1} = \boldsymbol{\Phi}\omega^{-2}\boldsymbol{\Phi}^T \tag{2-41}$$

If only the first n modes are available, then the flexibility matrix is truncated. Note that the contribution of the modes in the flexibility is proportional to ω^{-2}, the influence

of the higher modes is much smaller than the one of lower modes.

Before applying Eq. (2-41) to obtain the flexibility matrix, the mode shapes need to be normalized by a known mass matrix. In practice, the mass matrix can be calculated approximately by constructing the numerical model of the structure, *e.g.* a FE model. However, if a non-model based damage detection method is preferred, Eq. (2-41) cannot be used directly. The other way to obtain the flexibility matrix can be achieved by the modal analysis from the measurement directly. This quasi-static flexibility matrix is obtained by evaluating the dynamic flexibility matrix, also called receptance matrix or force-displacement FRF matrix, at zero frequency. The estimation of the quasi-static flexibility matrix can be obtained from force or ambient vibration tests directly, as summarized in (Reynders and De Roeck 2010).

Obtaining Quasi-static Flexibility Matrix from Forced Vibration Tests

Remind Eq. (2-27) again that for a mechanical system, the receptance matrix can be represented as the modal decomposition form as (Heylen *et al.* 1997):

$$H(\omega) \approx H^m(\omega) = \sum_{j=1}^{n} \frac{q_j \varphi_j \varphi_j^T}{i\omega - \lambda_j} + \frac{\overline{q}_j \overline{\varphi}_j \overline{\varphi}_j^H}{i\omega - \overline{\lambda}_j} \tag{2-42}$$

with n the number of measured modes. The quasi-static flexibility matrix can be obtained at $\omega = 0$. The approximation in Eq. (2-42) is due to the fact that the number of measured modes n is limited, *i.e.* the modal truncation takes place. Using the CSI technique described in Section 2.1.2, the quasi-static flexibility matrix can be obtained directly from the force vibration tests. The construction of a finite element model to obtain mass matrix of a structure is not necessary. Note that the mass-normalized mode shapes cannot be obtained in the ground excitation case as described in Section 2.1.2.

Obtaining Quasi-static Flexibility Matrix from Ambient Vibration Tests

Take a Fourier transform of Eq. (2-2) and Eq. (2-4) with considering the displacement

measurement at first, one has the following expression for the receptance matrix:

$$H(0) = -C_d A_c^{-1} B_c \qquad (2\text{-}43)$$

From differentiation of the left equation of Eq. (2-4), it can be shown that (Bernal 2007)

$$H_p B_c = L_2 D \quad \text{with} \quad H_p = \begin{bmatrix} C_d A_c \\ C_d \end{bmatrix} \quad \text{and} \quad L_2 = \begin{bmatrix} I \\ 0 \end{bmatrix} \qquad (2\text{-}44)$$

in case of displacement measurements. Solving this equation for B_c in a least-square sense and substituting the results in Eq. (2-25) yields

$$H(0) = -C_d A_c^{-1} (H_p^T H_p)^{-1} H_p^T L_2 D \qquad (2\text{-}45)$$

If D is diagonal, which is a good assumption for almost all practical cases, and if the structure's mass is approximately equally distributed, one has

$$H(0) = -m H^m(0) \quad \text{with} \quad H^m(0) = C_d A_c^{-1} (H_p^T H_p)^{-1} H_p^T L_2 \qquad (2\text{-}46)$$

Where m is an unknown mass-dependent constant. The eigenvalue decomposition of A_c leads to the state space model in modal coordinates as

$$\dot{s}^m(t) = \Lambda_c s^m(t) + B_c^m u(t) \qquad (2\text{-}47)$$

$$y(t) = \Phi s^m(t) + D u(t) \qquad (2\text{-}48)$$

where

$$A_c = \Psi \Lambda_c \Psi^{-1}, \quad s^m(t) = \Psi^{-1} s(t), \quad B_c^m = \Psi^{-1} B_c$$

Considering the state space model in modal coordinates, $H^m(0)$ can be written as

$$H^m(0) = -\Phi \Lambda_c^{-1} (\Lambda_c^H \Phi^H \Phi \Lambda_c + \Phi^H \Phi)^{-1} \Lambda_c^H \Phi^H \qquad (2\text{-}49)$$

Therefore from only the knowledge of the system poles and the non-mass-normalized mode shapes, $\boldsymbol{H}^m(0)$ can be calculated. If the assumptions of lumped mass and equal mass distribution are not valid, the measured modes could be scaled using the analytical mass matrix.

2.2. Linking Experimental and Analytical Data

2.2.1. Modal Assurance Criterion

The modal assurance criterion (MAC) originally developed at the University of Cincinnati, Structural Dynamics Research Lab (Allemang 1980) is defined as a scalar constant relating the degree of consistency (linearity) between one mode shape and another reference mode shape as follows:

$$MAC_{ij} = \frac{\left|\boldsymbol{\varphi}_i^{H}\boldsymbol{\varphi}_j\right|^2}{\boldsymbol{\varphi}_i^{H}\boldsymbol{\varphi}_i\boldsymbol{\varphi}_j^{H}\boldsymbol{\varphi}_j} \tag{2-50}$$

The modal assurance criterion can be used to verify or correlate an experimental mode shape with respect to an analytical mode shape. This can be done by computing the modal assurance criterion between the mode shapes estimated from experimental data and the mode shapes estimated from a finite element analysis evaluated at common DOFs. This process results in a rectangular modal assurance criterion matrix with values that approach unity whenever an experimental mode shape and an analytical mode shape are consistently related.

2.2.2. Mean Phase Deviation

The mean phase deviation (MPD) algorithm is originally proposed in (Heylen *et al.* 1997). The MPD is a measurement of an identified mode shape about how much a mode shape looks like a straight line cross the zero point. As the components of a mode shape lie closer to the straight line, the mode is closer to a "real" mode. MPD value of a mode

can be thought as the standard deviation of the distances between the modal components and the mean phase of the mode. As a mode is closer to a "real" mode, the MPD of the mode is close to zero.

The main axis of a mode shape is estimated as the mean of the phase of every component of mode m:

$$MP_m = \frac{\sum_{j=1}^{N} w_{jm} \varphi_{jm}}{\sum_{j=1}^{N} w_{jm}} \qquad (2\text{-}51)$$

where

$$\theta_{jm} = \arctan\left(\mathrm{Re}(\varphi_{jm}) / \mathrm{Im}(\varphi_{jm})\right) \quad \text{if} \quad \arctan\left(\mathrm{Re}(\varphi_{jm}) / \mathrm{Im}(\varphi_{jm})\right) \geq 0$$

$$\theta_{jm} = \arctan\left(\mathrm{Re}(\varphi_{jm}) / \mathrm{Im}(\varphi_{jm})\right) + \pi \quad \text{if} \quad \arctan\left(\mathrm{Re}(\varphi_{jm}) / \mathrm{Im}(\varphi_{jm})\right) < 0$$

w_j : a weighting factor (*e.g.* = 1, or = $\left|\varphi_{jm}\right|$)

After the MP is determined, the mean phase deviation (MPD) is estimated as the standard deviation of the difference between the phase of every component and the MP of mode m:

$$MPD_m = \sqrt{\frac{\sum_{j=1}^{N} w_{jm} \tilde{\theta}_{jm}^{2}}{\sum_{j=1}^{N} w_{jm}}} \qquad (2\text{-}52)$$

where $\tilde{\theta}_{jm} = \theta_{jm} - MP_m$. The original algorithm performs very well if the mode shape is close to the real axis and the mode shape is quite "real" (which means the components of a mode shape lie on a straight line cross the zero point). However, this algorithm will estimate a wrong MP if the modes shape is not so real and the main axis of the mode

shape is not close to the real axis, especially when the main axis of a mode shape is close to the imaginary axis. Wrong estimation of MP inevitably induces wrong estimation of MPD using Eq. (2-52).

Because of a unreliable estimation of the MP and MPD could be obtained using the original algorithm as mentioned above, another modified algorithm is proposed. The MP is estimated simply by the curve fitting of a straight line cross the zero by solving MP_m by the following equation in a least square sense:

$$\text{Im}(\tilde{\boldsymbol{\varphi}}_m) = \text{Re}(\tilde{\boldsymbol{\varphi}}_m)\tan(MP_m^R) \tag{2-53}$$

where $\tilde{\boldsymbol{\varphi}}_m = w_{mj}\boldsymbol{\varphi}_{mj}$ and MP_m^R means the mean phase starts from the positive real axis. However, when the main axis of a mode shape is very close to the imaginary axis and the mode shape is not quite "real", the estimation of the MP_m has a numerical problem. This can be easily solved by calculating another mean phase from the imaginary axis as

$$\text{Re}(\tilde{\boldsymbol{\varphi}}_m) = \text{Im}(\tilde{\boldsymbol{\varphi}}_m)\tan(MP_m^I) \tag{2-54}$$

where MP_m^I means the mean phase starts from the positive imaginary axis. Then the final mean phase can be decided by choosing between MP_m^R and MP_m^I with smaller absolute value.

Remember that the mean phase needs to be transformed to the same definition of phase as in the original algorithm, *i.e.* start from the positive imaginary axis with clockwise positive and within 0 to π, before it is used to calculate MPD. If MP_m^I is chosen, then $MP_m = \pi/2 - MP_m^I$. If MP_m^R is chosen and it is minus, then $MP_m = MP_m^I + \pi$.

When calculating the MPD using Eq. (2-52), one needs to be careful not to overestimate the absolute value of $\tilde{\boldsymbol{\theta}}_{jm}$ because sometimes it can be greater than $\pi/2$ or smaller than $-\pi/2$. The following equations should be considered:

$$\tilde{\boldsymbol{\theta}}_{jm} = \boldsymbol{\theta}_{jm} - MP_m - \pi \quad \text{if} \ \ \boldsymbol{\theta}_{jm} - MP_m > \pi/2 \tag{2-55}$$

$$\tilde{\theta}_{jm} = \theta_{jm} - MP_m + \pi \quad \text{if} \quad \theta_{jm} - MP_m < -\pi / 2 \tag{2-56}$$

2.2.3. Expansion and Reduction

When performing damage detection for a structure, sometimes a finite element model is constructed and the damage can be detected according to the finite element model. While a real structure has infinite number of DOF, a finite element model has finite number of DOF. In practice, the number of measured DOF is usually smaller than the number of DOF of the finite element model. However, all the DOF of the mode shape of a finite element model may be necessary to conduct the damage detection. In this case, the measured mode shapes need to be expanded by the modal expansion method (while the reversal way is the modal reduction). Several modal expansion/reduction method, *e.g.* static, dynamic, hybrid and SEREP (System Equivalent Reduction and Expansion Process), had been developed. In this thesis, only static, dynamic and SEREP expansion/reduction methods are implemented and introduced. Note that these expansion and reduction method may also be implemented to expand or reduce the mass matrix and stiffness matrix.

2.2.3.1. Static and Dynamic Expansion and Reduction

The static expansion (Guyan *et al.* 1965) and dynamic expansion (Kidder 1973) are well-known reduction and expansion algorithm. The transform matrix between the master DOFs (measured DOFs) and slave DOFs (unmeasured DOFs) of the static expansion algorithm is

$$\hat{t} = -K_{ss}^{-1} K_{sm} \tag{2-57}$$

where subscript m denotes master DOFs (measured DOFs), and subscript s denotes slave DOFs (unmeasured DOFs). An experimental mode shape with full DOFs can be obtained by expanding a mode shape with incomplete measured DOFs according to the following equation

$$\varphi = \begin{bmatrix} I \\ \hat{t} \end{bmatrix} \varphi_m = \hat{T}\varphi_m \qquad (2\text{-}58)$$

Similarly, the transform matrix between the master DOFs and slave DOFs for the ith mode shape of the dynamic expansion algorithm is

$$\hat{t}_i = -(K - M\omega_i^2)_{ss}^{-1}(K - M\omega_i^2)_{sm} \qquad (2\text{-}59)$$

The ith experimental mode shape with full DOFs can be obtained by expanding the ith experimental mode shape with incomplete measured DOFs according to the following equation

$$\varphi_i = \begin{bmatrix} I \\ \hat{t}_i \end{bmatrix} \varphi_{m,i} = \hat{T}_i \varphi_{m,i} \qquad (2\text{-}60)$$

The static expansion algorithm can also be used inversely to perform reduction of the stiffness matrix and mass matrix as

$$\begin{aligned} M_r &= \hat{T}^T M \hat{T} \\ K_r &= \hat{T}^T K \hat{T} \end{aligned} \qquad (2\text{-}61)$$

2.2.3.2. System Equivalent Reduction and Expansion Process

The System Equivalent Reduction Expansion Process (SEREP) (O'Callahan *et al.* 1989) is a very useful method for modal expansion and reduction. The slave (unmeasured) DOFs of the experimental mode shapes can be expressed according to the reference analytical mode shapes and the master (measured) DOFs of the experimental mode shapes as

$$\Phi_s = \Phi_s^r (\Phi_m^{r\,T} \Phi_m^r)^{-1} (\Phi_m^{r\,T} \Phi_m) \qquad (2\text{-}62)$$

where superscript r denotes reference analytical mode shapes.

3. DAMAGE DETECTION METHODOLOGY

As point out in Section 1.5, the research community of SHM is still investigating the feasibility of damage detection algorithms using change of structural features due to damage. In this chapter, three Level-III vibration-based damage detection algorithms using different strategies are introduced. Similar to the majority in the literatures of vibration-based damage detection, the damage that is aimed at to detect in this thesis is the damage that causes stiffness reduction in a structure. In other words, the methodologies in this thesis are limited to stiffness variation identification.

The first algorithm is the MSEC method originally developed by (Shi *et al.* 2000), classified as a modal-domain, Level-III and highly model-based approach. With the help of a finite element model, detailed damage characteristics could be recognized by this method. The original MSEC method is further modified in this thesis to improve the performance of damage detection in practice.

The second method is the FRFC method developed by the author. This method is classified as a frequency-domain, Level-III and model-based approach. Efforts are devoted to reduce the dependence of a FE model for the FRFC method. One of the advantages of this method is the potential to be integrated with wireless sensing systems. Because only some segments of measured frequency spectra of each sensor are necessary to detect the damage by the FRFC method, the whole measured time-history is not necessary to be transmitted wirelessly. While taking the advantage of collocated computing resources of wireless sensing systems, the energy consumed by wireless sensing units is saved at the same time.

The third one is the local flexibility method developed by Reynders and De Roeck (2010), classified as a modal-domain, Level-III and rarely model-based approach. Because the dynamic measured flexibility matrix is dominated by the lowest modes of a structure which can be easily measured with high reliability comparing to higher modes, this method reveals the feasibility in practice.

These three damage detection algorithms are later verified via numerical and experimental cases in Chapter 4.

3.1. Modal Strain Energy Change Method

The original modal strain energy change method developed by (Shi *et al.* 2000) can both detect the location and extent of the damaged elements. Before quantifying damage extent, the suspected damaged elements need to be selected in advance owing to the nature of the ill-posed problem when solving the inverse problem. Therefore, the first step of MSEC method is to select the candidates based on the ratio of MSEC in each element. The next step is to calculate the damage extent based on its sensitivity to the MSEC in each element. The information necessary for this method includes the measured mode shapes in damage state, the intact analytical mode shapes, and the intact analytical elemental stiffness matrix. Because the calculation of MSE in each element relies on the analytical mode shapes and analytical elemental stiffness matrix, the MSEC method is evidently a highly model-based method.

In order to overcome some difficulties when applying MSEC method to a 3D steel building structure (as introduced in Section 4.1.1), several modifications of the original MSEC method are proposed. The main modifications proposed are: (i) including the sensitivity equations of eigenvalue respect to elemental stiffness change in the damage identification equations; (ii) considering elemental stiffness loss contributed by different elemental sectional properties; and (iii) a new "target-updated" iteration process.

3.1.1. Original Modal Strain Energy Change Method

3.1.1.1. Damage Localization

The basic idea of MSE is the product of the elemental stiffness matrix and the second power of the mode shape component (Doebling *et al.* 1997). For the jth element in the ith mode, the MSE before and after the occurrence of a damage is given by

$$MSE_{ij} = \boldsymbol{\varphi}_i^T \boldsymbol{K}_j \boldsymbol{\varphi}_i \qquad \text{and} \qquad MSE_{ij}^d = \boldsymbol{\varphi}_i^{d,T} \boldsymbol{K}_j \boldsymbol{\varphi}_i^d \qquad \qquad (3\text{-}1)$$

where $\boldsymbol{\varphi}_i$ denotes the ith mode shape of intact state; $\boldsymbol{K}_j$ denotes the intact elemental stiffness of jth element; superscript ^{T} denotes the transpose, and the superscript ^{d}

denotes the damage state. In the modal strain energy of damaged case, MSE_{ij}^d, the stiffness of damaged case K_j^d is approximated by K_j since the damaged stiffness matrix is not known in advance. The MSECR (Shi *et al.* 1998) is defined as

$$MSECR_{ij} = \left| MSE_{ij}^d - MSE_{ij} \right| \Big/ MSE_{ij} \qquad (3\text{-}2)$$

If a total of m modes are considered at the same time, then the average normalized modal strain energy change ratio for the jth element may also be utilized as the damage localization indicator, and it is defined as

$$MSECR_j = \sum_{i=1}^{m} MSECR_{ij} \Big/ MSECR_{i,\max} \Big/ m \qquad (3\text{-}3)$$

which denotes the average of MSECR normalized with respect to the largest value of MSECR for each mode. The MSECR is the damage indicator to select the candidate damaged elements to be quantified the damage extent.

3.1.1.2. Damage Quantification

The MSEC method assumes that damage only affects the stiffness matrix of the system. The relationship between the damaged stiffness matrix of the system K^d and the lump value of the stiffness loss ΔK_j of the jth element after the damage is introduced can be expressed as

$$\boldsymbol{K}^d = \boldsymbol{K} + \Delta\boldsymbol{K} = \boldsymbol{K} + \sum_{j=1}^{L} \Delta\boldsymbol{K}_j = \boldsymbol{K} + \sum_{j=1}^{L} \alpha_j \boldsymbol{K}_j \quad (-1 < \alpha_j \le 0) \qquad (3\text{-}4)$$

where α_j denotes the reduction factor in stiffness of the jth element, and L denotes the total number of elements in the system. The first-order modal strain energy change of jth element in the ith mode due to the variation of mode shape is defined as (Shi *et al.* 1998)

$$MSEC_{ij} = 2\boldsymbol{\varphi}_i^T \boldsymbol{K}_j \Delta\boldsymbol{\varphi}_i = 2\boldsymbol{\varphi}_i^T \boldsymbol{K}_j (\boldsymbol{\varphi}_i^d - \boldsymbol{\varphi}_i) \qquad (3\text{-}5)$$

If the variation of mode shape is assumed to be the linear combination of the mode shapes, then it can be derived from the equation of motion as (Thomas *et al.* 1988)

$$\Delta\boldsymbol{\varphi}_i = -\sum_{r=1}^{n}(\boldsymbol{\varphi}_r^T \Delta \boldsymbol{K} \boldsymbol{\varphi}_i / \lambda_r - \lambda_i)\boldsymbol{\varphi}_r \quad \text{where} \quad r \neq i \tag{3-6}$$

where λ_i denotes the eigenvalue of the ith mode of the intact system. Note that the mode shapes are mass-normalized. Substituting $\Delta\boldsymbol{K}$ in Eq. (3-6) into Eq. (3-5), $MSEC_{ij}$ can be expressed as

$$MSEC_{ij} = -2\boldsymbol{\varphi}_i^T \boldsymbol{K}_j \left(\sum_{r=1}^{n}(\boldsymbol{\varphi}_r^T \Delta \boldsymbol{K} \boldsymbol{\varphi}_i / \lambda_r - \lambda_i)\boldsymbol{\varphi}_r \right) \quad \text{where} \quad r \neq i \tag{3-7}$$

Finally, by substituting Eq. (3-4) into Eq. (3-7), the relationship between $MSEC_{ij}$ and α_j is then obtained

$$MSEC_{ij} = \sum_{p=1}^{L} -2\alpha_p \boldsymbol{\varphi}_i^T \boldsymbol{K}_j \left(\sum_{r=1}^{n}(\boldsymbol{\varphi}_r^T \boldsymbol{K}_p \boldsymbol{\varphi}_i / \lambda_r - \lambda_i)\boldsymbol{\varphi}_r \right) \quad \text{where} \quad r \neq i \tag{3-8}$$

Define the sensitivity coefficient as

$$\beta_{jp} = -2\boldsymbol{\varphi}_i^T \boldsymbol{K}_j \left(\sum_{r=1}^{n}(\boldsymbol{\varphi}_r^T \boldsymbol{K}_p \boldsymbol{\varphi}_i / \lambda_r - \lambda_i)\boldsymbol{\varphi}_r \right) \quad \text{where} \quad r \neq i, \quad j = 1,2,...,J, \quad p = 1,2,...,P.$$

$$\tag{3-9}$$

For the ith mode, the $MSEC_{ij}$ in Eq. (3-8) can be expressed as follows

$$\begin{Bmatrix} MSEC_{i1} \\ MSEC_{i2} \\ ... \\ MSEC_{iJ} \end{Bmatrix} = \begin{bmatrix} \beta_{11} & \beta_{12} & ... & \beta_{1P} \\ \beta_{21} & \beta_{22} & ... & \beta_{2P} \\ ... & ... & ... & ... \\ \beta_{J1} & \beta_{J2} & ... & \beta_{JP} \end{bmatrix} \begin{Bmatrix} \alpha_1 \\ \alpha_2 \\ ... \\ \alpha_P \end{Bmatrix} \tag{3-10}$$

where J denotes the size of the group covering the selected elements for calculating the MSEC, which may or may not include the suspected damaged elements with $J \geq P$,

and P denotes the number of suspected damaged elements.

The vector on the left side of Eq. (3-10) denotes the MSEC of all J elements in the ith mode, which can be calculated from Eq. (3-5) by utilizing the identified mode shapes of the damaged and intact state from measured data. The sensitivity coefficient β_{jp} can be computed from Eq. (3-9) by employing the analytical modal information and elemental stiffness matrices of the intact state. However, the direct solution of Eq. (3-10) would yield poor results owing to the nature of the ill-posed problem, particularly when the data contain noise. Hence, to reduce the effect of the ill-posed problem, the number of suspected damaged elements should be appropriately determined in the previous damage localization stage. Additionally, it is recommended to include several modes when solving Eq. (3-10). The number of equations of Eq. (3-10) increases to dimension of $m \times J$ when m modes are employed to estimate the damage.

3.1.2. Modified Modal Strain Energy Change Method

3.1.2.1. Modification for Damage Localization

The MSECR is originally defined as the absolute change ratio of the MSE of each element for a mode, which implies that the variation of the MSE of the damaged element is bigger than the variation of the other elements both in increasing or decreasing way. However, since damage always makes the damaged element with smaller stiffness value, intuitively, damaged element may deform more under the same load. It was also concluded in the literature that if a structure is damaged at some points, the modal curvatures in the neighborhood of that point tend to increase (Pandey *et al.* 1991; Wahab and De Roeck 1999). These concepts imply that the MSE of damaged elements may increase after damage, not decrease after damage for most of the lower modes. Therefore, in order to select the candidate damaged elements more efficiently with considering difference between increasing and decreasing of MSE, the MSECR is modified as

$$MSECR_{ij} = \left(MSE_{ij}^d - MSE_{ij}\right) / MSE_{ij} \tag{3-11}$$

without taking absolute value in the numerator.

In addition, because the element with a small MSE inevitably leads to an abnormal MSECR value, especially when applied to a 3D structure, a criterion for eliminating the possibility of resulting in an abnormal MSECR is proposed. The jth element in i^{th} mode will be removed if

$$MSE_{ij} < C_{MSE} \big/ L \times \sum_{j=1}^{L} MSE_{ij} \tag{3-12}$$

where C_{MSE} is defined as the threshold of MSE; L is the number of total elements. Another reason to remove the elements of a small MSE is that the corresponding sensitivities of such elements maybe too small, thus producing abnormal results when solving the inverse problem. By setting an appropriate C_{MSE} value, the null hypothesis of damage location and the abnormal results of damage quantification can both be circumvented.

The advantage of modified MSECR and introducing the threshold of MSE will be illustrated in the numerical studies in Section 4.1.2.

3.1.2.2. Including Sensitivity of Eigenvalue

For many cases, the estimation of system eigenfrequencies can be more accurate than the estimation of mode shapes. Therefore, Eq. (3-10) can be expanded to incorporate the change of system eigenvalue together with the MSEC. The sensitivity equation on the variation of eigenvalue can be expressed as (Fox and Kapoor 1968):

$$\Delta\lambda_i = \lambda_i^d - \lambda_i = \boldsymbol{\varphi}_i^T \Delta \boldsymbol{K} \boldsymbol{\varphi}_i = \sum_{p=1}^{P} \alpha_i \boldsymbol{\varphi}_i^T \boldsymbol{K}_p \boldsymbol{\varphi}_i \tag{3-13}$$

This sensitivity equation of eigenvalue is added to Eq. (3-10), where λ_i^d denotes the measured eigenvalue of the ith mode of the damaged system, and λ_i denotes the measured eigenvalue of the ith mode of the intact system. Hence Eq. (3-10) becomes

$$\begin{Bmatrix} \Delta\lambda_i \\ MSEC_{i1} \\ MSEC_{i2} \\ ... \\ MSEC_{iJ} \end{Bmatrix} = \begin{bmatrix} \boldsymbol{\varphi}_i^T \boldsymbol{K}_1 \boldsymbol{\varphi}_i & \boldsymbol{\varphi}_i^T \boldsymbol{K}_2 \boldsymbol{\varphi}_i & ... & \boldsymbol{\varphi}_i^T \boldsymbol{K}_P \boldsymbol{\varphi}_i \\ \beta_{11} & \beta_{12} & ... & \beta_{1P} \\ \beta_{21} & \beta_{22} & ... & \beta_{2P} \\ ... & ... & ... & ... \\ \beta_{J1} & \beta_{J2} & ... & \beta_{JP} \end{bmatrix} \begin{Bmatrix} \alpha_1 \\ \alpha_2 \\ ... \\ \alpha_P \end{Bmatrix} \quad (3\text{-}14)$$

Note that Eq. (3-14) is valid within small disturbance otherwise the truncation error is introduced. Fortunately, the truncation error could be reduced by introducing iteration process which will be explained in detail in Section 3.1.2.4. Moreover, including eigenvalue in Eq. (3-14) adds an equation hence lower the possibility of an ill-posed sensitivity equation. This benefit is discussed in the numerical studies in Section 4.1.2.

3.1.2.3. Expansion of Element Stiffness

Previous studies on damage diagnosis mainly concentrated on the lump value of the damage extent of elements for simplification. In practice, when structure is damaged, equally reduction of stiffness in different DOFs of elements cannot happen unless the element is removed or completely damaged. Furthermore, diverse lump damage extent of an element could be obtained using different directional modes since the damage extent of different DOFs of the elements may be distinct. Consequently, obscure extents of damage of an element are obtained. The original MSEC method is modified further to identify the stiffness loss of elements contributed by different sectional properties.

The stiffness of a beam element is directly related to its sectional properties. By considering the elemental stiffness matrix of the jth element as the combination of stiffness matrices contributed by different sectional properties, the stiffness matrix for the jth element can be expressed as

$$\boldsymbol{K}_j = \boldsymbol{K}_j^A + \boldsymbol{K}_j^{I_z} + \boldsymbol{K}_j^{I_y} + \boldsymbol{K}_j^{I_x} \quad (3\text{-}15)$$

where superscript A denotes the cross sectional area; superscript I_z or I_y denotes the moment of inertia about the local z-axis or y-axis, respectively, and superscript I_x denotes the torsional constant. Accordingly, the variation of the stiffness matrix for the

46

j^{th} element can be expressed as

$$\Delta \boldsymbol{K}_j = \alpha_j^A \boldsymbol{K}_j^A + \alpha_j^{I_z} \boldsymbol{K}_j^{I_z} + \alpha_j^{I_y} \boldsymbol{K}_j^{I_y} + \alpha_j^{I_x} \boldsymbol{K}_j^{I_x} \tag{3-16}$$

Similarly, the MSECR can also be represented by the ratio contributed by different sectional properties of the elements. The reduction factor α_j of the stiffness of the jth element can be expanded as

$$\{\alpha_j\} = \left\{ \alpha_j^A \quad \alpha_j^{I_z} \quad \alpha_j^{I_y} \quad \alpha_j^{I_x} \right\}^T \tag{3-17}$$

Therefore, the $MSEC_{ij}$ contributed by variation of mode shapes with different sectional properties is expressed as

$$2 \left\{ \begin{array}{c} \boldsymbol{\varphi}_i^T \boldsymbol{K}_j^A \Delta\boldsymbol{\varphi}_i \\ \boldsymbol{\varphi}_i^T \boldsymbol{K}_j^{I_z} \Delta\boldsymbol{\varphi}_i \\ \boldsymbol{\varphi}_i^T \boldsymbol{K}_j^{I_y} \Delta\boldsymbol{\varphi}_i \\ \boldsymbol{\varphi}_i^T \boldsymbol{K}_j^{I_x} \Delta\boldsymbol{\varphi}_i \end{array} \right\} \tag{3-18}$$

And the sensitivity coefficient β_{jp} is modified as

$$\begin{bmatrix} \beta_{jp}^{AA} & \beta_{jp}^{AI_z} & \beta_{jp}^{AI_y} & \beta_{jp}^{AI_x} \\ \beta_{jp}^{I_zA} & \beta_{jp}^{I_zI_z} & \beta_{jp}^{I_zI_y} & \beta_{jp}^{I_zI_x} \\ \beta_{jp}^{I_yA} & \beta_{jp}^{I_yI_z} & \beta_{jp}^{I_yI_y} & \beta_{jp}^{I_yI_x} \\ \beta_{jp}^{I_xA} & \beta_{jp}^{I_xI_z} & \beta_{jp}^{I_xI_y} & \beta_{jp}^{I_xI_x} \end{bmatrix} \tag{3-19}$$

in which the typical component of sensitivity coefficient β_{jp} is expressed as

$$\beta_{jp}^{AI_z} = -2\boldsymbol{\varphi}_i^T \boldsymbol{K}_j^A \left(\sum_{r=1}^{n} \frac{\boldsymbol{\varphi}_r^T \boldsymbol{K}_p^{I_z} \boldsymbol{\varphi}_i}{\lambda_r - \lambda_i} \boldsymbol{\varphi}_r \right) \quad \text{where } r \neq i \tag{3-20}$$

where the superscript A and I_z can be replaced by any other combination of A, I_z, I_y, and I_x. Each sensitivity equation of variation of eigenvalue for i^{th} mode and p^{th}

element, $\alpha_i \boldsymbol{\varphi}_i^T \boldsymbol{K}_p \boldsymbol{\varphi}_i$, is also expanded as

$$\left\{\boldsymbol{\varphi}_i^T \boldsymbol{K}_p^A \boldsymbol{\varphi}_i \quad \boldsymbol{\varphi}_i^T \boldsymbol{K}_p^{I_z} \boldsymbol{\varphi}_i \quad \boldsymbol{\varphi}_i^T \boldsymbol{K}_p^{I_y} \boldsymbol{\varphi}_i \quad \boldsymbol{\varphi}_i^T \boldsymbol{K}_p^{I_x} \boldsymbol{\varphi}_i \right\} \left\{ \alpha_i^A \quad \alpha_i^{I_z} \quad \alpha_i^{I_y} \quad \alpha_i^{I_x} \right\}^T \qquad (3\text{-}21)$$

Finally, Eq. (3-17) to (3-21) are substituted into Eq. (3-14) to solve for the stiffness reduction factor of different sectional properties of each element. Similar to the original MSEC method, all the stiffness reduction factor of sectional properties not suspected as being damaged are assumed to be zero, and hence are not considered in Eq. (3-14). Although J can be chosen different from P in Eq. (3-14), for simplicity, the sensitivity coefficients in Eq. (3-14) only relates to the number of suspected damaged elements or sectional properties. Therefore, if there are l suspected damaged elements or sectional properties, the dimension of sensitivity matrix in Eq. (3-14) is $(l+1) \times l$.

3.1.2.4. Iteration Process

Because the relationship between MSEC and damage reduction factor α is nonlinear when sufficient damage has occurred to cause the shift of the system modal information, iteration is necessary to improve the accuracy of the assessment of damage severity. The original MSEC method utilizes an iteration process identical to the one proposed by (Ricles and Kosmatka 1992) to handle the nonlinearity as illustrated in Figure 3-1(a), where the superscripts 0, 1, and 2 refer to the iteration number during updating, and $\boldsymbol{\Omega}_0$ and $\boldsymbol{\Omega}_d$ denote arrays containing modal parameters, including the eigenvalue and MSE of the intact and damaged system, respectively. The difference between $\boldsymbol{\Omega}_0$ and $\boldsymbol{\Omega}_d$ is actually the left side of Eq. (3-14). In the ith step, the stiffness reduction factor array $\boldsymbol{\alpha}^i$ is calculated by Eq. (3-14), which considers the current structural state rather than the intact structural state. Finally, the accumulated stiffness reduction factor array $\boldsymbol{\alpha}$ is obtained by summing up the stiffness reduction factor array $\boldsymbol{\alpha}^i$.

The target of the iteration process is $\boldsymbol{\Omega}_d$, which is assumed to be "fixed" during the iteration. The eigenvalue in $\boldsymbol{\Omega}_d$ is directly measured in the damaged state, which is definitely fixed. However, the other target, MSE in the damaged state, is obtained by expanding the measured damaged mode shape according to the "intact" stiffness matrix.

Hence the MSE remains unchanged during the iteration in the original iteration process. In this thesis, the author proposes to expand the measured damaged mode shape according to the updated "damaged" stiffness matrix based on the results of the previous step, meaning that the target MSE becomes "updated" during the iteration process. Figure 3-1(b) depicts the modified iteration process.

(a) Original iteration scheme

(b) Modified iteration scheme
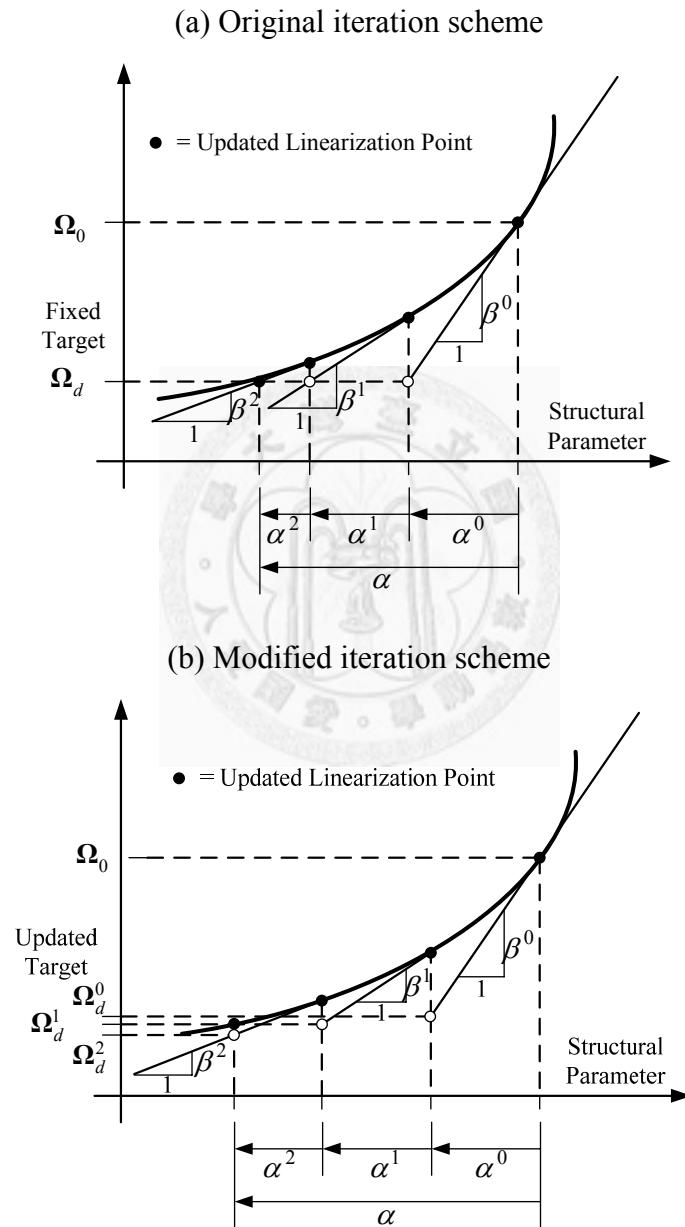
Figure3-1: Iteration process of MSEC method (a) original; (b) modified

3.1.2.5. Convergence Criterion

In practice, the true damage state is unknown. Therefore, a criterion is required to evaluate the results obtained by the modified MSEC method. It is proposed to observe an objective which includes the MAC values between each pair of the measured damaged mode shape and the updated analytical mode shape. The objective is defined as:

$$Ob_i^j = 1 - MAC_i^j \tag{3-22}$$

where MAC_i^j denotes the MAC between the ith measured damaged mode shape and the ith updated analytical mode shape in the jth iteration. The iteration process can be terminated when

$$\sum_{i=1}^{N} Ob_i^j - \sum_{i=1}^{N} Ob_i^{j-1} > 0 \tag{3-23}$$

3.2. Frequency Response Function Change Method

All the FRF-based damage detection approaches summarized in Section 1.4.2 must generate artificial excitations at one or some DOFs on the structure. However, artificial excitations for a civil engineering structure are usually expensive or impractical because of the large scale. Ground excitations powered by an earthquake or traffic seem to be a possible alternative provided the amplitude of the ground excitation is much larger than the other excitation sources.

In this section, the Frequency Response Function Change (FRFC) method which can detect the location and extent of damage is derived from the motion of equations of a linear system subjected to a ground motion both before and after damage. The system matrices of the intact system, *i.e.* mass matrix, damping matrix and stiffness matrix, and the FRFs both prior and posterior to an occurrence of damage are required for the proposed method. This method is classified as a frequency-domain and Level-III damage detection approach. The intact system matrices could be obtained using a finite

element model, which makes the FRFC method model-based. Alternatively, these matrices could be obtained from the measured signals and an analytical mass matrix using the subspace identification technique introduced in Section 2.1.3. Furthermore, for a shear building with a diagonal mass matrix, it is derived that the stiffness reduction ratio can be obtained even though the value in the mass matrix is not known. The circumvention of establishing a FE model to obtain an analytical mass matrix transforms the FRFC method from a highly model-based method to a rarely model-based method.

Experience shows that when solving an inverse problem, poor results could be obtained due to the nature of ill-posed problem, especially when the data are polluted by noise (Fritzen *et al.* 1998). Therefore, a least-squares method is usually implemented and more redundancy is preferred to obtain estimation with better accuracy. Unlike the modal-domain methods where only some identified lower modes can be used, the FRFC method allows plenty of FRFs with different frequencies to be used to solve the inverse problem.

Initially motivated to reduce the cost of sensors instrumented in a structure, wireless sensing technology for SHM becomes an emerging research topic in the last decades. As discussed in Section 1.5, the research community is still trying to discover the potential contributed by computational power collocated in wireless sensing systems. Because the FRFC method requires only some segments of measured frequency spectra of each sensor to detect the damage of a structure, it represents its potential to integrate with the wireless sensing systems to take advantage of collocated computing resources and reduce the energy consumption at the same time. The operational scheme to integrate the proposed FRFC method and wireless sensing systems is also introduced in this section.

3.2.1. Methodology

Let $\ddot{U}(\omega)$ be the Fourier spectrum of the measured ground acceleration vector. The equation of motion with n degrees of freedom under a ground excitation $\ddot{U}(\omega)$ in frequency domain is

$$(-\omega^2 M + i\omega C_1 + K)X(\omega) = -ML\ddot{U}(\omega) \tag{3-24}$$

where $X(\omega)$ is the Fourier spectrum of displacement response vector; M, C_1 and K represents the $n \times n$ mass, damping and stiffness matrices, respectively; L represents the loading vector. The displacement vibration response can be represented as

$$X(\omega) = T(\omega)\ddot{U}(\omega) \tag{3-25}$$

where $T(\omega)$ denotes the frequency response function matrix between the input ground excitation vector and the response displacement vector for the intact system as

$$T(\omega) = -(-\omega^2 M + i\omega C_1 + K)^{-1} ML \tag{3-26}$$

It is assumed that the mass and damping matrices are unchanged after the system is damaged. Therefore the frequency response function matrix $T_d(\omega)$ for the damaged system is

$$T_d(\omega) = -(-\omega^2 M + i\omega C_1 + K_d)^{-1} ML \tag{3-27}$$

where K_d is the stiffness matrix of the damaged structure. Multiply both sides of Eq. (3-26) and Eq. (3-27) by $-\omega^2 M + i\omega C_1 + K$ and $-\omega^2 M + i\omega C_1 + K_d$, respectively. And then subtracts Eq. (3-27) from Eq. (3-26), Eq. (3-28) is obtained as

$$KT(\omega) - K_d T_d(\omega) + (-\omega^2 M + i\omega C_1)(T(\omega) - T_d(\omega)) = 0 \tag{3-28}$$

The change in the stiffness matrix and the change in FRFs due to damage are defined as

$$\Delta K = K_d - K \tag{3-29}$$

and

$$\Delta T(\omega) = T_d(\omega) - T(\omega) \tag{3-30}$$

, respectively. Substituting Eq. (3-29) and Eq. (3-30) into Eq. (3-28) yields the damage identification equation

$$\Delta K T_d(\omega) = (-\omega^2 M + i\omega C_1 + K)\Delta T(\omega) \tag{3-31}$$

Let $R(\omega)$ denotes the right hand side of the damage identification equation as:

$$R(\omega) = (-\omega^2 M + i\omega C_1 + K)\Delta T(\omega) \tag{3-32}$$

Therefore Eq. (3-31) becomes

$$\Delta K T_d(\omega) = R(\omega) \tag{3-33}$$

The term ΔK is the variation of stiffness matrix and can be represented as a sum of each elemental matrix multiplied by a reduction factor ($\Delta K = \sum_{j=1}^{L} \alpha_j K_j$). However, such a representation needs that the element matrices are known or well-updated. In order to circumvent the troublesome model updating procedures to obtain a finite element model with acceptable accuracy, the author tries to solve the variation of element stiffness matrices by only assuming the geometry relationship between the elemental matrices and the system matrix, without assuming the value of each elemental matrix. Considering an one-dimensional shear building with n degrees of freedom for example, the system stiffness matrix is assumed to be the form

$$K = \begin{bmatrix} k_1 + k_2 & -k_2 & & & 0 \\ -k_2 & k_2 + k_3 & & \ddots & \\ & & \ddots & & \\ & \ddots & & k_{n-1} + k_n & -k_n \\ 0 & & & -k_n & k_n \end{bmatrix} \tag{3-34}$$

Because we have specified the form of the stiffness matrix, the left hand side of Eq. (3-33) can be rearranged to allow the variation of elemental stiffness components to be assembled in a vector and then be rewritten as

53

$$\boldsymbol{\tau}_d(\omega)\Delta\boldsymbol{\kappa} = \Delta\boldsymbol{K}\boldsymbol{T}_d(\omega) \tag{3-35}$$

where

$$\Delta\boldsymbol{\kappa} = \begin{bmatrix} \Delta k_1 & \Delta k_2 & \dots & \Delta k_n \end{bmatrix}^T \tag{3-36}$$

and

$$\boldsymbol{\tau}_d(\omega) = \begin{bmatrix} T_{d1}(\omega) & T_{d1}(\omega)-T_{d2}(\omega) & & & 0 \\ 0 & T_{d2}(\omega)-T_{d1}(\omega) & & \ddots & \\ & & \ddots & & \\ & \ddots & & T_{d(n-1)}(\omega)-T_{d(n-2)}(\omega) & T_{d(n-1)}(\omega)-T_{dn}(\omega) \\ 0 & & 0 & & T_{dn}(\omega)-T_{d(n-1)}(\omega) \end{bmatrix} \tag{3-37}$$

where $T_{dp}(\omega)$ presents the pth component in $\boldsymbol{T}_d(\omega)$. Substituting Eq. (3-35) into Eq. (3-33) and separating the complex FRF into real and imaginary parts, Eq. (3-33) becomes

$$\begin{bmatrix} \Re\boldsymbol{\tau}_d(\omega) \\ \Im\boldsymbol{\tau}_d(\omega) \end{bmatrix}\Delta\boldsymbol{\kappa} = \begin{bmatrix} \Re\boldsymbol{R}(\omega) \\ \Im\boldsymbol{R}(\omega) \end{bmatrix} \tag{3-38}$$

For a certain frequency ω_j, there are $2n$ equations with n unknowns to be solved. To reduce the noise effects and ill-posed problem, one may use m different frequencies and get $2n \times m$ equations and then solve them by a least-squares approach. Solving Eq. (3-38) gives the variations of elemental stiffness components without assuming the value of the baseline elemental stiffness matrices. The procedure to obtain Eq. (3-35) can be automated in a way similar to the development of the finite element model of the system (Caicedo 2003).

After the variations of elemental stiffness components in Eq. (3-36) are obtained by solving Eq. (3-38), the stiffness reduction ratio of the ith element can be obtained as $\dfrac{\Delta k_i}{k_i}$. Note that because k_i is not known analytically if no FE model is constructed,

here the components in the identified stiffness matrix using Eq. (2-34) can be utilized to calculate the stiffness reduction ratio.

The displacement FRF $\boldsymbol{T}(\omega)$ can be calculated by the FRF between the ground acceleration time-history and the response acceleration time-history and then divided by the square of the circular frequencies. Similarly, it can be calculated by the FRF between the ground velocity time-history and the response velocity time-history and then divided by the circular frequencies. The FRF can be obtained by one of the most commonly used FRF estimators which assumes that only the noise is present on the outputs and the noise is uncorrelated with the input signals as given by the following equations (Heylen 1997):

$$\boldsymbol{P} = \boldsymbol{G}_{yf}\boldsymbol{G}_{ff}^{-1} \tag{3-39}$$

where $\boldsymbol{G}_{ff}$ is the auto-power spectra of the inputs and $\boldsymbol{G}_{yf}$ is the cross-power spectra between the inputs and outputs given by

$$G_{ff}(\omega_k) = \frac{1}{N_b}\sum_{b=1}^{N_b} F_{b,k}F_{b,k}^{\ H} \tag{3-40}$$

$$G_{yf}(\omega_k) = \frac{1}{N_b}\sum_{b=1}^{N_b} Y_{b,k}F_{b,k}^{\ H} \tag{3-41}$$

with N_b the number of blocks by which the time data is divided and the input spectra $F_{b,k}$ and output spectra $Y_{b,k}$ given by the Discrete Fourier Transform (DFT) in combination with a window w_n as:

$$F_{b,k} = \frac{1}{\sqrt{N}}\sum_{n=0}^{N-1} w_n f_{b,n} z_k^{-n} \tag{3-42}$$

$$Y_{b,k} = \frac{1}{\sqrt{N}}\sum_{n=0}^{N-1} w_n y_{b,n} z_k^{-n} \tag{3-43}$$

with $z_k = e^{i2\pi k/N}$ and $f_{b,n}$, $y_{b,n}$ the time samples of the input and output signals for

block b at simple time $n\Delta t$ (Δt the sample period). The total number of time samples is N.

In summary, the FRFs of the system prior and posterior to damage as well as the system matrices including the mass matrix, damping matrix and stiffness matrix of the undamaged structure are required to solve Eq. (3-38). However, to obtain all the well-estimated or well-updated system matrices individually is not an easy task. Alternatively, one can obtain the well-estimated system matrix (i.e. $-\omega^2 M + i\omega C_1 + K$) instead of to obtain the well-estimated mass matrix, damping matrix and stiffness individually. In other words, the individual mass matrix, damping matrix or stiffness matrix is not necessary to be close to the true one, but only the system matrix composed of these matrices is necessary to be close to the true one. This can be achieved by using the subspace identification technique as described in Section 2.1.3 to evaluate the system matrix with acceptable accuracy. The feasibility of this technique is discussed in Section 4.2.

It is worth to be mentioned that for a shear building with diagonal mass matrix which is a good assumption in many practical cases, the mass matrix is not necessary to be known for the FRFC method. Multiplying the inverse of the mass matrix in both side of Eq. (3-31), Eq. (3-32) can be derived as:

$$\tilde{R}(\omega) = (-\omega^2 I + i\omega M^{-1}C_1 + M^{-1}K)\Delta T(\omega) \tag{3-44}$$

Following similar procedures, Eq. (3-28) can be derived as

$$\begin{bmatrix} \Re\tau_d(\omega) \\ \Im\tau_d(\omega) \end{bmatrix} \Delta\tilde{\kappa} = \begin{bmatrix} \Re\tilde{R}(\omega) \\ \Im\tilde{R}(\omega) \end{bmatrix} \tag{3-45}$$

where

$$\Delta\tilde{\kappa} = [\frac{\Delta k_1}{m_1} \quad \frac{\Delta k_2}{m_2} \quad \dots \quad \frac{\Delta k_n}{m_n}]^T \tag{3-46}$$

The mass normalized damping and stiffness matrices in Eq. (3-44) can be obtained

using Eq. (2-35) assuming that the damping and stiffness matrices are symmetric. The components in the identified mass-normalized stiffness matrix using Eq. (2-35) can be utilized to calculate the stiffness reduction ratio. The stiffness reduction ratio of the ith element can still be obtained as $\dfrac{\varDelta k_i}{k_i} = \dfrac{\varDelta k_i/m_i}{k_i/m_i}$.

3.2.2. Integrated with wireless sensing systems

Since the mid-1990s, a number of research teams in both academia and industry have proposed an impressive array of wireless sensing unit prototypes to be implemented for SHM (Lynch and Loh 2006). The essential part of a wireless sensing systems (WSS) is the wireless sensing unit (WSU) which generally consists of three or four functional subsystems: sensing interface, computational core, wireless transceiver and, for some, an actuation interface. A benefit of wireless structural monitoring systems is that they are inexpensive to install because extensive wiring is no longer required between sensors and a central data acquisition system. However, wireless sensing network is not simply a substitute for traditional tethered monitoring systems but also a decentralized architecture offering parallel processing of measured data. The collocated computational power endows wireless sensing systems great potential for research community to discover.

To date, wireless sensor networks are still in their infancy in many respects (Lynch and Loh 2006). One of the remaining limitations of current wireless sensing systems is the finite energy sources used to power devices in the field. Besides expecting the maturing of battery technology for the mobile devices, the research community has proposed several approaches to addressing the limitation of current battery technologies: (i) maximizing the time sensors are placed in sleep mode; (ii) pursuit of duty cycle usage schemes; (iii) designing the wireless sensor hardware to be as low power as possible; and (iv) power harvesting by converting ambient energy sources into usable and storable electrical energy. In addition, since wireless radio consumes more electrical energy than the computational core, energy can be saved by minimizing the use of the wireless communication channel. Therefore, minimizing the need to transfer long time-histories of structural response data, by programming wireless sensing units to

locally interrogate their data first, seems an appropriate solution.

The FRFC method answers to this idea and can be integrated with wireless sensing systems to take advantage of the collocated computational power and also save energy consumption of wireless sensing units. This is contributed by the advantage of the FRFC method where enough equations to obtain the least squares solution in Eq. (3-38) can be acquired by using FRFs at a few frequencies. The FRF estimation can be calculated by Eq. (3-39) which only needs the frequency spectrum segments calculated by fast Fourier transform (FFT) algorithm for measurement in each sensing unit. Without transmitting the whole time-history, only a short array composed of selected frequency spectrum segments is transmitted between the wireless sensing networks. The frequency spectrum segments can be selected as the frequencies close to the eigenfrequencies of the system since the signal to noise ratio of these Fourier spectra is much higher than others. This suggestion will be further discussed in Section 4.2 using some analytical case studies.

The operational scheme of the integration of FRFC with WSUs is illustrated in the flow chart in Figure (3-2). After the acceleration (or velocity) time-history $y_i(t)$ is measured in the ith WSU, the Fourier spectrum $Y_i(\omega)$ is calculated by the embedded FFT algorithm. A set of m eigenfrequencies of the structure in the ith WSU, $\bar{\omega}_i = [\bar{\omega}_{i1}, \bar{\omega}_{i2}, \cdots, \bar{\omega}_{im}]$, is determined by an embedded peak-picking algorithm which selects the peaks of the Fourier spectrum smoothed by an embedded smoothing algorithm. The frequency set $\bar{\omega}_i$ selected in each WSU is then transmitted wirelessly to the host computer. The most probable set of the system eigenfrequencies $\bar{\omega}_{system}$ is decided in the host computer and then broadcasted to all the n WSUs. The ith WSU then transmit a set of Fourier spectrum $\tilde{Y}_i(\tilde{\omega}_{system})$ back to the host computer. Note that the frequencies set $\tilde{\omega}_{system}$ can contain not only the system eigenfrequencies $\bar{\omega}_{system}$ but also some adjacent frequencies around them. After the host computer receives the selected frequency spectrum segments from all the WSUs, the FRF segments are estimated using Eq. (3-39). The variations of elemental stiffness matrices $\Delta \kappa$ can be calculated using these FRF segments by Eq. (3-38).

Since the necessary information for FRFC method to detect damage of the structure could be accessed automatically right after a ground excitation, *i.e.* a train passing or an

earthquake, on-line damage detection could be achieved by this operational scheme. The realization of the operational scheme in a laboratory test is presented in Section 4.2. The benefit of saving energy by integrating FRFC method with WSUs is also discussed in the same section.
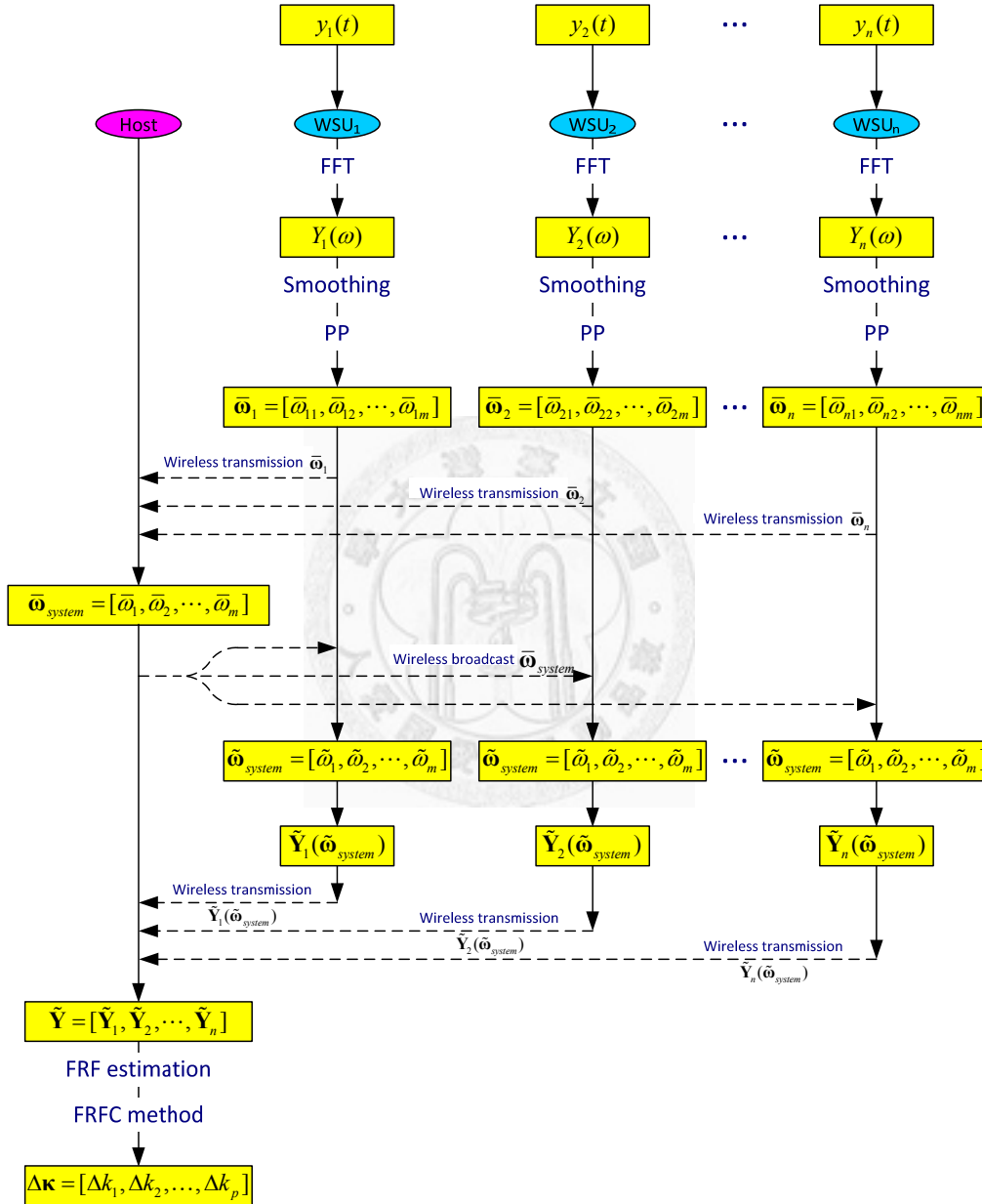
Figure 3-2: Operational scheme of the FRFC method integrated with WSUs.

3.3.   Local Flexibility Method

The local flexibility method which not only localizes but also quantifies the damage of a structure has been developed by Reynders and De Roeck (2010). This method tries to obtain the quasi-static flexibility matrix by making use of the dynamic flexibility matrix evaluated at zero frequency. Based on the principle of virtual work, provided the stress-strain relationship is proportional, the ratio of virtual work done by some virtual force before and after a change in stiffness has occurred equals the inverse stiffness ratio. The virtual force can be selected to make the structure consist of nonzero stress only in a "local" region; by doing so, the change of local stiffness can be quantified. This is probably the reason that the method is called "local" flexibility method.

Because the construction of the quasi-static flexibility matrix requires only the modal parameters (eigenfrequencies, damping ratios and mode shapes), the local flexibility method can be classified as a rarely model-based method if a mass-normalized mode shape is used. The dependence of the model of the structure is quite limited. Furthermore, if the assumptions of lumped mass and equally mass distribution are valid, the non-mass-normalized mode shapes can be implemented and hence the local flexibility method approaches a non-model based method. The model-independence is one of the advantages of this method.

Another advantage of this method is common for all the methods using flexibility matrices, instead of using stiffness matrices. Due to the nature that, observing equations (2-40) and (2-41), while the influence of the modes on stiffness matrices increases with ω^2, the influence of the modes on flexibility matrices decreases with ω^{-2}. As a results, the number of truncated modes need to approximate a non-truncated flexibility matrix is much smaller than the ones need to approximate a non-truncated stiffness matrix. This benefits the application cases where only lower modes can be identified with good accuracy.

Although the concept of local flexibility method is a general principle applicable to linear elastic structures, all the applications in the literature are limited to beam-like structures such as reinforced concrete beams in the laboratory and a prestressed concrete bridge. The feasibility of application to building structures needs to be investigated,

especially for the low-rise buildings with lower flexibilities. The local flexibility method is summarized in this section, and the application of this method to building structures is discussed in Section 4.3.

3.3.1. General Principle

Consider a structure with Volume $\mho$ and boundary Γ which is subjected to the Dirichlet boundary conditions $x = \bar{x}$ along part of the boundary as shown in Figure 3-3. A first load system f^1 is applied at a limited number of l DOFs where response can be measured. The first load system is chosen such that the induced stress field σ^1 (1) can be calculated from the loading without knowledge of the structure's stiffness and (2) consists of nonzero stresses in a small volume $\mho_p$ only. The stiffness within $\mho_p$ is assumed constant.
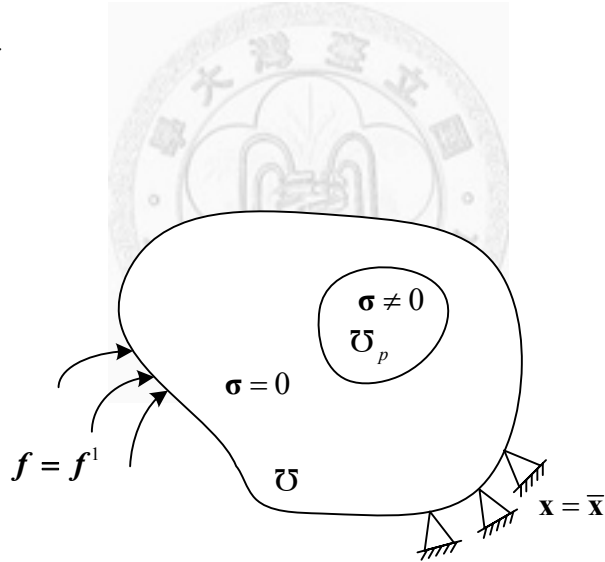
Figure 3-3: A structure subjected to load system f^1 that causes nonzero stresses in $\mho_p$ only.

(modified from Reynders and De Roeck 2010)

The virtual work principle states that

$$\int_{\mho} \rho b^T \delta x d\mho + \int_{\Gamma} t^T \delta x d\Gamma = \int_{\mho} \sigma^T \delta \varepsilon d\mho \qquad (3\text{-}47)$$

Where $\boldsymbol{b} \in \mathbb{R}^{3 \times 1}$ is the vector with body forces, $\boldsymbol{t} \in \mathbb{R}^{6 \times 1}$ the vector with applied tractions, $\boldsymbol{\sigma} \in \mathbb{R}^{6 \times 1}$ the corresponding stress vector, $\delta \boldsymbol{x} \in \mathbb{R}^{3 \times 1}$ a virtual displacement field that obeys the Dirichlet boundary conditions and $\delta \boldsymbol{\varepsilon} \in \mathbb{R}^{6 \times 1}$ the corresponding virtual strain vector. If the virtual displacement field is chosen as the one that is induced by the first load system $\boldsymbol{f}^1$ and the forces and the stresses are due to the second load system $\boldsymbol{f}^2$ which obeys the boundary condition of the system, one has that

$$\sum_{j=1}^{l} f_j^2 x_j^1 = \int_{\mho_p} (\boldsymbol{\sigma}^2)^T \boldsymbol{\varepsilon}^1 d\mho_p \tag{3-48}$$

where x_j^1 is the displacement at DOF j corresponding to the first load system. This equation shows that $\boldsymbol{x}^1$ is only dependent on the stress-strain relationship inside $\mho_p$. Assume that the structure is linear elastic and that $\boldsymbol{\sigma}^1$ is proportional to $\boldsymbol{\varepsilon}^1$ with stiffness constant K. For example, for a linear elastic isotropic structure where K equals the elastic modulus E, $\boldsymbol{\sigma}^1$ is proportional to $\boldsymbol{\varepsilon}^1$ with stiffness constant K as long as Poisson's ratio is constant since

$$\begin{bmatrix} \varepsilon_{xx} \\ \varepsilon_{yy} \\ \varepsilon_{zz} \\ \varepsilon_{xy} \\ \varepsilon_{yz} \\ \varepsilon_{zx} \end{bmatrix} = \frac{1}{E} \begin{bmatrix} 1 & -\nu & -\nu & 0 & 0 & 0 \\ -\nu & 1 & -\nu & 0 & 0 & 0 \\ -\nu & -\nu & 1 & 0 & 0 & 0 \\ 0 & 0 & 0 & 1+\nu & 0 & 0 \\ 0 & 0 & 0 & 0 & 1+\nu & 0 \\ 0 & 0 & 0 & 0 & 0 & 1+\nu \end{bmatrix} \begin{bmatrix} \sigma_{xx} \\ \sigma_{yy} \\ \sigma_{zz} \\ \sigma_{xy} \\ \sigma_{yz} \\ \sigma_{zx} \end{bmatrix} \tag{3-49}$$

If $\sum_{j=1}^{l} f_j^2 x_j^1$ is calculated before and after damage has occurred, one has

$$\frac{\sum_{j=1}^{l} f_j^2 x_j^1}{\sum_{j=1}^{l} f_j^2 x_{jd}^1} = \frac{\int_{\mho_p} (\boldsymbol{\sigma}^2)^T \frac{\boldsymbol{\sigma}^1}{K} d\mho_p}{\int_{\mho_p} (\boldsymbol{\sigma}^2)^T \frac{\boldsymbol{\sigma}_d^1}{K + \Delta K} d\mho_p} = \frac{K + \Delta K}{K} \tag{3-50}$$

where ΔK is the change in the stiffness parameter in $\mho_p$ due to damage. It is assumed that ΔK is constant within $\mho_p$.

3.3.2. Application to Bending Stiffness of Beam Structures

Although the theoretical basis above is general to any structure type, here the general principle is applied to the estimation of changes of bending stiffness of isostatic and hyperstatic beams. The stiffness parameter K of Eq. (3-50) is substituted by EI where E is the elastic modulus in volume $\mho_p$ and I is the moment of inertia in volume $\mho_p$ with beam's cross-section with respect to the transversal axis.

Consider a beam structure under the load configuration f^1 as shown in Figure (3-4). If shear deformation can be neglected and EI is constant between equidistant points $j-2$ and $j+2$, the force configuration of Figure (3-4) causes nonzero stresses between points $j-2$ and $j+2$ only, whatever the beam is isostatic or hyperstatic. This can be proved if

(1) The vector sum of all forces of Figure (3-4) is zero;

(2) The resulting moment of all forces of Figure (3-4) at points $j-2$ and $j+2$ is zero.

(3) The relative rotation between points $j-2$ and $j+2$, due to the force configuration, is zero.
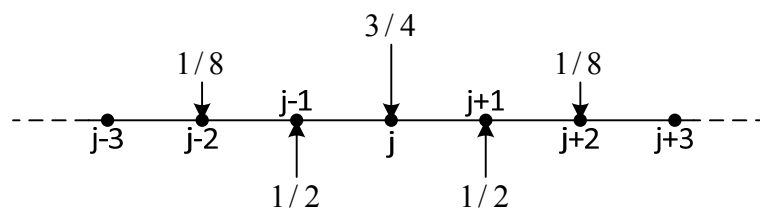
Figure 3-4: A beam structure with load configuration that causes virtual stresses and strains around one particular measurement DOF j only.
(modified from Reynders and De Roeck 2010)
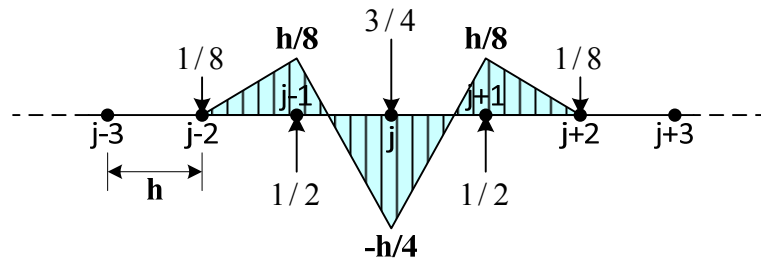
Figure 3-5: Bending moments due to the load configuration of Figure 3-4.

(modified from Reynders and De Roeck 2010)

Checking the first two conditions is trivial, and the moment diagram is shown in Figure (3-5). The third condition can be easily checked by means of the virtual work principle with applying a virtual unit moment pair at points $j-2$ and $j+2$.

The second load configuration can be chosen as any configuration that obeys the boundary conditions, like for example the configuration of Figure (3-6).
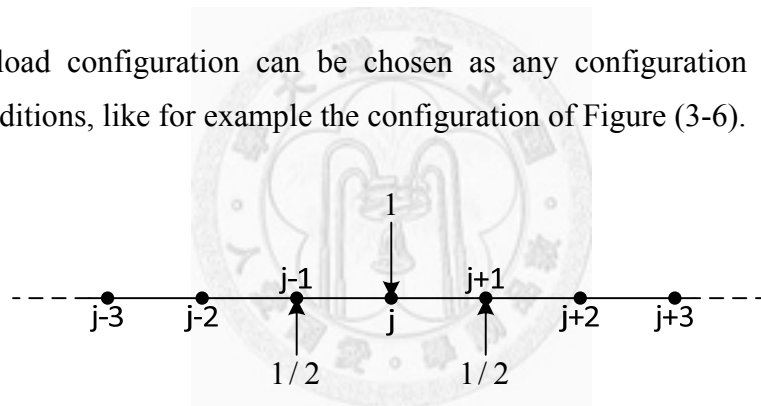
Figure 3-6: A beam structure with possible second load configuration.

(modified from Reynders and De Roeck 2010)

Following Eq. (3-48), with applying load configuration f^1 as shown in Figure (3-4) and applying load configuration f^2 as shown in Figure (3-6), one has that

$$x_j^1 - \frac{1}{2}(x_{j-1}^1 + x_{j+1}^1) = \int_{\mho_p} M^2 \frac{M^1}{EI} d\mho_p \qquad (3-51)$$

It follows from (3-50) that

$$\frac{x_j^1 - \frac{1}{2}(x_{j-1}^1 + x_{j+1}^1)}{x_{jd}^1 - \frac{1}{2}(x_{j-1,d}^1 + x_{j+1,d}^1)} = \frac{EI + \Delta EI}{EI} \tag{3-52}$$

It should be noted that for isostatic beams, as an alternative to the load configuration f^1 of Figure (3-4), the force configuration of Figure (3-6) can be applied. The proof is trivial since for isostatic structures, it is not necessary that the relative rotation between points $j-1$ and $j+1$ be zero in order to have nonzero stress between theses points only.

The displacement vector x^1 under the first load system f^1 can be obtained using the following equation

$$x^1 = Hf^1 \tag{3-53}$$

where H is the flexibility matrix which can be obtained using the approaches introduced in Section 2.1.4. Note that normally the mass-normalized mode shapes can be obtained by normalizing the measured mode shapes with the analytical mass matrix constructed by a FE model or can be obtained by identifying from a forced-vibration test using CSI technique described in Section 2.1.2. Afterwards, the mass-normalized mode shapes can be used to obtain the flexibility matrix using Eq. (2-41) or Eq. (2-42). Alternatively, suppose the mass of a structure is equally distributed and can be approximated as a lumped mass matrix, a non-mass-normalized mode shape identified from an ambient vibration test (output-only identification) can be used to obtain the flexibility matrix using Eq. (2-46) and Eq. (2-49).

4. VERIFICATION OF DAMAGE DETECTION METHODOLOGY

In this section, the damage detection algorithms introduced in Chapter 3 were verified through numerical and experimental studies. In Section 4.1, several numerical studies were conducted to validate the modified MSEC method. Afterwards, the modified MSEC method was verified by a full-scaled 3-story steel building structure experimentally. The damage was simulated by cutting the flanges of the columns in the 1st story which made the building un-symmetric. Cutting flanges of an H-shape column also made the stiffness reduction ratio of the column different in DOFs, which is suitable for verifying modified MSEC method. However, this destructive simulation of damage was permanent and was not easy to conduct; hence only one damage simulation was made. In Section 4.2, the feasibility of the proposed FRFC method for damage localization and quantification was studied through a numerical simulation of a 2D 6-story shear building. Both the effects of measurement noise and modeling error were considered. Afterwards, the FRFC method was verified by a 1/4-scaled 6-story steel building structure experimentally. Several damage cases were simulated by simply replacing or removing special-designed connecting plates between bracings and floors. The idea of integrating FRFC method with wireless sensing systems as proposed in Section 3.2.2 was also validated using the same 6-story steel building structure. In Section 4.3, because former numerical and experimental verifications of the LFM focused on the beam structures and bridge structures, the feasibility of the LFM applied to building structures were discussed. The LFM was verified by numerically studies and the same 6-story steel building structure experimentally.

4.1. Modal Strain Energy Change Method

The ability of original MSEC method to identify the damage location and quantity of a structure was verified by an analytical beam structure and also an experimental portal frame structure (Shi *et al.* 2000). However, these simulation and experimental studies for original MSEC method solely focused on 2D structures. Therefore, one of the main purposes of this section is to investigate the feasibility of application of original and

modified MSEC method to a 3D steel building structure (target structure).

Both numerical and experimental study of the target structure was conducted to examine the advantage of damage detection of the proposed MSEC method over the original MSEC method. The experimental study of the MSEC method of the target structure was performed on a shaking-table in NCREE. It is worth to be mentioned that very limited DOFs were measured during the experimental test, as is common in civil engineering structures. Less measurement increase the difficulty of vibration-based damage detection, which will be discussed via a numerical study in this section.

Because the MSEC method is highly model-based, a FE model of the target structure with acceptable accuracy is necessary. Therefore, in the beginning of this section (Section 4.1.1), the experimental setup as well as the FE model of the target structure are both described.

In the section of numerical study (Section 4.1.2), besides the validation of the original and modified MSEC method, three preliminary numerical studies were performed to verify some proposed modifications of procedures when applying MSEC method (Section 4.1.2.1 to Section 4.1.2.3). Afterwards, the numerical studies of the proposed modified MSEC method and also the difficulty caused by relatively sparse measurement of the target structure are presented (Section 4.1.2.4 to Section 4.1.2.6).

4.1.1. Target Structure Description

4.1.1.1. Experimental Setup

The target structure for validating the proposed modified MSEC method was a full-scale 3D benchmark model in the laboratory of National Center for Research Center on Earthquake Engineering (NCREE). It was a 1-bay × 1-bay × 3-story steel building structure (Figure 4-1). The dimension of the target structure was 2m, 3m and 9m in X, Y and Z direction, respectively (Figure 4-2). The dimension of the beams and columns was H150×150×7×10 mm and the floor plate was 25 mm thick. The dead load was simulated by lead-block units fixed on the steel plate of each floor, and the total mass of each floor of the target structure was 5,943 kg.

To imitate the damaged state, which was like the plastic hinge of the column, the flanges of the bottom of two of the first story columns were sliced with 2 cm wide and 20cm long for both sides (Figure 4-1 and Figure 4-2). According to the numerical study of the entire damaged column of the first floor by SAP2000 commercial software, the force required to achieve 1 unit deformation in each DOF on the top of the designated-damaged columns (*i.e.* the point No. 5 and 6 in Figure 4-2) was deducted to different extents, as summarized in Table 4-1.

Figure 4-1: Photo of the 3D experimental target structure in NCREE's lab.
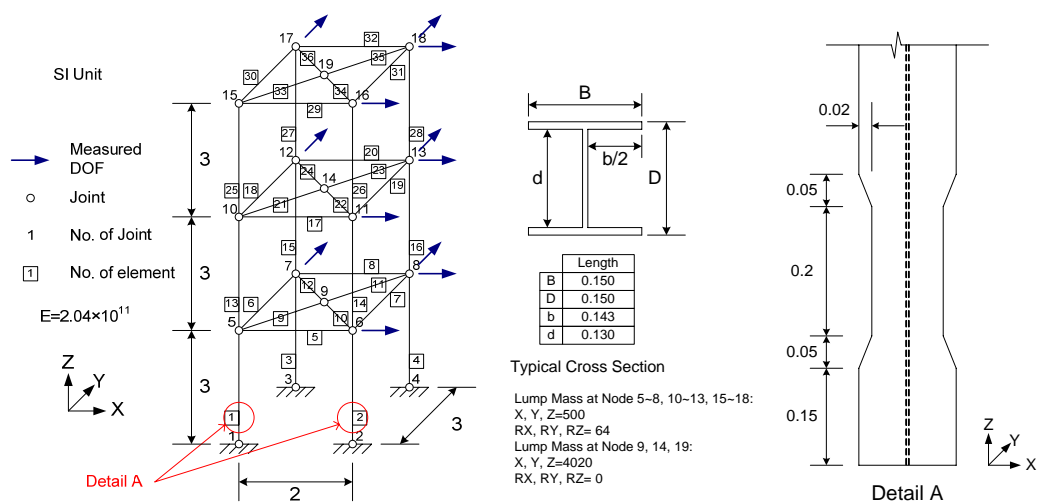
Figure4-2: The FE model of the 3D target structure and detail of cross section reduction in elements 1 and 2.

Table 4-1: Stiffness reduction of the sliced column in each DOF.

Global Coordinate	Reduced Quantity
Z	-2.5%
X	20.3%
Y	-5.5%
Rotation of Z	-3.1%
Rotation of X	-6.8%
Rotation of Y	-25.2%

The target structure was subjected to excitations simulated by the shaking-table in NCREE. Bi-lateral excitation tests of El Centro earthquake with peak ground acceleration (PGA) 0.1 g were conducted both before and after the "damage" was introduced into the target structure. The acceleration responses during the tests were measured only at points 6, 8, 11, 13, 16, and 18 in X direction, and points 7, 8, 12, 13, 17, and 18 in Y direction.

In order to have a roughly idea about the density of measured DOFs of the target structure, the Coefficient of Measurement Density (CMD), defined as (measured number of DOFs)/((number of elements)×(number of DOFs per node)), is calculated. The CMD of the target structure is (12)/(36×6)=1/18, while that of the experimental

case study of the original paper (Shi *et al.* 2000) is (16)/(18×3)=8/27, which is more than 5 times the CMD of the target structure, thus indicating that only very limited DOFs are measured on the target structure. Accordingly, damage detection is likely to be much more difficult for this target structure.

4.1.1.2. Identified Modal Parameters of the Target Structure

Before identifying the modal parameters of the target structure, the measured time-history was observed. Figure 4-3 depicts the typical measured acceleration time-history in X and Y directions at point 18 of the intact and damaged structure. The figure reveals that the period of the response in X direction was prolonged after damage was introduced.
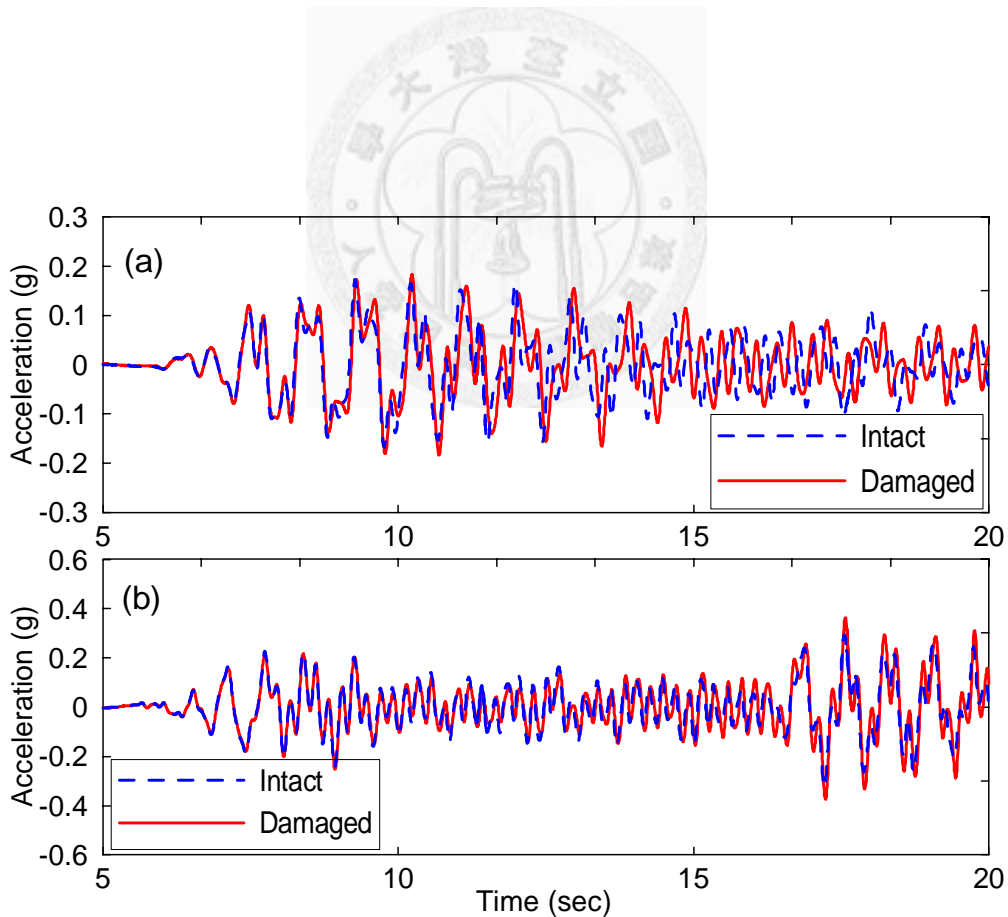
Figure 4-3: Comparison on the measured acceleration response at point 18 of the target structure in intact state and damaged state: (a) X direction; (b) Y direction

The un-damped eigenfrequencies, damping ratio and mode shapes were identified using the stochastic subspace identification technique introduced in Section 2.1.1 with only the measured response acceleration time-histories. The mean phase deviation (MPD) of each identified mode shapes was calculated using the proposed modified algorithm introduced in Section 2.2.2 to estimate the complexity of the identified mode shapes. The un-damped eigenfrequencies, damping ratio and MPD of the target structures in both intact and damaged states are listed in Table 4-2. The quality of the identified modes are good because their MPD are less than 5° and their damping ratios are reasonable. The eigenfrequencies after the target structure was damaged were smaller than the ones of the intact target structure, which corresponds to the observation in time-history.

Table 4-2. Modal parameters of the target structure in both intact and damaged states.
(X: x-direction, Y: y-direction, T: torsion)

Mode	Experimental						Analytical		
	Intact			Damaged					
	$(f_i)_I$	ξ_I	MPD_I	$(f_i)_D$	ξ_D	MPD_D	$(f_i)_A$	$(f_i)_A/(f_i)_I-1$	MAC
	(Hz)	(%)	(°)	(Hz)	(%)	(°)	(Hz)	(%)	(-)
X1	1.094	1.5	3.2	1.067	1.8	4.4	1.116	2.02	1.000
Y1	1.370	1.9	4.3	1.363	1.9	4.5	1.417	3.44	0.999
T1	2.090	0.2	0.3	2.043	0.6	3.3	2.100	0.47	1.000
X2	3.321	0.2	1.1	3.262	0.2	0.6	3.304	-0.51	0.999
Y2	4.611	0.2	0.5	4.588	0.2	0.9	4.587	-0.50	0.997
X3	5.180	0.2	1.5	5.148	0.2	0.7	5.123	-1.10	0.999
T2	6.498	0.0	0.6	6.428	0.1	0.6	6.423	-1.15	0.995
Y3	8.193	0.2	1.0	8.174	0.2	0.8	7.980	-2.60	0.998
T3	10.819	0.2	0.8	10.773	0.2	0.7	10.459	-3.33	0.996

4.1.1.3. FE Model of the Target Structure

Figure 4-2 shows the details of the geometrical and physical information of FE model of the target structure, which consists of 36 beam-column elements. Each point has 6 DOFs, making a total of 90 DOFs. The axial stiffness of the elements No. 9~12, 21~24, 33~36 are magnified 1000 times to simulate the stiffness contribution of the steel plate

and lead block units, while the bending and torsion stiffness of the same elements were reduced to 1/100. The distribution of mass of each joint in each floor is manually adjusted to fit the experimental modal results. The mass distribution of the structure is assumed unchanged due to damage.

Table 4-2 lists the eigenfrequencies of the analytical FE model and the differences between the analytical and experimental eigenfrequencies. To evaluate the analytical mode shapes of the FE model, the modal assurance criterion (MAC) was utilized to verify the similarity between the analytical and experimental mode shapes. Table 4-2 also lists the diagonal values of the MAC between the experimental (structure in intact state) and analytical mode shapes. In summary, the differences between the analytical and experimental eigenfrequencies were all less than 4%, and the diagonal values of the MAC were all larger than 0.995. These findings reveal that the FE model can represent the target structure well. With the well-estimated FE model ready, the experimental mode shapes can be mass-normalized according to the analytical mass matrix, and can be expanded according to stiffness and mass matrices using dynamic expansion algorithm as introduced in Section 2.2.3. The stiffness matrix of each element can be used to calculate the stiffness reduction factors using the MSEC method.

4.1.2. Numerical Validation

Before verifying the feasibility of application of the original and modified MSEC method to the target structure, three preliminary numerical studies (Sections 4.1.2.1 ~ 4.1.2.3) were performed to verify some proposed modifications of procedures when applying MSEC method. Firstly, the MSECR while selecting the suspected damaged elements is determined "without" taking absolute MSEC value rather than taking absolute MSEC value. Secondly, dynamic expansion algorithm is utilized to expand the incomplete measured DOFs instead of the SEREP utilized in the original paper (Shi *et al.* 2000). Thirdly, a threshold of MSE when selecting suspected damaged elements is proposed to make sure that damage locations can be identified clearly without the interference caused by the elements with little MSE, especially for a 3D structure. For better illustration and explanation, a fixed beam, the same as the numerical example of the original paper, is chosen as the test structure for the first two preliminary numerical

studies. A simple 3D test structure is chosen for the third preliminary numerical studies for the same reason.

Another three numerical studies of the target structure (Sections 4.1.2.4 ~ 4.1.2.6) were performed to verify the effectiveness of the modified MSEC method and the modified iteration process on damage detection. The FE model of the target structure was utilized in these sections. The original and modified MSEC methods were compared in Section 4.1.2.4, while the original and modified iteration processes were compared in Section 4.1.2.5. Owing to the very limited measurements of the target structure, the numerical study of the effect of modal expansion was performed in Section 4.1.2.6. Consequently, there are six subsections of numerical case studies in this section.

4.1.2.1. Preliminary Study on MSECR

When calculating MSECR for damage localization, taking absolute value of MSEC may obscure the damage locations (Ren and De Roeck 2002) especially in lower modes. Therefore, in the first part of this section, the results of damage localization determined by original procedure and modified procedure are compared. The original procedure utilizes absolute average normalized $MSECR_j$ obtained via Eq. (3-2), and the modified one utilizes non-absolute average normalized $MSECR_j$ obtained via Eq. (3-11). The non-absolute average normalized $MSECR_j$ will be illustrated as a better damage localization indicator in this section.

A fixed beam, the same as the numerical example of the original paper (Shi *et al.* 2000), is chosen as the structure for numerical study on MSECR and also the following discussion on modal expansion in Section 4.1.2.2. The FE model of the beam consists of 12 elements and 13 nodes with 33 DOFs as shown in Figure 4-4. The geometrical and physical data are as follows: length of each element is 0.6 m; elastic modulus is 7.5×10^{10} N/m^2; cross-sectional area is 0.001 m^2; moment of inertia is 7.56×10^{-7} m^4; and mass density is 7,800 kg/m^3. The damage occurs in the 6th element with stiffness loss 15%. Only the vertical DOFs of each node are assumed to be measured.
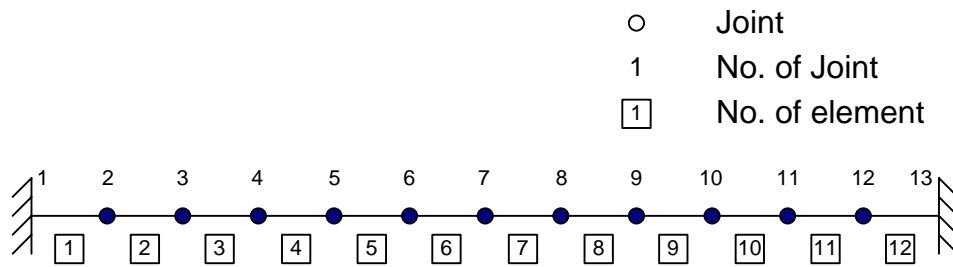
Figure 4-4: A FE model of the fixed-ends beam which is the test structure in Section 4.1.2.1 and 4.1.2.2.

The first 5 complete mode shapes are utilized to calculate MSECR value. The absolute MSECR obtained via Eq. (3-2) and Eq. (3-3) are shown in Figure 4-5(a), while the non-absolute ones obtained via Eq. (3-11) and Eq. (3-3) are shown in Figure 4-5(b). Comparing these 2 figures, the damage location at the 6th element is illustrated clearly in both figures, but the later one is much clearer. In this case, only a small part of the elements will be selected as the suspected damaged elements even when the data is polluted by some noise.
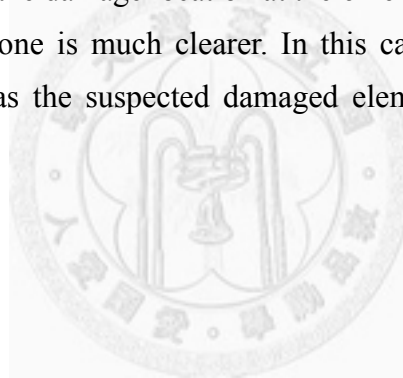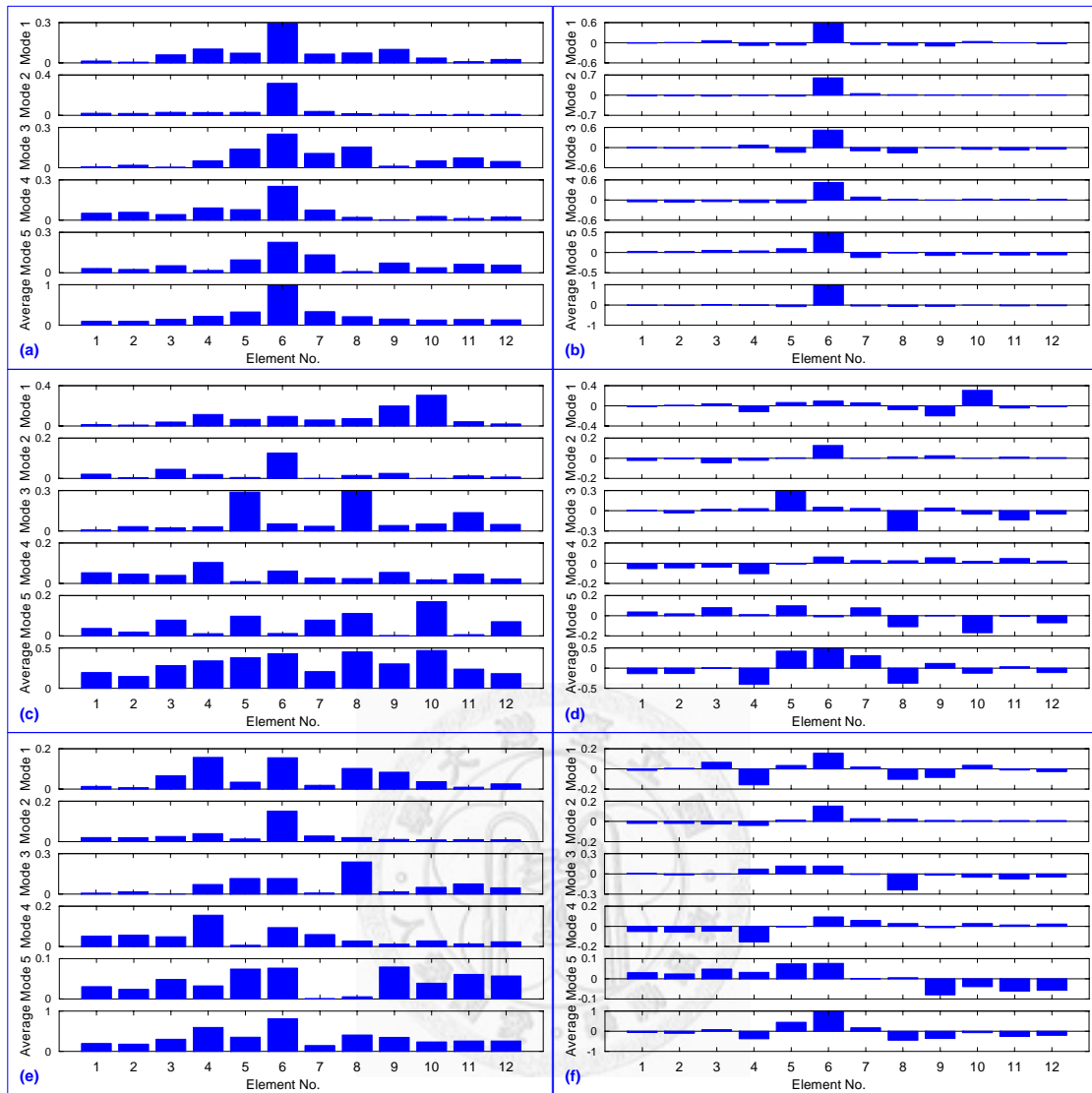
Figure 4-5: MSECR determined by (a) complete analytical mode shapes w/ taking absolute; (b) complete analytical mode shapes w/o taking absolute; (c) SEREP-expanded mode shapes w/ taking absolute; (d) SEREP-expanded mode shapes w/o taking absolute; (e) dynamic-expanded mode shapes w/ taking absolute; (f) dynamic-expanded mode shapes w/o taking absolute.

4.1.2.2. Preliminary Study on Modal Expansion Methods

This section compares the results of damage localization and damage quantification by utilizing different mode shape expansion methods. In practice, the measured DOFs of mode shapes are incomplete because of the limited number of sensors and the difficulty to get the information of rotational DOFs. Therefore, the original author utilizes the

SEREP (Shi *et. al.* 1995) to expand the DOFs of measured mode shapes as described in Section 2.2.3.2. The dynamic expansion method as described in Section 2.2.3.1 is proposed to be employed here and the results are compared to the ones obtained by utilizing the SEREP.

Utilizing the SEREP-expanded mode shapes and dynamic-expanded mode shapes through the same procedures, the results of both absolute or non-absolute MSECR are shown in Figure 4-5(c), (d), (e), and(f). The figures on the left side of Figure 4-5 are all absolute ones, while the figures on the right side are all non-absolute ones. Figure 4-5(c) and (d) show the results from the SEREP-expanded mode shapes, whereas Figure 4-5(e) and (f) show the results from the dynamic-expanded mode shapes.

The result of Figure 4-5(c) looks so vague that the number of suspected damaged elements is difficult to determine. All the values of average normalized MSECR are under 0.5, even the true damaged 6th element becomes the 3rd suspected element. The result of damage localization in this case is quite poor. On the other hand, the result of Figure 4-5(d) looks much clearer than the previous one. Only 3 or 4 elements will be selected with high confident, including the 6th element as the most suspected damaged one. Comparing the results of Figure 4-5(c, d) and Figure 4-5(e, f), it is obviously that dynamic modal expansion is much more suitable than the SEREP for calculating the MSECR because less elements will be selected with the 6th element remains as the most suspected damaged one. Combining the advantage of dynamic expansion and taking non-absolute values of MSE, Figure 4-5(f) illustrates a better procedure for damage localization in practice. The maximum value of the average normalized MSECR is 1.0 at element 6th, and the other values of the average normalized MSECR are under 0.5.

The suitability for damage quantification utilizing different modal expansion methods is also studied. For comparison, the suspected damaged elements are selected the same as in the original paper (Shi *et. al.* 2000). They are elements 4, 6, 7, and 11. The numbers J and P in Eq. (3-10) are equal to 4. The MSEC of these suspected damaged elements are computed from Eq. (3-8), and the sensitivity coefficients are calculated from Eq. (3-9). The stiffness variations of the suspected damaged elements are obtained from solving Eq. (3-10) without iteration, and the results from utilizing individual mode are all listed in Table 4-3. However, for clear illustration, only the stiffness variation of

element 6th is shown here. The damage indexes obtained by individual complete analytical mode shapes are reasonable. If the mode shapes expanded with SEREP are utilized via the same procedure, the stiffness variations with large error were obtained by individual mode shapes. Moreover, the stiffness reduction of other elements is even larger than the one of the 6th element for the cases using the 4th and 5th mode individually, which means false-positive damage assessment of intact elements or false-negative damage assessment of the 6th element could be concluded. On the other hand, if the mode shapes expanded with dynamic expansion are utilized via the same procedure, the stiffness variations obtained by the first 5 individual mode shapes are closer to the true stiffness loss ratio. It is concluded that the dynamic modal expansion is not only more suitable for damage localization but also for damage quantification comparing to the SEREP.

Table 4-3: Comparison of damage indexes calculated by complete or expanded mode shapes.

Method	Damage Index of Element 6 (true value = -15%)				
	Mode 1	Mode 2	Mode 3	Mode 4	Mode 5
Complete Mode Shapes	-17.0%	-17.2%	-16.6%	-16.8%	-16.3%
SEREP Modal Expansion	-6.6%	-6.9%	-4.9%	-2.6%*	-5.8%*
Dynamic Modal Expansion	-9.7%	-7.1%	-9.0%	-4.4%	-9.8%

* Damage Index of other elements is even smaller

4.1.2.3. Preliminary Study on a 3D Frame Structure for MSECR

The damage localization procedure utilizing MSECR is studied with a simple 1-bay × 1-bay × 1-story 3D steel building structure for clear illustration. The FE model of the 3D structure is shown in Figure 4-6 with details of the geometrical and physical information. The FE model consists of 8 elements and 8 nodes with 24 DOFs, and the damage is assumed to occur at elements 1 and 2 with 15% stiffness loss.
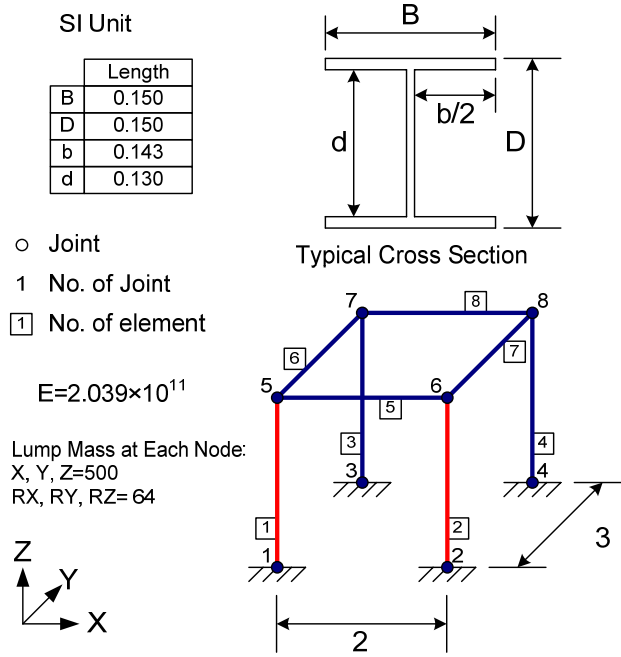
Figure 4-6: FE model of a 3D steel building structure.

The first 3 complete analytical mode shapes are utilized to calculate MSECR, and the results of non-absolute $MSECR_{ij}$ are shown in Figure 4-7(a). The MSECR of element 6 and 7 in the first mode (X-dir.) is extraordinary large, as well as the MSECR of element 5 and 8 in the third mode (Y-dir.). It is easy to find out that the MSE of these elements in the translation modes are close to zero, and hence the MSECR of these elements in certain modes will be abnormal.

Certain level of MSE should be limited for calculating MSECR, and the criteria for removing the possibility of resulting in abnormal MSECR is proposed to neglect the jth element in i^{th} mode if

$$MSE_{ij} < C_{MSE} \times \frac{1}{L} \sum_{j=1}^{L} MSE_{ij} \tag{4-1}$$

in the undamaged state, where C_{MSE} is defined as the threshold of MSE. With setting C_{MSE} equal to 0.05, the MSECR obtained by the same procedure are shown in Figure 4-7(b). The damage locations at element 1 and 2 are clearly identified via the modified procedure.
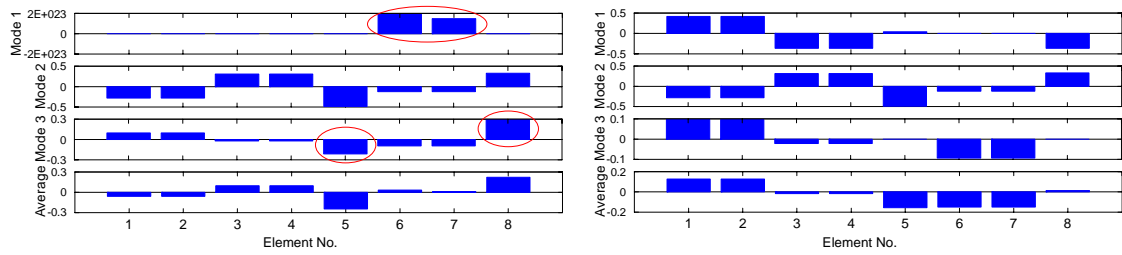
Figure 4-7: MSECR determined by complete mode shapes (a) w/o setting limit; (b) w/ setting C_{MSE} =0.05.

4.1.2.4. Comparison between Original and Modified MSEC Method

The stiffness reduction factors obtained by the original and modified MSEC methods were compared in this section to demonstrate the effectiveness of the modified MSEC method. Complete DOFs of mode shapes obtained by analytical FE model were utilized, meaning that the modified and original iteration processes were identical in this case, and less than three iterations were processed in the studies in this section. The numerical and the later experimental study of the target structure employed the first 78 analytical modes to compute the MSEC sensitivity coefficients of the target structure.

To imitate the true damage state in the FE model of the target structure described in Section 4.1.1.3, the sectional properties of the 1st and 2nd elements were reduced similar to the results in Table 4-1, as summarized in Table 4-4. The approximate stiffness reduction of sectional properties of element 1 and 2 was utilized in the following numerical studies in Sections 4.1.2.4 ~ 4.1.2.6.

Table 4-4: Approximate reduction of sectional properties of elements 1 and 2 in the FE model of the target structure.

Sectional Property	Reduced Quantity
A	-2.0%
I_z	-20.0%
I_y	-6.0%
I_x	-3.0%

Original MSEC Method

The first step was to locate the suspected damaged elements by MSECR. The proposed non-absolute MSECR was proved better-indicating of suspected damaged elements than the absolute MSECR in Section 4.1.2.1, hence was utilized in the following numerical and experimental studies. The MSECR of each element is calculated from Eq. (3-11) for the first 9 individual modes. Although MSECR obtained by each individual mode can also be used to select the suspected damaged elements, for simplicity only the $MSECR_j$ obtained in Eq. (3-3) via combination of different kind of mode shapes were considered. Five combinations were studied: (1) modes 1, 4 and 6 (X-dir.); (2) modes 2, 5 and 8 (Y-dir.); (3) modes 3, 7 and 9 (Torsion); (4) modes 1, 2, 4, 5, 6 and 8 (X- and Y-dir.), and (5) modes 1 through 9. For discarding the abnormal MSECR caused by elements with small MSE, C_{MSE} was chosen as 0.05. The same value of C_{MSE} was used in the following numerical studies. Figure 4-8(a) shows the damage localization results, with MSECR plotted against the element number. Elements with MSECR > 0.05 were chosen as suspected damaged elements. For instance, the first combination of mode 1, 4 and 6 contained four elements with MSECR > 0.05, namely elements 1, 2, 13 and 14.
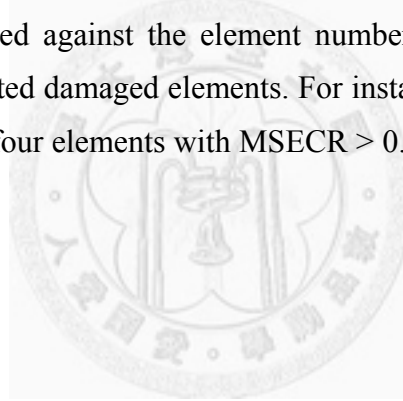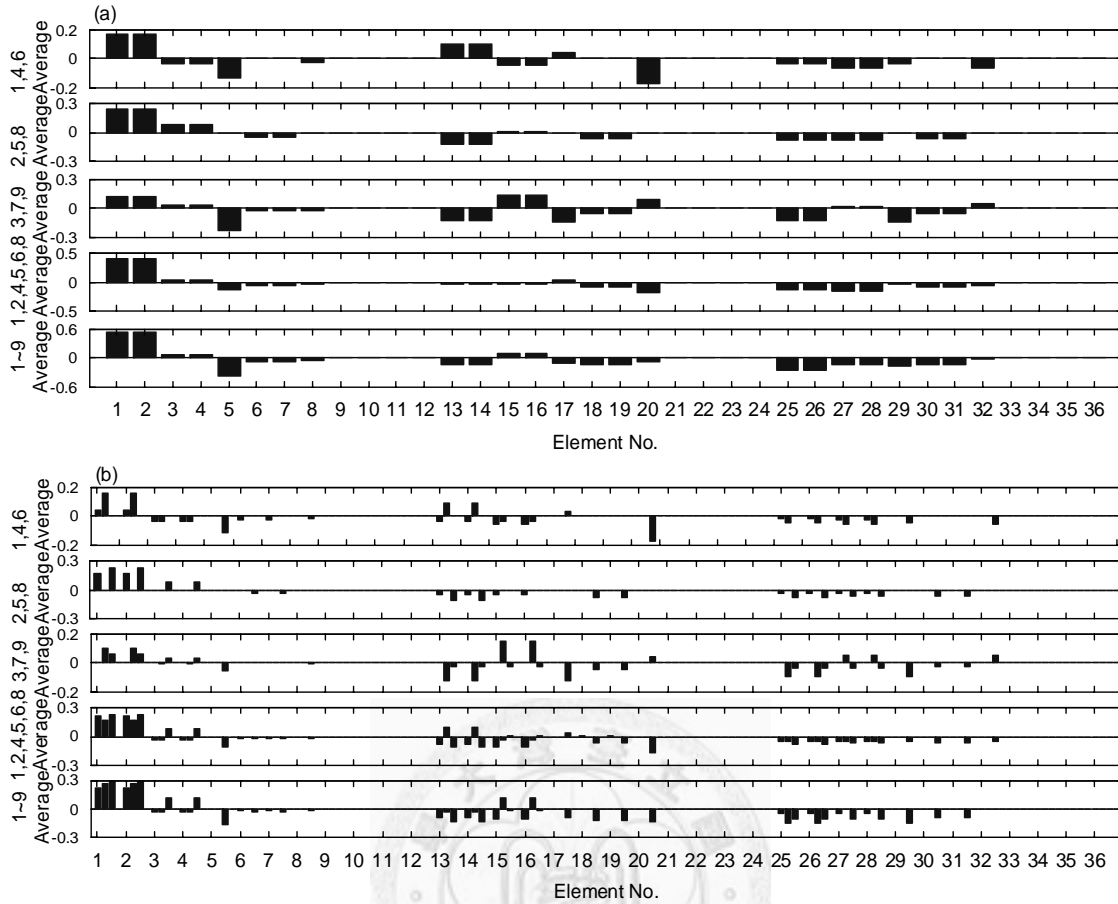
Figure 4-8: Damage localization results of the 3D target structure using complete analytical mode shapes by (a) original MSEC method; (b) modified MSEC method.

After the suspected damaged elements are selected, the second step is to quantify the damage extent. The stiffness reduction factor α_j is computed by solving Eq. (3-10). The numbers J and P in Eq. (3-10) are equal to the number of suspected damaged elements. Each sensitivity coefficient β_{jp} in Eq. (3-10) is computed using the analytical information according to the intact FE model from Eq. (3-9). The MSEC in left-hand side of Eq. (3-10) is computed from Eq. (3-8). Table 4-5 summarized the stiffness reduction factors α_j obtained by five different combinations of modes.

Table 4-5: Identified percentage of element stiffness reduction (α_i) using original MSEC method with complete analytical mode shapes. The objective Ob_i is also shown.

| | Mode 1,4,6 | | | Mode 2,5,8 | | | Mode 3,7,9 | | | Mode 1,2,4,5,6,8 | | | Mode 1~9 | |
Element No.	Estimated α_i	Real α_i	Element No.	Estimated α_i	Real α_i	Element No.	Estimated α_i	Real α_i	Element No.	Estimated α_i	Real α_i	Element No.	Estimated α_i	Real α_i
1	-19.2%	-20.0%	1	-6.0%	-6.0%	1	-11.5%	-	1	-7.7%	-	1	-9.9%	-
2	-19.2%	-20.0%	2	-6.0%	-6.0%	2	-11.5%	-	2	-7.7%	-	2	-9.9%	-
13	-0.1%	0.0%	3	0.0%	0.0%	15	0.1%	0.0%	3	0.4%	0.0%	3	-0.7%	0.0%
14	-0.1%	0.0%	4	0.0%	0.0%	16	0.1%	0.0%	4	0.4%	0.0%	4	-0.7%	0.0%
						20	-2.5%	0.0%				15	0.1%	0.0%
						32	-0.8%	0.0%				16	0.1%	0.0%

Mode	$Ob_i \times 10^4$	Mode	$Ob_i \times 10^4$	Mode	$Ob_i \times 10^4$	Mode	$Ob_i \times 10^4$	Mode	$Ob_i \times 10^4$
X1	0.11	X1	15.90	X1	6.39	X1	11.67	X1	8.49
Y1	0.38	Y1	0.03	Y1	0.03	Y1	0.01	Y1	0.02
T1	0.20	T1	3.37	T1	1.13	T1	2.44	T1	1.77
X2	0.05	X2	26.15	X2	9.34	X2	19.59	X2	14.52
Y2	3.19	Y2	0.03	Y2	0.47	Y2	0.03	Y2	0.33
X3	0.03	X3	20.23	X3	7.25	X3	14.93	X3	10.78
T2	1.09	T2	2.70	T2	0.72	T2	1.86	T2	1.08
Y3	2.86	Y3	0.03	Y3	0.43	Y3	0.04	Y3	0.31
T3	1.11	T3	0.73	T3	0.05	T3	0.45	T3	0.10

In Table 4-5, the stiffness reduction factors obtained by the combination of three X-directional modes looks quite reasonable, since they relate to the reduction of I_z of the 1st and 2nd elements, which is a reduction of approximately 20%. Note that the objective, e.g. Ob_i, of the corresponding X-directional modes (with gray background in Table 4-5) were close to zero, while most of Ob_i of the other modes were not. Similarly, the stiffness reduction factors of the 1st and 2nd element obtained by the combination of three Y-directional modes (with gray background in Table 4-5) were 6%, and the corresponding Ob_i were close to zero.

The stiffness reduction factors of the 1st and 2nd elements obtained from the combination of three torsion modes, the combination of six X- and Y-directional modes, and the combination of all the nine modes were between 20% and 6%, and the stiffness reduction factors of the other elements were slightly disturbed, leading to confusing and unreliable results. This is because the original MSEC method yields the "lump sum" stiffness reduction of the elements, which is not the true damage state of the numerical FE model. The results obtained by different combinations of modes using original MSEC method are divergent. The Ob_i of corresponding modes (with gray background in Table 4-5) was not close to zero, also indicating unreliable results.

Modified MSEC Method

The procedure of damage localization and quantification using modified MSEC method was very similar to that of using original MSEC method. The $MSECR_j$ of each element was also obtained using Eq. (3-1), Eq. (3-11) and Eq. (3-3), except that the MSE of each element was replaced by the MSE contributed by different sectional properties of each element, *i.e.* A, I_z, I_y, and I_x. Figure 4-8(b) depicts the damage localization results using modified MSEC method with MSECR plotted against the element number, where each element number has 4 bars with respect to sectional properties in sequence A, I_z, I_y, and I_x. The elemental sectional properties with MSECR > 0.05 were chosen as suspected damaged elemental sectional properties. For example, the MSECR of six sectional properties exceeded the limit in the first combination of mode 1, 4 and 6, *i.e.* A and I_z of element 1, A and I_z of element 2, and I_z of elements 13 and 14. Different kinds of mode shapes (*e.g.* X-dir., Y-dir., and torsion) were found to relate to different sectional properties.

The stiffness reduction factors of these suspected damaged sectional properties were computed by solving Eq. (3-14) with considering Eq. (3-17) through (3-21). Table 4-6 summarizes the stiffness reduction factors obtained by the same 5 different combinations of modes. In Table 4-6, the stiffness reduction factors of the suspected damaged sectional properties obtained by combining three X-directional or Y-directional modes are almost identical to those of the designated factor, not only in terms of the corresponding sectional properties I_z or I_y respectively, but also in the axial sectional property. Like the results using original MSEC method, the Ob_i of corresponding X- or Y-directional modes obtained by these two combinations are close to zero, while most of Ob_i of the other modes are not. This is because the X- or Y-directional modes are only capable of identifying the corresponding sectional properties of these two elements, and cannot identify their other sectional properties.

Conversely, unlike the results using original MSEC method, the stiffness reduction factors obtained by the combination of torsional modes, the combination of X- and Y-directional modes, and also the combination of all nine modes are very close to the designated damage extent. The corresponding Ob_i of these three combinations distinctly indicate that the results are reliable, since the Ob_i of every mode is close to zero, indicating the mode shapes obtained from the calculated damaged stiffness matrix is

almost identical to the measured mode shapes in the damaged state. These findings indicate that the modified MSEC method can clearly identify the extent of damage to sectional properties of elements, rather than a vague damage extent of elements obtained by the original MSEC method. The Ob_i is verified as an easy way to judge the reliability of results. If all the Ob_i of corresponding modes are close to zero, the results are believed reliable.

Table 4-6. Identified percentage of element stiffness reduction (α_i) using modified MSEC method with complete analytical mode shapes. The objective Ob_i is also shown.

	Mode 1,4,6			Mode 2,5,8			Mode 3,7,9			Mode 1,2,4,5,6,8			Mode 1~9	
Sectional Property	Estimated α_i	Real α_i	Sectional Property	Estimated α_i	Real α_i	Sectional Property	Estimated α_i	Real α_i	Sectional Property	Estimated α_i	Real α_i	Sectional Property	Estimated α_i	Real α_i
'1_A'	-2.3%	-2.0%	'1_A'	-1.9%	-2.0%	'1_Iz'	-20.0%	-20.0%	'1_A'	-2.0%	-2.0%	'1_A'	-1.4%	-2.0%
'1_Iz'	-19.7%	-20.0%	'1_Iy'	-6.0%	-6.0%	'1_Iy'	-6.0%	-6.0%	'1_Iz'	-19.7%	-20.0%	'1_Iz'	-19.9%	-20.0%
'2_A'	-2.3%	-2.0%	'2_A'	-1.9%	-2.0%	'2_Iz'	-20.0%	-20.0%	'1_Iy'	-6.0%	-6.0%	'1_Iy'	-6.0%	-6.0%
'2_Iz'	-19.7%	-20.0%	'2_Iy'	-6.0%	-6.0%	'2_Iy'	-6.0%	-6.0%	'2_A'	-2.0%	-2.0%	'2_A'	-1.4%	-2.0%
'13_Iz'	0.0%	0.0%	'3_Iy'	0.0%	0.0%	'15_Iz'	0.0%	0.0%	'2_Iz'	-19.7%	-20.0%	'2_Iz'	-19.9%	-20.0%
'14_Iz'	0.0%	0.0%	'4_Iy'	0.0%	0.0%	'16_Iz'	0.0%	0.0%	'2_Iy'	-6.0%	-6.0%	'2_Iy'	-6.0%	-6.0%
									'3_Iy'	0.0%	0.0%	'3_Iy'	0.0%	0.0%
									'4_Iy'	0.0%	0.0%	'4_Iy'	0.0%	0.0%
									'13_Iz'	0.0%	0.0%	'15_Iz'	0.0%	0.0%
									'14_Iz'	0.0%	0.0%	'16_Iz'	0.0%	0.0%

Mode	$Ob_i \times 10^4$	Mode	$Ob_i \times 10^4$	Mode	$Ob_i \times 10^4$	Mode	$Ob_i \times 10^4$	Mode	$Ob_i \times 10^4$
X1	0.00	X1	19.22	X1	0.00	X1	0.00	X1	0.00
Y1	0.10	Y1	0.00	Y1	0.00	Y1	0.00	Y1	0.00
T1	0.04	T1	6.39	T1	0.00	T1	0.00	T1	0.00
X2	0.00	X2	50.94	X2	0.00	X2	0.00	X2	0.00
Y2	0.60	Y2	0.00	Y2	0.00	Y2	0.00	Y2	0.00
X3	0.01	X3	45.92	X3	0.00	X3	0.00	X3	0.00
T2	0.21	T2	6.92	T2	0.00	T2	0.00	T2	0.00
Y3	0.52	Y3	0.00	Y3	0.00	Y3	0.00	Y3	0.00
T3	0.18	T3	1.71	T3	0.00	T3	0.00	T3	0.00

4.1.2.5. Comparison between Original and Modified Iteration Process

To evaluate the performance of the proposed modified iteration process, the estimated stiffness reduction factors obtained by the original and modified iteration processes were compared. The complete DOFs of mode shapes obtained by dynamic expanding from the twelve measured DOFs (which are the same as those described in Section 4.1.1.1) via Eq. (2-59) and Eq. (2-60) were utilized in this section, both for the original and modified iteration processes. For simplicity, only the modified MSEC method was employed.

The MSECR of each elemental sectional property was calculated from Eq. (3-11) for the first nine individual modes. Figure 4-9 shows the damage localization results, and the elemental sectional property with MSECR > 0.05 in the 1st, 3rd and 4th modes and with MSECR > 0.01 in the 2nd, 5th and the 6th modes were chosen as suspected damaged elements. Here, the performance of the proposed modified iteration process is illustrated by using the suspected damaged sectional properties selected in the 1st mode, *i.e.* I_z of element 1, I_z of element 2, and I_y of element 5 selected from the 1st bar chart of Figure 4-9. Only the modal information of the 1st mode is used to solve the stiffness reduction factors. Figures 4-10(a) and 4-10(b) illustrate the stiffness reduction factors obtained by the original and modified iteration process at each step, respectively. The original iteration process converged very quickly but the results were poor. For example, the sectional property I_y of element 5 exhibited no damage, but the result was that the stiffness was reduced by approximately 10%. Conversely, the results of modified iteration process converged to the destined reduction value after around 30 iterations. The modified iteration process, which updated the target modal parameters according to the current model state, was found to be a much better iteration process than the original process.
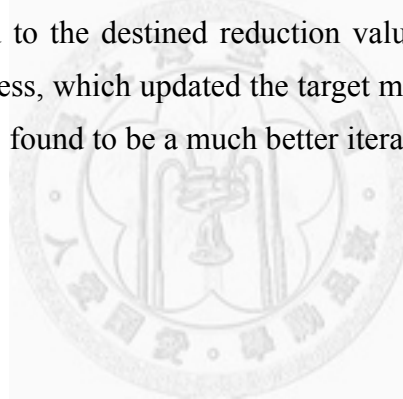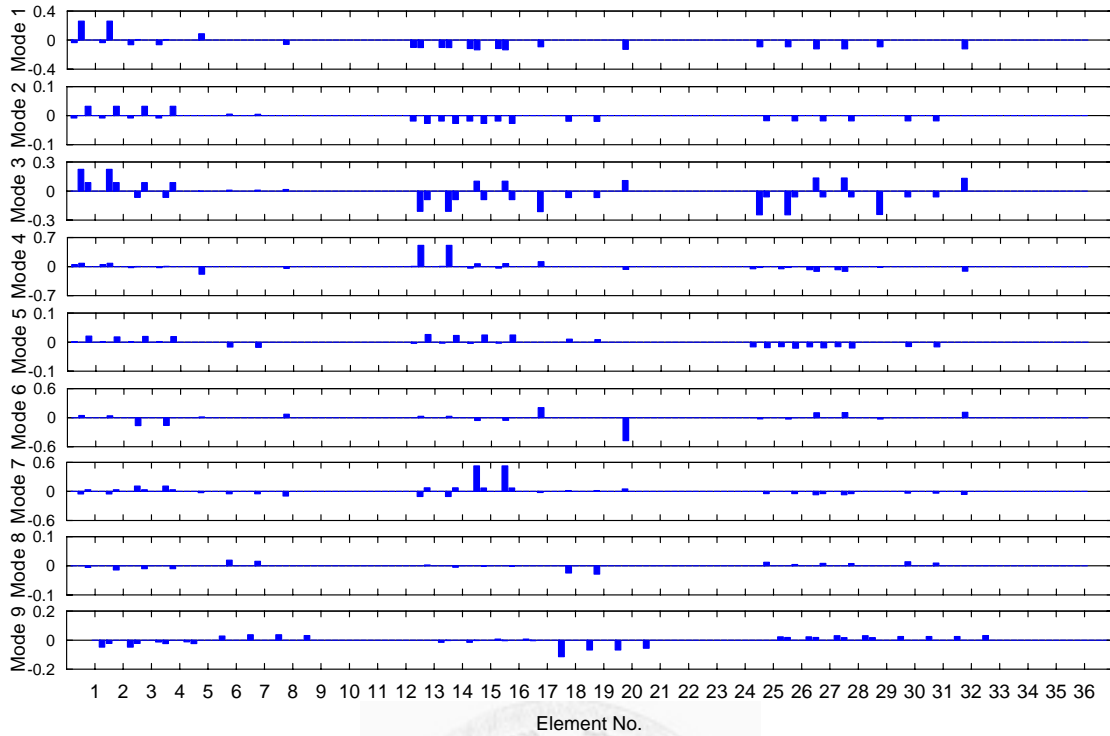
Figure 4-9: Damage localization results of the 3D target structure using dynamic expanded analytical mode shapes by modified MSEC method.
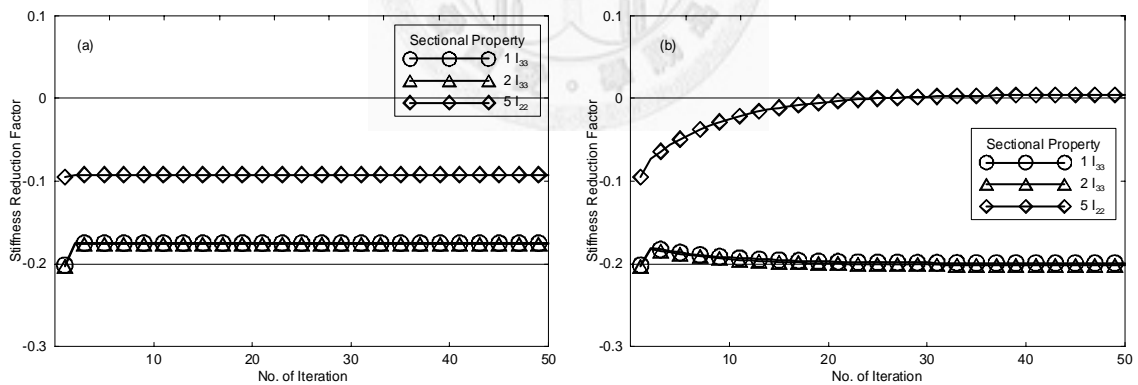
Figure 4-10: Iteration process for damage quantification: (a) original method; (b) proposed method.

4.1.2.6. Study of the Effect Caused by Modal Expansion with Limited Measurement of the Target Structure

Numerical results of Section 4.1.2.4 and 4.1.2.5 have demonstrated that the modified MSEC method and iteration processes performed better than the original method.

Therefore the modified MSEC method and iteration processes were utilized in this section to investigate the effect caused by modal expansion with a few measurements. The dynamic expanded mode shapes were utilized, instead of the analytical mode shapes with complete DOFs.

The results of damage localization were the same as those in the previous section. Figure 4-9 in Section 4.1.2.5 shows these results and reveals that the lower modes can clearly provide information to locate the damaged sectional properties, while the higher modes cannot do so. Therefore, the information of damage location from higher modes should not be considered in the experimental study of the target structure. However, if the damage section properties relate only to some higher mode shapes in other damage cases, maybe the higher modes should be considered rather than the lower ones.

Table 4-7 presents the stiffness reduction factor α_j and the objective Ob_i obtained by individual 1st, 2nd, 3rd, 4th, 5th, 6th and 7th mode, while the localization using other individual modes was failed, and therefore not shown. The iteration number of each mode is also listed in Table 4-7. The stiffness reduction of sectional properties I_z of elements 1 and 2 were correctly identified by the first three X-directional modes and the 1st torsional mode, while the stiffness reduction of sectional properties I_y of elements 1 and 2 were distributed to I_y of elements 3 and 4 in the 1st Y-directional mode and the 1st torsional mode. The stiffness reduction of sectional properties obtained by the 2nd Y-directional mode and 2nd torsional mode were not so close to the true one. This reveals again that higher modes are too sensitive to be expanded with only limited measurements, and therefore large error is introduced. The stiffness reduction of sectional properties A of elements 1 and 2 were incorrect, because no vertical DOFs were measured. The results of damage quantification using individual mode help understand the effect of dynamic expansion with limited measurement of the target structure and also the possible modes to be utilized in the following experimental study to identify the damage of the real target structure.

It is worth to be mentioned that if α is obtained by Eq. (3-10) where no eigenvalue was included rather than by Eq. (3-14) where eigenvalue was included, the results obtained by the 3rd or the 4th modal information individually disperse, while the results obtained by the 1st, 2nd, 5th, 6th or the 7th modal information individually did not change

too much. This reveals the benefit of suppressing the ill-posed problem by including eigenvalue in Eq. (3-14).

Table 4-7: Identified percentage of element stiffness reduction (α_i) using modified MSEC method with dynamic expanded mode shapes. The objective Ob_i is also shown.

Mode 1 (ITE=50)			Mode 2 (ITE=60)			Mode 3 (ITE=4)			Mode 4 (ITE=5)		
Sectional Property	Estimated α_i	Real α_i	Sectional Property	Estimated α_i	Real α_i	Sectional Property	Estimated α_i	Real α_i	Sectional Property	Estimated α_i	Real α_i
'1_Iz'	-19.9%	-20.0%	'1_Iy'	-3.0%	-6.0%	'1_Iz'	-20.5%	-20.0%	'1_A'	21.0%	-2.0%
'2_Iz'	-20.2%	-20.0%	'2_Iy'	-3.0%	-6.0%	'1_Iy'	-3.0%	-6.0%	'1_Iz'	-18.5%	-20.0%
'5_Iy'	0.5%	0.0%	'3_Iy'	-3.1%	0.0%	'2_Iz'	-20.7%	-20.0%	'2_A'	21.0%	-2.0%
			'4_Iy'	-3.1%	0.0%	'2_Iy'	-3.1%	-6.0%	'2_Iz'	-19.1%	-20.0%
			'6_Iy'	0.0%	0.0%	'3_Iz'	-3.0%	0.0%	'13_Iz'	3.8%	0.0%
			'7_Iy'	0.0%	0.0%	'3_Iy'	-2.9%	0.0%	'14_Iz'	2.5%	0.0%
						'4_Iz'	0.0%	0.0%	'15_Iz'	1.9%	0.0%
						'4_Iy'	0.1%	0.0%	'16_Iz'	2.0%	0.0%
						'5_Iy'	0.0%	0.0%	'17_Iy'	0.6%	0.0%
						'6_Iy'	-0.3%	0.0%			
						'7_Iy'	-0.4%	0.0%			
						'8_Iy'	3.2%	0.0%			

Mode	$Ob_i \times 10^4$	Mode	$Ob_i \times 10^4$	Mode	$Ob_i \times 10^4$	Mode	$Ob_i \times 10^4$
X1	0.00	X1	19.28	X1	0.00	X1	0.00
Y1	0.10	Y1	0.00	Y1	0.00	Y1	0.10
T1	0.04	T1	6.39	T1	0.00	T1	0.03
X2	0.00	X2	50.77	X2	0.00	X2	0.00
Y2	0.60	Y2	0.00	Y2	0.00	Y2	0.60
X3	0.00	X3	45.79	X3	0.00	X3	0.00
T2	0.20	T2	6.92	T2	0.00	T2	0.21
Y3	0.52	Y3	0.00	Y3	0.00	Y3	0.52
T3	0.18	T3	1.73	T3	0.00	T3	0.18

Mode 5 (ITE=1)			Mode 6 (ITE=2)			Mode 7 (ITE=1)					
Sectional Property	Estimated α_i	Real α_i	Sectional Property	Estimated α_i	Real α_i	Sectional Property	Estimated α_i	Real α_i	Sectional Property	Estimated α_i	Real α_i
'1_Iy'	-1.1%	-5.5%	'1_Iz'	-23.1%	-20.3%	'1_Iy'	-19.0%	-5.5%	'15_Iz'	32.8%	0.0%
'2_Iy'	-1.3%	-5.5%	'2_Iz'	-23.1%	-20.3%	'2_Iy'	-29.9%	-5.5%	'15_Iy'	-12.3%	0.0%
'3_Iy'	-2.6%	0.0%	'8_Iy'	-1.3%	0.0%	'3_Iz'	4.4%	0.0%	'16_Iz'	32.0%	0.0%
'4_Iy'	-2.5%	0.0%	'17_Iy'	15.2%	0.0%	'3_Iy'	-5.4%	0.0%	'16_Iy'	9.1%	0.0%
'13_Iy'	-4.3%	0.0%	'27_Iz'	7.5%	0.0%	'4_Iz'	4.0%	0.0%	'18_Iy'	0.0%	0.0%
'14_Iy'	-4.7%	0.0%	'27_Iy'	7.5%	0.0%	'4_Iy'	5.4%	0.0%	'19_Iy'	-0.1%	0.0%
'15_Iy'	-7.7%	0.0%	'31_Iy'	7.1%	0.0%	'13_Iy'	-39.5%	0.0%	'20_Iy'	3.5%	0.0%
'16_Iy'	-7.4%	0.0%				'14_Iy'	-61.0%	0.0%			

Mode	$Ob_i \times 10^4$	Mode	$Ob_i \times 10^4$	Mode	$Ob_i \times 10^4$
X1	19.28	X1	12.35	X1	4.76
Y1	0.12	Y1	0.10	Y1	5.04
T1	6.66	T1	2.09	T1	9.10
X2	50.77	X2	22.51	X2	81.54
Y2	0.02	Y2	0.60	Y2	19.82
X3	45.78	X3	12.11	X3	86.46
T2	6.80	T2	4.28	T2	0.85
Y3	0.10	Y3	0.52	Y3	30.09
T3	1.58	T3	2.96	T3	4.29

4.1.3. Experimental Validation

After the proposed modified MSEC method was validated through the numerical studies in the previous section, the feasibility of the application of the proposed MSEC method to the target structure described in Section 4.1.1 was studied in this section. Due to the limited measurement as discussed in 4.1.1.1, the difficulty of damage detection of the target structure was anticipated, which has also been discussed via numerical studies in Section 4.1.2.6. The performance of the original method was also studied in this section. However, since some of the proposed modifications of the original MSEC method had been verified through the numerical studies in Section 4.1.2 including: (i) taking non-absolute MSECR for damage localization; (ii) using dynamic expansion to expand incomplete measured mode shapes; (iii) setting threshold to exclude elements with small MSE to avoid abnormal results of damage localization and quantification; (iv) an modified iteration process, these modifications were employed also by the original MSEC method here.

4.1.3.1. Modified MSEC Method

Damage Localization

The measured mode shapes of the target structure in intact and damaged states were employed to calculate MSECR using Eq. (3-1) and Eq. (3-11). In order to erase the abnormal MSECR, the threshold of MSE, C_{MSE}, should be determined in advance. Owing to the noise and other disturbance in the test, this threshold was determined much larger than the one in Section 4.1.2.6. If C_{MSE} was chosen as 0.05, which is the same as the one in Section 4.1.2.6, some abnormal MSECR were induced. Therefore, the threshold was finally set to 0.3 in this experimental study to exclude the abnormal MSECR. The individual modes were used to determine the damage locations. Similarly, the sectional properties with MSECR > 0.05 in the 1st, 3rd and 4th modes and with MSECR > 0.01 in the 2nd and the 6th modes as shown in Figure 4-11 were chosen to calculate the stiffness reduction factors. The damage localization using the other individual modes was failed.

Figure 4-11: Experimental damage localization results of the target structure using modified MSEC method.

Damage Quantification

The measured mode shapes and eigenfrequencies of the target structure in both intact and damaged states were applied for damage quantification. Table 4-8 presents the stiffness reduction factors obtained using individual modes. These results indicate that the stiffness reduction of sectional properties I_z of elements 1 and 2 were properly identified by the first three X-direction modes and the 1st torsional mode. However, the other sectional properties of other elements were identified as some moderate amount of stiffness reduction or "increasing", which may be caused by modal expansion, modeling error and noise effect. The combination of any modes did not improve the results of damage quantification, and hence is not shown here.

The results obtained by the modified MSEC method but excluding eigenvalue in Eq. (3-14) are also shown in Table 4-9. It is evident that all the results are distorted. Again, the effects to suppress ill-posed problem by including eigenvalue in Eq. (3-14) are illustrated.

90

Table 4-8: Identified percentage of element stiffness reduction (α_i) from experimental damage detection using modified MSEC method. The objective Ob_i is also shown.

Mode 1 (ITE=1)			Mode 2 (ITE=1)			Mode 3 (ITE=1)			Mode 4 (ITE=1)		
Sectional Property	Estimated α_i	Real α_i	Sectional Property	Estimated α_i	Real α_i	Sectional Property	Estimated α_i	Real α_i	Sectional Property	Estimated α_i	Real α_i
'1_Iz'	-18.3%	-20.3%	'1_Iy'	-2.5%	-5.5%	'1_Iz'	-19.9%	-20.3%	'1_Iz'	-18.8%	-20.3%
'2_Iz'	-18.9%	-20.3%	'2_A'	-1.9%	-2.5%	'1_Iy'	-4.1%	-5.5%	'2_Iz'	-20.9%	-20.3%
'5_Iy'	-9.5%	0.0%	'2_Iy'	-2.3%	-5.5%	'2_Iz'	-20.5%	-20.3%	'13_Iz'	12.1%	0.0%
			'3_A'	-2.2%	0.0%	'3_Iz'	-2.3%	0.0%	'14_Iz'	8.1%	0.0%
			'3_Iy'	-1.8%	0.0%	'3_Iy'	0.6%	0.0%	'15_Iz'	-14.2%	0.0%
			'4_Iy'	-2.8%	0.0%	'4_Iz'	-3.0%	0.0%	'17_Iy'	1.8%	0.0%
			'25_Iy'	-4.2%	0.0%	'6_Iy'	-1.8%	0.0%			
			'30_Iy'	-2.7%	0.0%	'13_Iy'	1.1%	0.0%			
						'15_Iy'	-2.3%	0.0%			
						'18_Iy'	-1.5%	0.0%			
						'26_Iy'	-4.1%	0.0%			
						'28_Iy'	-3.5%	0.0%			

Mode	$Ob_i \times 10^4$	Mode	$Ob_i \times 10^4$	Mode	$Ob_i \times 10^4$	Mode	$Ob_i \times 10^4$
X1	4.05	X1	27.87	X1	4.76	X1	10.42
Y1	6.95	Y1	6.02	Y1	8.01	Y1	6.94
T1	127.10	T1	129.04	T1	4.76	T1	122.05
X2	11.09	X2	74.40	X2	7.36	X2	14.02
Y2	32.47	Y2	31.09	Y2	32.19	Y2	32.47
X3	6.81	X3	54.15	X3	5.57	X3	27.37
T2	46.91	T2	63.54	T2	46.08	T2	45.56
Y3	26.81	Y3	29.63	Y3	26.84	Y3	26.80
T3	41.07	T3	52.49	T3	33.99	T3	43.21

Mode 6 (ITE=3)		
Sectional Property	Estimated α_i	Real α_i
'1_Iz'	-20.2%	-20.3%
'2_Iz'	-29.8%	-20.3%
'5_Iy'	55.2%	0.0%
'8_Iy'	1.0%	0.0%
'13_Iz'	9.0%	0.0%
'14_Iz'	5.7%	0.0%
'27_Iz'	4.0%	0.0%
'28_Iz'	5.8%	0.0%
'32_Iy'	3.6%	0.0%

Mode	$Ob_i \times 10^4$
X1	7.71
Y1	6.94
T1	122.10
X2	9.14
Y2	32.47
X3	10.31
T2	39.92
Y3	26.80
T3	35.28

Table 4-9: Identified percentage of element stiffness reduction (α_i) from experimental damage detection using modified MSEC method but without eigenvalue. The objective Ob_i is also shown.

Mode 1 (ITE=16)			Mode 2 (ITE=2)			Mode 3 (ITE=1)			Mode 4 (ITE=1)		
Sectional Property	Estimated α_i	Real α_i	Sectional Property	Estimated α_i	Real α_i	Sectional Property	Estimated α_i	Real α_i	Sectional Property	Estimated α_i	Real α_i
'1_Iz'	-8.6%	-20.3%	'1_Iy'	-19.8%	-5.5%	'1_Iz'	-24.0%	-20.3%	'1_Iz'	36.5%	-20.3%
'2_Iz'	-43.2%	-20.3%	'2_A'	-2.9%	-2.5%	'1_Iy'	51.8%	-5.5%	'2_Iz'	34.6%	-20.3%
'5_Iy'	12.5%	0.0%	'2_Iy'	-15.7%	-5.5%	'2_Iz'	-21.3%	-20.3%	'13_Iz'	-89.2%	0.0%
			'3_A'	-3.8%	0.0%	'3_Iz'	10.4%	0.0%	'14_Iz'	-92.4%	0.0%
			'3_Iy'	-18.0%	0.0%	'3_Iy'	41.4%	0.0%	'15_Iz'	40.4%	0.0%
			'4_Iy'	-17.2%	0.0%	'4_Iz'	12.6%	0.0%	'17_Iy'	-33.2%	0.0%
			'25_Iy'	-9.9%	0.0%	'6_Iy'	52.6%	0.0%			
			'30_Iy'	-5.1%	0.0%	'13_Iy'	59.0%	0.0%			
						'15_Iy'	63.7%	0.0%			
						'18_Iy'	76.4%	0.0%			
						'26_Iy'	-34.5%	0.0%			
						'28_Iy'	-36.0%	0.0%			

Mode	$Ob_i \times 10^4$	Mode	$Ob_i \times 10^4$	Mode	$Ob_i \times 10^4$	Mode	$Ob_i \times 10^4$
X1	3.43	X1	27.07	X1	12.40	X1	868.31
Y1	7.02	Y1	1.73	Y1	1228.12	Y1	7.01
T1	125.72	T1	132.31	T1	27.93	T1	502.08
X2	7.60	X2	70.93	X2	40.76	X2	763.15
Y2	32.80	Y2	15.53	Y2	1222.81	Y2	9999.98
X3	7.08	X3	51.79	X3	45.94	X3	9999.98
T2	44.83	T2	41.14	T2	291.08	T2	95.89
Y3	26.97	Y3	18.67	Y3	2557.97	Y3	26.99
T3	38.62	T3	33.82	T3	540.42	T3	94.18

Mode 6 (ITE=2)		
Sectional Property	Estimated α_i	Real α_i
'1_Iz'	-24.5%	-20.3%
'2_Iz'	-29.7%	-20.3%
'5_Iy'	35.7%	0.0%
'8_Iy'	0.5%	0.0%
'13_Iz'	3.1%	0.0%
'14_Iz'	1.4%	0.0%
'27_Iz'	1.2%	0.0%
'28_Iz'	2.8%	0.0%
'32_Iy'	1.3%	0.0%

Mode	$Ob_i \times 10^4$
X1	4.16
Y1	7.03
T1	124.08
X2	7.87
Y2	32.81
X3	6.69
T2	42.15
Y3	26.98
T3	36.38

4.1.3.2. Original MSEC Method

The damage detection using original MSEC method was also conducted for comparison. Note that the proposed modifications of the original MSEC method verified through the numerical studies in Sections 4.1.2.1, 4.1.2.2, 4.1.2.3 and 4.1.2.5 were employed also by the original MSEC method here. In other words, the only difference between the original MSEC method and modified MSEC method employed in this section are the including of eigenvalue in Eq. (3-14) and the expansion of element stiffness to sectional properties as described in Section 3.1.2.3.

Damage Localization

The measured mode shapes of the target structure in intact and damaged states were employed to calculate MSECR for individual modes using Eq. (3-1) and Eq. (3-11). The threshold of MSE, C_{MSE}, was determined as 0.3 which was the same as the one in Section 4.1.3.1. The individual modes were used to determine the damage locations. Similarly, the sectional properties with MSECR > 0.05 in the 1st, 3rd and 4th modes and with MSECR > 0.01 in the 2nd and the 6th modes as shown in Figure 4-12 were chosen to calculate the stiffness reduction factors. The damage localization using the other individual modes was failed.
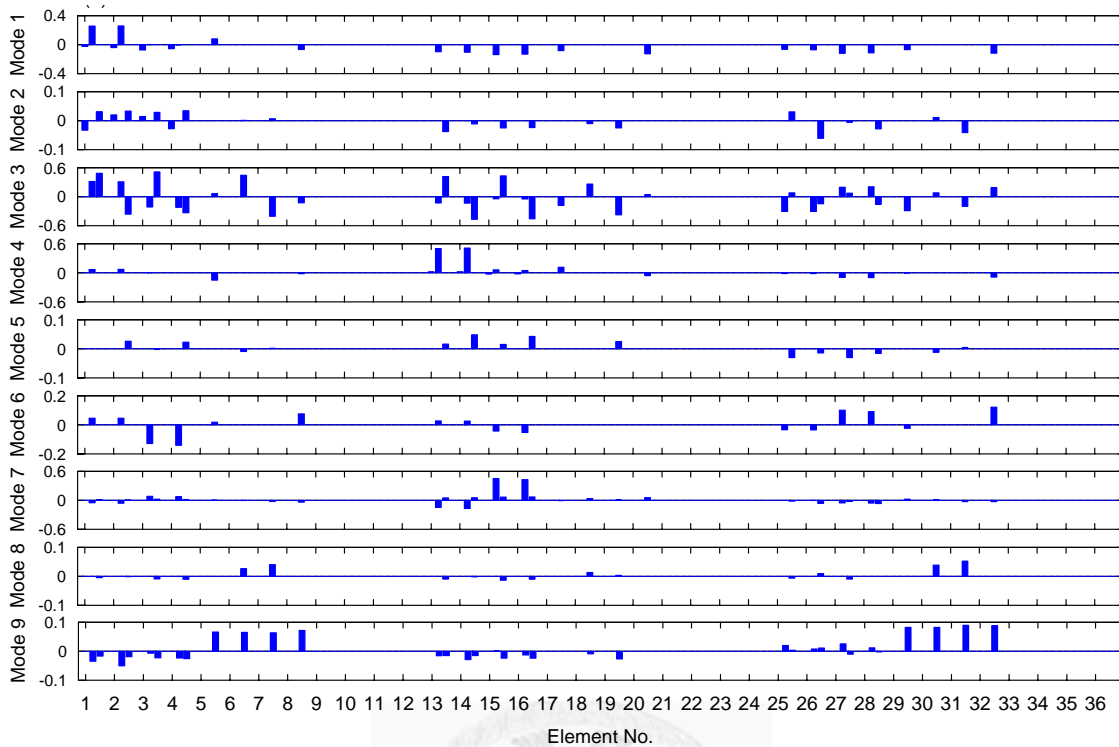
Damage Quantification

The measured mode shapes and eigenfrequencies of the target structure in both intact and damaged states were applied for damage quantification. Table 4-10 presents the stiffness reduction factors obtained using individual modes. The combination of any modes did not improve the results of damage quantification, hence is not shown here. The results obtained using individual modes were divergent, leading to confusing results. Comparing the results in Table 4-10 and Table 4-8, it can be observed that the results obtained by modified MSEC method were more accurate than the one obtained by original MSEC method.
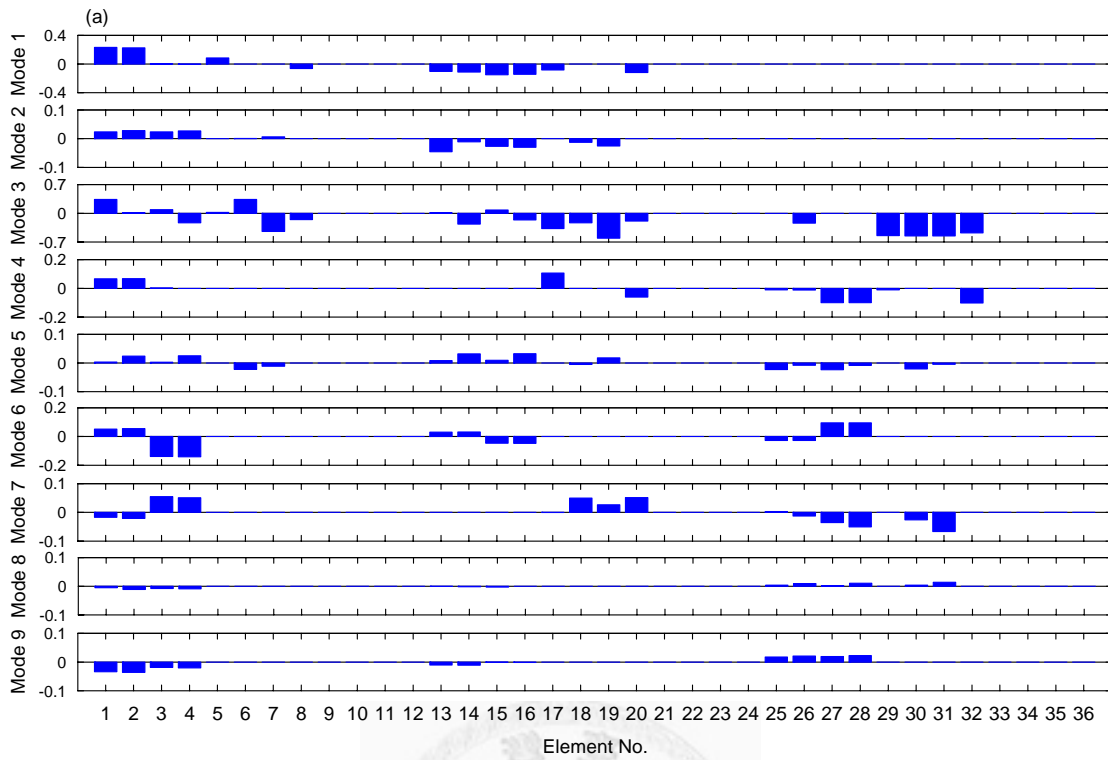
Figure 4-12: Experimental damage localization results of the target structure using original MSEC method.

Table 4-10: Identified percentage of element stiffness reduction (α_i) from experimental damage detection using original MSEC method. The objective Ob_i is also shown.

Mode 1 (ITE=1)			Mode 2 (ITE=1)			Mode 3 (ITE=1)			Mode 4 (ITE=1)		
Element	Estimated α_i	Real α_i	Element	Estimated α_i	Real α_i	Element	Estimated α_i	Real α_i	Element	Estimated α_i	Real α_i
1	-15.9%	-20.3%	1	-1.8%	-5.5%	1	-25.2%	-	1	-9.6%	-20.3%
2	-16.0%	-20.3%	2	-2.2%	-5.5%	2	-22.2%	-	2	-10.2%	-20.3%
5	-7.9%	0.0%	3	-1.9%	0.0%	3	10.9%	0.0%	17	-4.0%	0.0%
			4	-2.0%	0.0%	5	-18.0%	0.0%			
						6	-4.4%	0.0%			
						13	-8.6%	0.0%			
						15	4.1%	0.0%			

Mode	$Ob_i \times 10^4$	Mode	$Ob_i \times 10^4$	Mode	$Ob_i \times 10^4$	Mode	$Ob_i \times 10^4$
X1	5.30	X1	25.82	X1	34.56	X1	7.77
Y1	4.32	Y1	6.44	Y1	5.80	Y1	5.42
T1	128.64	T1	127.01	T1	6.80	T1	126.40
X2	14.38	X2	64.40	X2	41.29	X2	31.83
Y2	16.18	Y2	28.13	Y2	1.31	Y2	21.74
X3	7.35	X3	47.47	X3	31.33	X3	16.27
T2	36.76	T2	58.16	T2	5.54	T2	46.17
Y3	12.51	Y3	23.01	Y3	0.41	Y3	17.43
T3	32.16	T3	47.74	T3	1.60	T3	39.21

Mode 6 (ITE=1)		
Element	Estimated α_i	Real α_i
1	-45.4%	-20.3%
2	-45.4%	-20.3%
27	15.6%	0.0%
28	15.4%	0.0%

Mode	$Ob_i \times 10^4$
X1	207.15
Y1	4.38
T1	185.20
X2	125.30
Y2	19.85
X3	52.77
T2	34.12
Y3	14.21
T3	17.16

4.2. Frequency Response Function Change Method

At frst, the feasibility of the proposed FRFC method for damage localization and quantification was studied through a numerical simulation of a 2D 6-story shear building. Both the effects of measurement noise and modeling error were considered. Efforts were made to reduce the error caused by measurement noise and modeling error.

The FRFC method was further validated via a 1/4-scale 6-story steel building structure designed by NCREE. A set of special connecting plates between bracings and floor plates in the structure could be replaced by smaller ones or be removed quickly at each story to simulate damage.

To realize the idea of integrating FRFC method with wireless sensing systems as proposed in Section 3.2.2, another experimental validation was carried out. The feasibility and energy efficiencies of the proposed on-line damage detection operation scheme were investigated.

4.2.1. Numerical Validation

4.2.1.1. Test Structure Description

The FE model of a 2D 6-story shear building was constructed using 6 beam elements whose properties can be summarized as: $E = 2.039 \times 10^{11} \, N/m^2$, $I = 3.906 \times 10^{-7} \, N/m^2$, and $A = 3.6 \times 10^{-3} \, m^2$. The stiffness of each story is 955,720 N/m. The lumped mass of each floor is 439.8 kg. The damping matrix is decided Rayleigh damping on the assumption that the damping ratios of the first two modes are 2%. The six eigenfrequencies are 1.7887 Hz, 5.2620 Hz, 8.4296 Hz, 11.1073 Hz, 13.1394 Hz, and 14.4080 Hz. The damage is assumed to be occurred at the first story with 50% loss of stiffness.

The 6-story shear building was assumed to be subjected to white noise ground excitations with sampling rate 200 Hz and time duration 50 sec. All the acceleration response time-history of 6 stories were assumed measured with the same sampling rate and length, *i.e.* 10000 points.

4.2.1.2. Effects of Measurement Noise

In order to study the effects caused by measurement noise on the damage detection of the proposed FRFC method, normally distributed noise with 2% and 5% of noise level were added to both the input and output acceleration signals. The noise Level is defined as

$$NL = (\sigma_n / \sigma_s) \times 100(\%) \tag{4-2}$$

where σ_s represents the standard deviation of the signal without noise, and σ_n represents the standard deviation of the noise. Totally 1000 samples were generated for each noise level. The "measured" displacement FRFs between each story and ground floor were calculated by Eq. (3-39) and divided by square of circular frequencies. Note that when solving Eq. (3-38), it is easy to reduce the ill-posed problem by including more equations as described in Section 3.2. Therefore, here the variation of stiffness of each story at different frequencies was identified by solving Eq. (3-38) with 11 successive frequencies at each frequency (22 equations). Figure 4-13(a) shows the variation of the identified stiffness at different frequencies from one of the sample under 2% noise level and Figure 4-13(b) shows the corresponding displacement FRFs. Note that the variation of stiffness was divided by minus of the original story stiffness; hence the plus value represents the percentage of stiffness loss. The solid line in Figure 4-13(a) represents the stiffness variation of the first story and should be 50% while the other lines represent the stiffness variation of the 2nd to 6th stories and should be 0%. Obviously these lines flutter because of noise effects. However, it is evident that the results around the eigenfrequencies of the damaged structure which are marked with solid vertical lines in both Figure 4-13(a) and Figure 4-13(b) suffer much less noise effects. It is because that the signal to noise ratio of FRFs is larger around the eigenfrequencies of the damaged structure. Therefore, it is suggested to select the FRFs around the eigenfrequencies of the damaged structure to calculate the stiffness variation.

Because the least-square solution of Eq. (3-38) is dominated by equations with larger coefficients, the information at frequencies with smaller amplitude of FRFs will be

overshadowed. To overcome this shortcoming, one can simply solve the equations with several frequencies around each eigenfrequency, and then take average of all the results obtained around 6 eigenfrequencies. The least-square solution using 11 frequencies around each eigenfrequency and also the average of all the results obtained using FRFs around 6 eigenfrequencies of one of the numerical sample under 2% measurement noise is listed in Table 4-11. It can be observed that there are some abnormal identified stiffness variations. For example, the identified 4th story stiffness variations of the 3rd mode is 20.1%, therefore the mean value of the 4th story seems to be affected by this abnormal value a lot. In order to obtain more reliable results with less effect caused by abnormal value, a results similarity criterion (RSC) is proposed. The RSC weights the identified story stiffness variations obtained by each mode according to their similarity to the median value of each story as shown in the following equations:

$$\Delta\hat{\kappa}_i = \sum_{j=1}^{p} \Delta\kappa_{ij} \times w_{ij} \qquad (4\text{-}3)$$

$$w_{ij} = \exp(-2(\Delta\kappa_{ij} - \Delta\hat{\kappa}_i)^2 / (\sigma_i)^2) \qquad (4\text{-}4)$$

$$\sigma_i = \sqrt{\sum_{j=1}^{p} (\Delta\kappa_{ij} - \Delta\tilde{\kappa}_i)^2} \qquad (4\text{-}5)$$

where $\Delta\hat{\kappa}_i$ represents the weighted identified stiffness variations of the ith story; $\Delta\kappa_{ij}$ represents the identified stiffness variations of the ith story using frequencies around mode j; w_{ij} represents the weighting determined by the similarity measurement result of each $\Delta\kappa_{ij}$; σ represents the standard deviation between the identified stiffness variations $\Delta\kappa_{ij}$ and the mdeian of identified stiffness variations $\Delta\tilde{\kappa}_i$; p represents the number of identified modes. The results weighted according to Eq. (4-3) to (4-5) are also listed in Table 4-11. By multiplying the abnormal results with less weighting, the weighted identified stiffness variations were much closer to the median value of other "normal" results, and therefore more reliable results can be obtained without the interference of the abnormal results.

Table 4-12 lists mean and standard deviation of both the calculated "average" and

"weighted" stiffness variations obtained by the 1000 samples under two different noise levels. For both the 2% and 5% noise levels, the "weighted" stiffness variations suffer much less errors caused by measurement noise than the "averaged" one. This demonstrates that the proposed weighting procedure RSC can reduce the error caused by some abnormal results. Therefore all the results of following studies were obtained by taking weighted results obtained around different eigenfrequencies using the RSC. For the 2% noise level, the standard deviation of the "weighted" results remains less than 2.5% which is quite reliable. As the noise Level-Increases to 5%, the identification accuracy becomes only moderate with about 5% of both standard deviation and biased mean value.
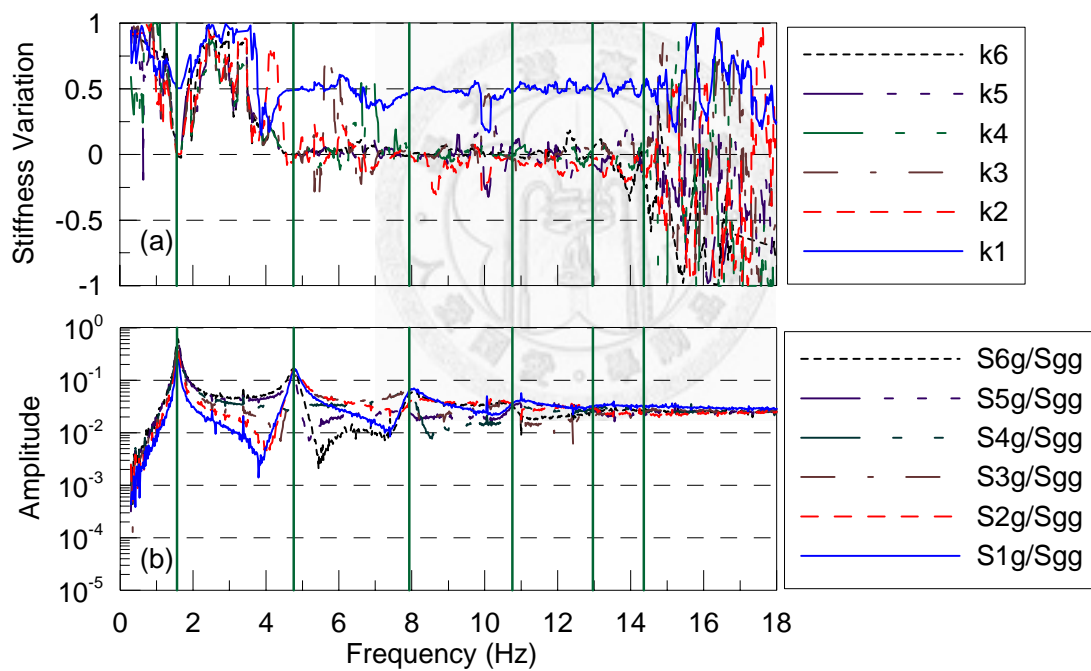
Figure 4-13: Typical FRFC results under 2% noise level: (a) identified stiffness variation; (b) FRFs

Table 4-11: One of the identified stiffness variation under 2% noise level.

Story Number	Mode 1	2	3	4	5	6	Average	RSC	Designated
1	50.6%	50.2%	46.9%	45.1%	50.0%	44.5%	47.9%	48.5%	50.0%
2	1.4%	14.9%	4.0%	-0.4%	-8.1%	-2.1%	1.6%	0.4%	0.0%
3	1.0%	-1.6%	1.7%	1.7%	3.4%	-1.5%	0.8%	0.9%	0.0%
4	3.6%	-0.8%	20.1%	1.6%	0.5%	9.5%	5.7%	1.2%	0.0%
5	2.0%	0.1%	-2.8%	9.2%	0.9%	-10.7%	-0.2%	0.4%	0.0%
6	4.4%	-0.9%	-1.1%	-2.2%	-2.0%	-6.8%	-1.4%	-1.6%	0.0%

Table 4-12: Mean and standard deviation of the identified stiffness variation of 1000 samples under different noise levels in measurement.

Story Number	NL=2% Average mean	std	RSC mean	std	NL=5% Averaged mean	std	RSC mean	std	Designated Value
1	49.0%	3.2%	49.1%	1.3%	46.6%	8.5%	49.0%	3.6%	50.0%
2	-2.4%	5.4%	-1.0%	2.3%	4.7%	10.3%	2.8%	5.7%	0.0%
3	2.8%	3.7%	1.7%	1.6%	5.6%	6.9%	4.2%	4.2%	0.0%
4	0.2%	4.3%	0.9%	1.6%	5.4%	10.2%	3.8%	4.9%	0.0%
5	3.4%	4.8%	1.3%	1.9%	8.0%	9.6%	4.0%	5.8%	0.0%
6	-1.9%	5.2%	0.3%	1.0%	-1.5%	8.4%	0.5%	2.6%	0.0%

4.2.1.3. Effects of Modeling Error

In this section, the effect caused by modeling error on the efficiency of the FRFC method was studied. Firstly, four cases considering modeling error in the system matrices but without measurement noise were investigated: Case M1 considered modeling error in the mass matrix; Case M2 considered modeling error in the damping matrix; Case M3 considered modeling error in the stiffness matrix; Case M4 considered modeling error in all the mass, damping and stiffness matrices. For each case, white noise with 5% noise level was added to the system matrix/matrices and totally 1000 samples were generated. The variation of stiffness of each story was identified using the same procedure with RSC as described in section 4.2.1.2, and the results are listed in Table 4-13. It is observed that the accuracy of the damage detection with 5% modeling error of the damping matrix is quite high. It makes sense since the damping ratio of each mode of this system is only about 2%. Meanwhile, the sensitivity of the accuracy to the

modeling error of the stiffness matrix is higher than the one of the mass matrix. This is because the dynamic stiffness matrix is dominated by the stiffness matrix within lower frequency range. If 5% modeling error were considered in all the system matrices, the standard deviation of damage detection results were about 4% to 8.5%, which were close to the summation of the standard deviations of the results in Case M1 to Case M3. Note that the mean value is non-biased for all Case M1 to Case M4 where only modelling error exists.

Since small modeling error in the mass matrix, damping matrix and stiffness matrix results in moderate error in damage detection, the proposed method seems to be dependent on the well-established or well-updated FE model of the monitored structure. Fortunately, the troublesome model updating of the FE model may be circumvented if the dynamic stiffness matrix, *i.e.* $-\omega^2 M + i\omega D + K$, in Eq. (3-31) can be well-estimated via measured data. The subspace identification technique proposed by (Xiao *et al.* 2001) as described in Section 2.1.3 provides a solution to estimate a dynamic system matrix directly from the input and output data with acceptable accuracy.

To understand the feasibility to perform damage detection with FRFC method using system matrices identified by subspace identification technique, another two numerical case studies were performed. Case M5 assumed the mass matrix was known, and the stiffness and damping matrices were identified using the measured ground and response acceleration with 5% noise level by the subspace identification technique introduced in Section 2.1.3. The stiffness variations calculated by Eq. (3-38) using system matrices identified by Eq. (2-34) and noise-free FRFs are also listed in Table 4-13. The mean value of the identified stiffness variations are all close to the true value, while the standard deviation is almost within 0.5%, which means the error caused by the identified dynamic stiffness matrix is quite small. In Case M6, all the conditions were the same with that in Case M5 except the FRFs was calculated with 5% noise Level-In measurement and the results are listed in Table 4-13. The error between the identified mean value and the true value of the stiffness variation is about 0.5% to 4%, and the relating standard deviation is about 2.5% to 6%. These errors are mainly contributed from the measurement noise when calculating FRFs because the results are quite similar to the results of the 5% noise Level-In Table 4-12 and the error in Case M5 is quite

small.

It should be noted that for a shear building with diagonal mass matrix which is a good assumption in many cases, the mass matrix is not necessary to be known for the FRFC method as derived in Section 3.2.1. The measured FRFs between each story and ground excitation both prior to and after the damage as well as the identified mass-normalized system matrices of the structure in intact state are the only information utilized in FRFC method to calculate the damage reduction ratio of each story. This makes the FRFC method a non-model-based method in this case. The feasibility of this idea is verified here using another numerical case study. In Case M7, all the conditions were the same with that in Case M6 except the mass-normalized stiffness and damping matrices were identified using Eq. (2-35) and the stiffness reduction of each story was calculated using Eq. (3-45). The results of Case M7 are also listed in Table 4-13. The error between the identified mean value and the true value of the stiffness variation is about 0.5% to 4.4%, and the relating standard deviation is about 2.7% to 6.0%. Similar to Case M6, these errors are mainly contributed from the measurement noise because the results are quite similar to the results of the 5% noise Level-In Table 4-12.
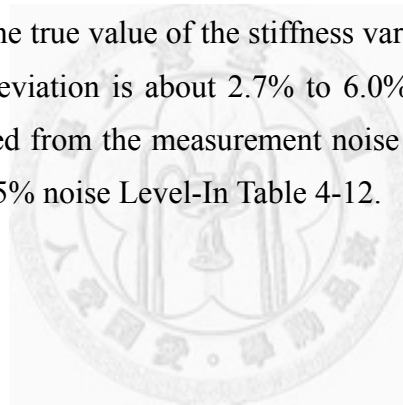
Table 4-13: Mean and standard deviation of the identified stiffness variation of 1000 samples under modeling error (Case M1~ M5) or under both modelling error and measurement noise (Case M6 and M7).

Story Number	Case M1 mean	std	Case M2 mean	std	Case M3 mean	std	Case M4 mean	std	Designated Value
1	50.0%	1.1%	50.0%	0.1%	50.1%	3.6%	50.0%	3.9%	50.0%
2	-0.1%	2.3%	0.0%	0.2%	0.1%	4.4%	0.0%	5.9%	0.0%
3	0.0%	2.7%	0.0%	0.2%	-0.1%	5.3%	-0.3%	7.5%	0.0%
4	0.0%	2.8%	0.0%	0.2%	0.3%	6.6%	-0.2%	8.4%	0.0%
5	-0.2%	2.8%	0.0%	0.2%	0.2%	6.3%	-0.1%	8.1%	0.0%
6	-0.1%	1.8%	0.0%	0.2%	0.1%	5.1%	-0.1%	6.4%	0.0%

Story Number	Case M5 mean	std	Case M6 mean	std	Case M7 mean	std	Designated Value
1	50.0%	0.6%	48.9%	3.7%	48.8%	3.7%	50.0%
2	0.0%	0.5%	2.8%	5.9%	2.8%	6.0%	0.0%
3	0.0%	0.5%	4.2%	4.7%	4.4%	4.5%	0.0%
4	0.0%	0.5%	3.4%	5.1%	3.6%	5.0%	0.0%
5	0.1%	0.6%	3.7%	6.0%	3.8%	6.0%	0.0%
6	0.0%	0.3%	0.5%	2.6%	0.5%	2.7%	0.0%

4.2.2. Experimental Validation

4.2.2.1. Test Structure Description

A 1/4-scale 6-story steel building structure (Figure 4-14) designed by NCREE was used for experimental validation on the proposed FRFC method. As shown in Figure 4-15, the 6-story 1/4-scale structure consisted of a single bay with 1.0m×1.5m floor area with uniformly 1.0 m story height. The size of column and beam was 150mm×25mm (rectangular section) and 50mm×50mm (L-section), respectively. The beam-floor connection was welded, and the floor-beam connection and the floor-column connection were bolted. The dead load was simulated by lead-block units fixed on the steel plate of each floor, and the total mass of each floor of the target structure was 862.85 kg, except the mass of the roof floor was 803.98 kg. The stiffness of the bracing system was controlled by a small connecting plate (named as "B3") whose size was 100mm×10mm with clear height 196mm as shown in Figure 4-16.

Figure 4-14: A 1/4-scale 6-story steel building structure.
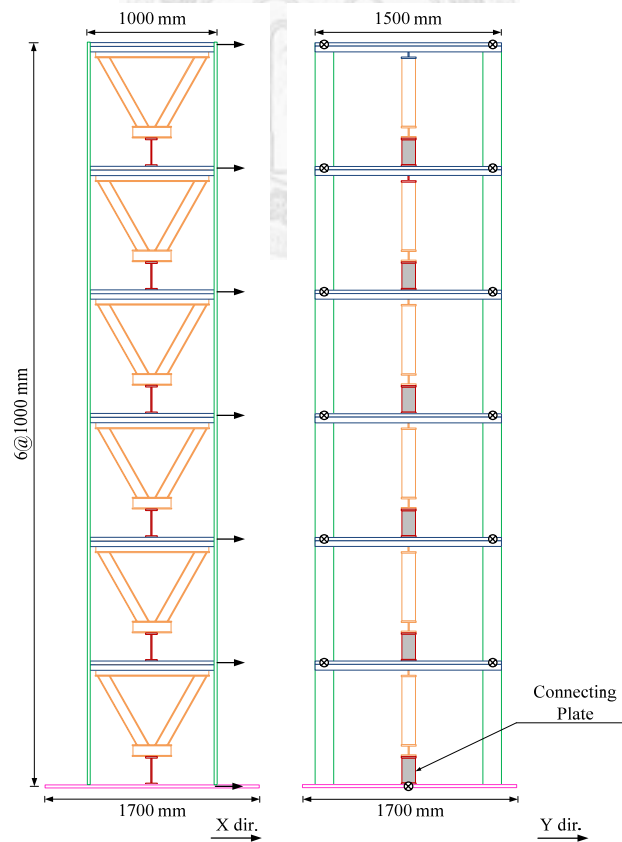
Figure 4-15: Side views of the 1/4-scale 6-story steel building structure.

Figure 4-16: Connecting plates installed in the bracing system of the 1/4-scale 6-story steel building structure (left: B3; middle: B2; right: B1).

4.2.2.2. Damage Cases

To imitate damage of the structure, the original connecting plate of the bracing system was removed or replaced by smaller connecting plates "B2" and "B1" whose cross-section were 100mm×5mm and 100mm×3mm respectively (see Figure 4-16). The connection of these connecting plates was designed as bolted (see Figure 4-17); therefore the bending shape of the plate should be between double-curvature and single-curvature. The story-stiffness reduction ratios assuming double-curvature and single-curvature were calculated. These story-stiffness reduction ratios of different size of bracings or without bracings were summarized in Table 4-14. The mean value of the story-stiffness reduction ratios is chosen as a reference value to check with the experimental results.

Figure 4-17: Close view of the bolting connection of the connecting plates.

Table 4-14: Estimated story-stiffness reduction ratios contributed by removing or replacing connecting plates.

	Single-Curvature	Mean	Double-Curvature
Removed	-54.8%	-37.3%	-19.8%
B1	-38.4%	-26.2%	-13.9%
B2	-27.4%	-18.7%	-9.9%

In order to examine the feasibility of the proposed FRFC method, totally 8 cases were conducted for the 6-story steel building structure as summarized in Table 4-15. Case R1 was the baseline test and no damage was introduced. Case R2 simulated the damage occurring in the first story by replacing the bracing with a smaller bracing "B2". In order to simulate the extension of damage both in extent and in range, the adjacent bracings were replaced by bracings "B2" and "B1" or even removed in Case R3 and Case R4. Case R5 was another baseline test to see if the proposed FRFC method may give false alarm. Case R6 through Case R8 simulated the phenomenon with sparsely distributed damage.

Table 4-15: Cases of experimental study in Section 4.2. ("B3", "B2" and "B1" are types of bracings; "R" represents removing of bracing).

Story Number	Case Nunber							
	R1	R2	R3	R4	R5	R6	R7	R8
6F	B3	B3	B3	B3	B3	B3	B1	B3
5F	B3	B3	B3	B3	B3	B3	B3	B3
4F	B3	B3	B3	B3	B3	R	R	R
3F	B3	B3	B3	B2	B3	B3	B3	B3
2F	B3	B3	B2	B1	B3	B3	B3	B3
1F	B3	B2	B1	R	B3	R	R	B3

4.2.2.3. Excitation and Measurement

All the cases were subjected to uniaxial ground excitations in X-direction including El Centro earthquake and white noise with PGA 0.05 g. The auto-spectra of achieved excitations of Case R1 shaking table test is shown in Figure 4-18. It is observed that the frequency content of the El Centro earthquake excitation in higher frequency is much

less than the one in lower frequency.

The acceleration responses in each story were obtained by averaging the measured acceleration responses in X-direction at both sides. The sampling rate for collecting discrete data was 200 Hz. The data length was 46.08 seconds and 133.12 seconds for the El Centro earthquake and white noise excitation respectively.
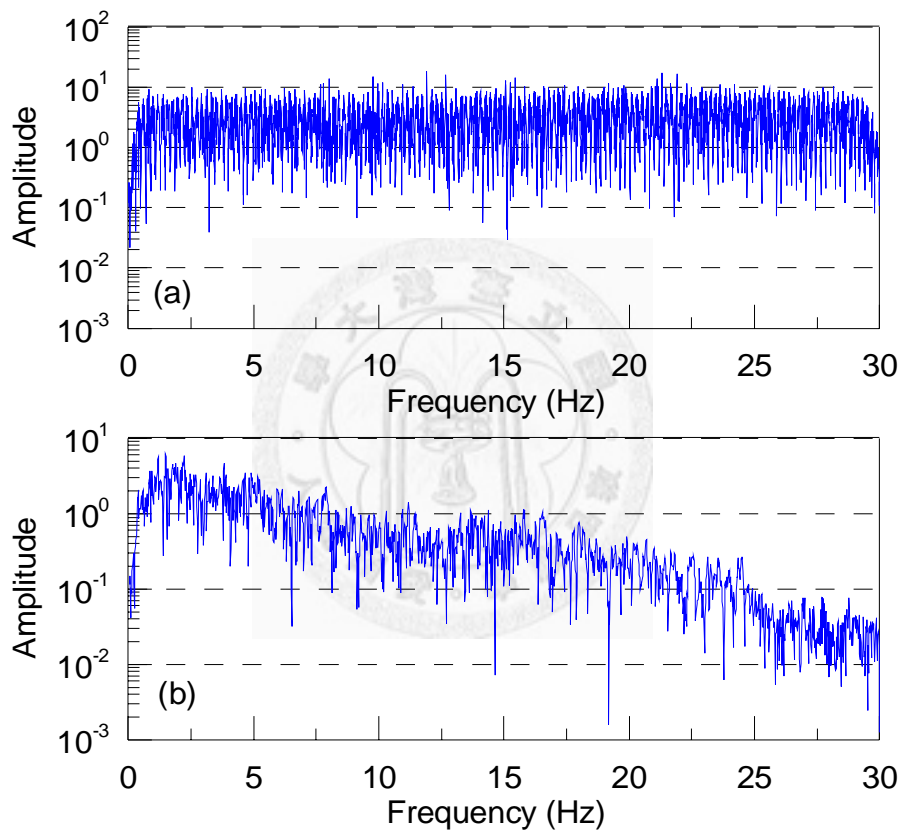
Figure 4-18: Auto-spectrum of the achieved ground excitations in Case R1: (a) white noise; (b) El Centro earthquake.

4.2.2.4. Data Preparing for FRFC Method

The FRFs between each story and the ground floor were calculated by Eq. (3-39) using measured ground and response acceleration time-histories and then divided by square of the circular frequencies. Typical FRFs of both the El Centro earthquake and white noise excitations are shown in Figure 4-19. It is observed that all the first 6 modes of the

structure are distinct under the white noise excitation while only the first 4 modes of the structure can be clearly recognized visually under the El Centro earthquake due to the insufficient frequency content of the El Centro earthquake.

Besides the FRFs of the structures both prior to and posterior to damage, the FRFC method needs a well-estimated system matrix of the structure in intact state. The mass matrix was assumed diagonal with the lumped value of story mass described in Section 4.2.2.1. The stiffness and damping matrices of both the El Centro and white noise excitations in Case R1 were identified using the subspace identification algorithm with the assumed diagonal mass matrix as described in Section 2.1.3.
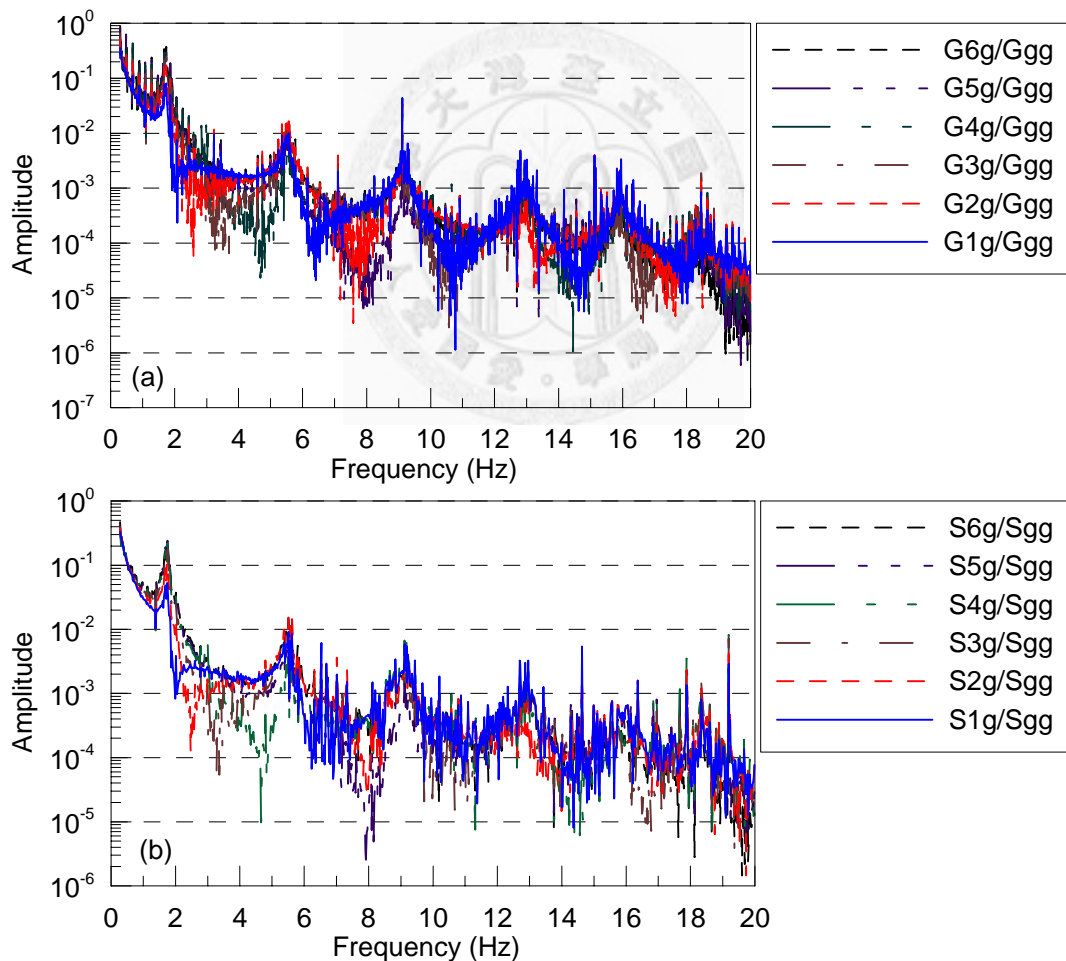
Figure 4-19: Typical FRFs of Case R1 under (a) white noise excitation; (b) El Centro earthquake.

108

4.2.2.5. Damage Detection Results of FRFC Method

The 11 frequencies closest to each identified eigenfrequencies of the structure were selected to detect the variation of stiffness of each story using Eq. (3-38). The 6 damaged eigenfrequencies were determined automatically according to the first 6 modes identified by auto-regression (Marple 1987) of the auto-correlation (Orfanidis 1996) of the measured acceleration response on the 1st story.

For each case, four results were obtained. The first one "WN/WN" represents the results obtained by using damaged FRFs under "white noise excitation" of Case R2 to Case R8 as well as the identified dynamic stiffness matrix and intact FRFs under "white noise excitation" of Case R1. The second one "ELC/WN" represents the results obtained by using damaged FRFs under "El Centro earthquake excitation" of Case R2 to Case R8 as well as the identified dynamic stiffness matrix and intact FRFs under "white noise excitation" of Case R1. The third one "WN/ELC" represents the results obtained by using damaged FRFs under "white noise excitation" of Case R2 to Case R8 as well as the identified dynamic stiffness matrix and intact FRFs under "El Centro earthquake excitation" of Case R1. The fourth one "ELC/ELC" represents the results obtained by using damaged FRFs under "El Centro earthquake excitation" of Case R2 to Case R8 as well as the identified dynamic stiffness matrix and intact FRFs under "El Centro earthquake excitation" of Case R1.

The RSC weighted results of the "WN/WN", "ELC/WN", "WN/ELC", and "ELC/ELC" of Case R2 to Case R8 as well as the reference value of the story-stiffness reduction ratios calculated in section 4.2.2.2 are shown in Figure 4-20. According to the results in Figure 4-20, some conclusions can be made. Firstly, Case R5 is intact hence no stiffness variations should be identified. However, the results of Case R5 indicate some biased errors and about 8% error in maximum of the identified variation of stiffness may be obtained. This may be mainly due to measurement noise effects which may contribute biased errors as illustrated in the numerical study. Case R2 is with single relative small damage in the first story and the results are quite satisfactory because all the four sets of results were consistent with each other and close to the reference value. Similar conclusion may be made according to the results of Case R6 to Case R8 which simulated the sparsely distributed damage. However, although the damage extent of the 1st story was identified quite successfully, the identified damage extent of the 2nd story

in Case R3 was relatively small comparing to the reference value. Similarly, the identified damage extent of the 2nd story and 3rd story in Case R4 were also relatively small comparing to the reference value.
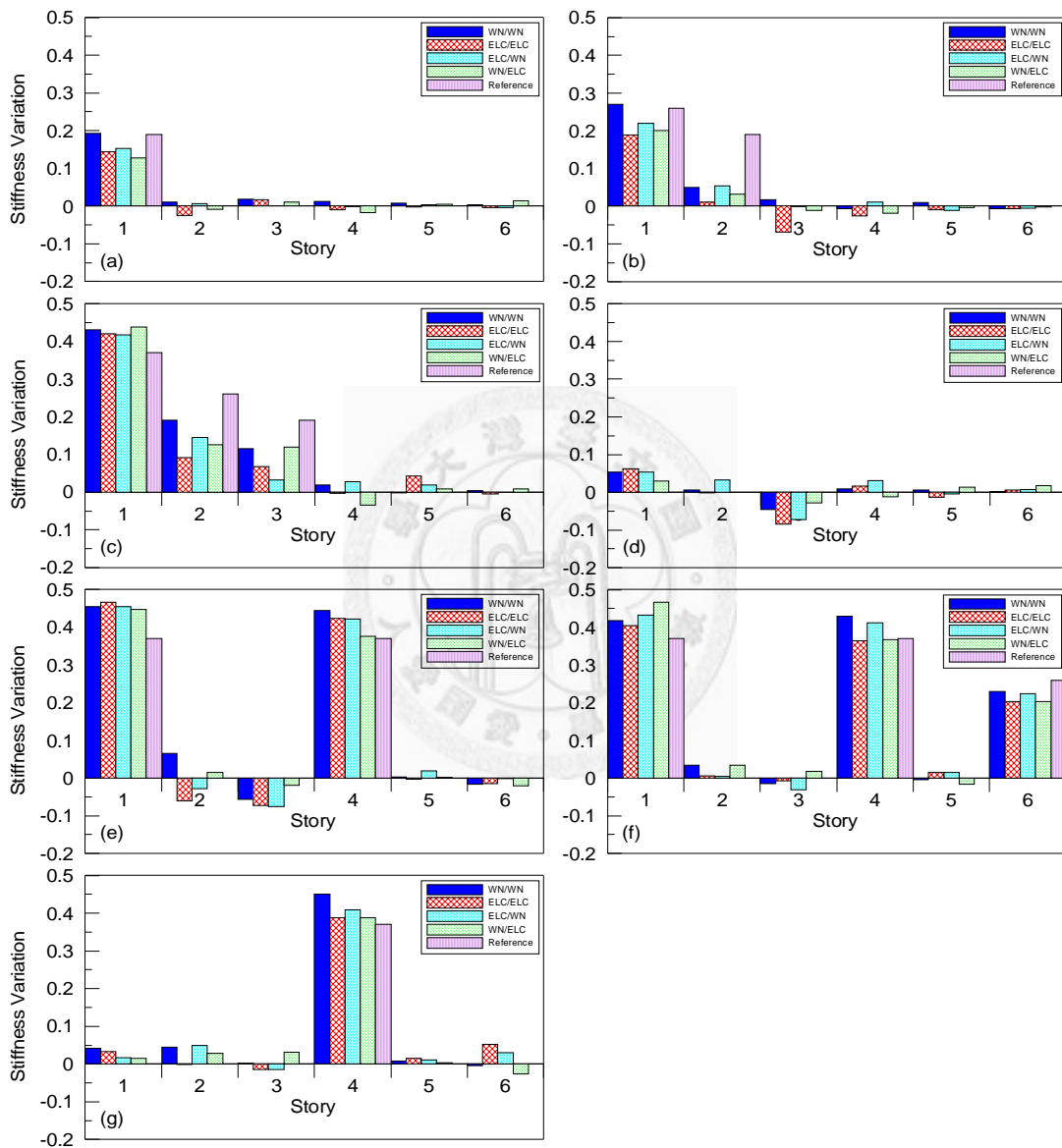
Figure 4-20: Identified story-stiffness reduction ratio from the experimental studies: (a) Case R2; (b) Case R3; (c) Case R4; (d) Case R5; (e) Case R6; (f) Case R7; (g) Case R8.

4.2.3. Experimental Validation of Integration with Wireless sensing systems

The idea proposed in Section 3.2.2 to integrate FRFC method with wireless sensing systems was validated in this Section. The main attraction of this idea is to take advantage of collocated computational power in each wireless sensing unit and save the energy consumption of wireless sensing unit at the same time. Therefore, the purposes of the experimental validation in this section are: (i) to realize the on-line damage detection operation scheme by integrating software and hardware; (ii) to verify the feasibility of the proposed on-line damage detection operation scheme; (iii) to recognize the possible energy saved by the proposed on-line damage detection operation scheme.

4.2.3.1. Wireless Sensing Unit

The prototype of wireless sensing unit developed by Wang *et al.* (2005) was employed here to realize the on-line damage detection operation scheme. This prototype was applied to both structural health monitoring (Lu *et al.* 2008b; Weng *et al.* 2008) and structural control (Lu *et al.* 2008a) successfully. Figure 4-21 shows the overall hardware design of the prototype wireless sensing unit with an optional off-board auxiliary module for conditioning analog sensor signals. The main wireless sensing unit (shown in the top part of the figure) consists of three functional modules: sensor signal digitization, computational core, and wireless communication. The auxiliary sensor signal conditioning module (shown in the bottom part of the figure) assists offsetting analog sensor signals prior to digitization. The key parameters of the prototype wireless sensing unit are summarized in Table 4-16.
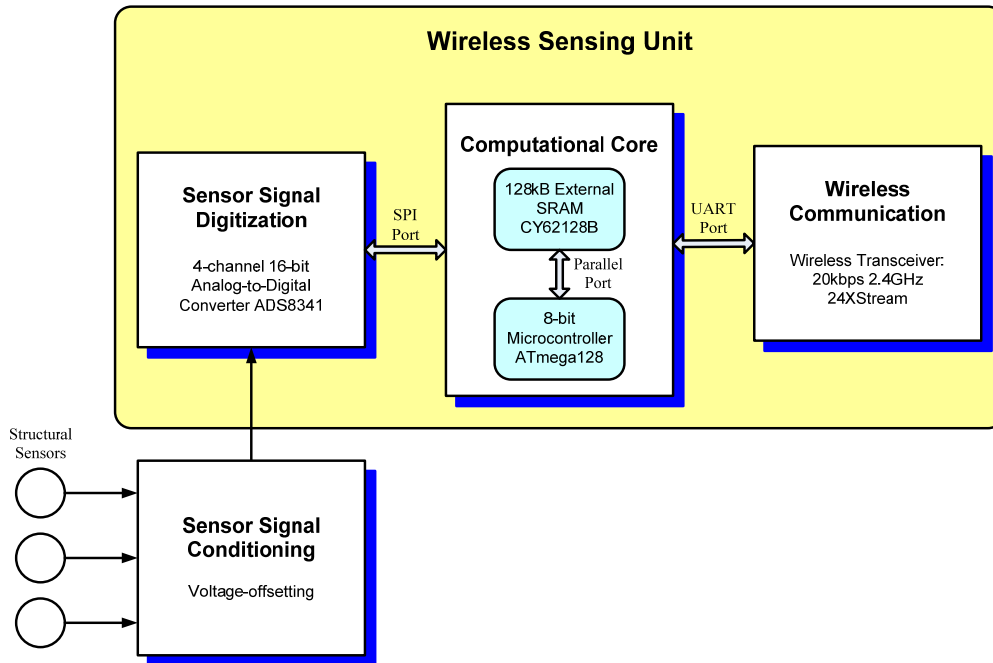
Figure 4-21: Functional diagram detailing the hardware design of the wireless sensing unit. (modified from Wang 2007)
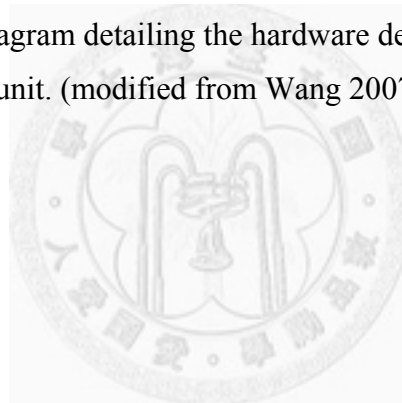
Table 4-16: Key performance parameters of the wireless sensing unit.

(modified from Wang 2007)

Design Parameter	Specification
Computing Core	
Microcontroller	8-bit RISC[1] architecture, up to 16MIPS[2] throughput at 16MHz
Flash Memory	128K bytes
Internal SRAM[3]	4K bytes
External SRAM	128K bytes
EEPROM[4]	4K bytes
Power Consumption	30mA active, 55μA standby
Wireless Transmission	
Operating Frequency	ISM 2.4000 - 2.4835 GHz
Data Transfer Rate	19.2 kbps
Communication Range	Up to 180m indoor, 5km at line-of-sight
Power Consumption	150mA transmitting, 80mA receiving, 26μA standby
Sensing Interface	
Sampling Precision and Rate	16bit, Up to 100kHz
Analog Sensor Channels	4

4.2.3.2. Experimental Setup

The same test structure in Section 4.2.2.1 and measurement setup in Section 4.2.2.3 were employed again here to perform experimental validation of the proposed wireless on-line damage detection operation scheme. For the shaking table wired measurement system, Setra141-A accelerometers with acceleration range of ±4 g and a noise floor of 0.4 mg were employed. Multiple Pacific Instrument Series PI660-6000 data acquisition chassis are used in the wired system.

The wireless sensing unit was instrumented with the "TOKYO SOKUSHIN Servo Velocity Seismometer" type VSE-15A which was placed in each story including the

---

[1] RISC: reduced instruction set computer.
[2] MIPS: million instructions per second.
[3] SRAM: static random access memory.
[4] EEPROM: electrically erasable programmable read-only memory.

ground floor. The wireless sensing systems consists of 7 wireless sensing units and 7 VSE-15A sensors. A typical setup of wireless sensing units and sensor as well as associated power supply devices and antennas are shown in Figure 4-22. The VSE-15A was switched to acceleration mode in order to compare the wireless measured acceleration data to the one measured by the data acquisition system of shaking table system. The analog output voltage of the VSE-15A sensor was -10V~10V, which was offset to 0~5V by the auxiliary sensor signal conditioning module. The specification of both the VSE-15A sensor and the Setra141-A accelerometers employed by the wired system are listed in Table 4-17. The sampling rate of both wired and wireless system was 200 Hz.

Because the FRFC method has been validated by wired data obtained in experimental case studies with 8 different damage cases and 2 different excitations in Section 4.2.2, only 4 different damage cases (see Table 4-18) under El Centro earthquake excitation with PGA 0.05 g were studied in this section. Case W1 was the baseline test and no damage was introduced. Case W2 was another baseline test to see if the FRFC method may give false alarm. Case W3 and Case W4 simulated the damage occurring by removing the "B3" connecting plates in the designated stories.
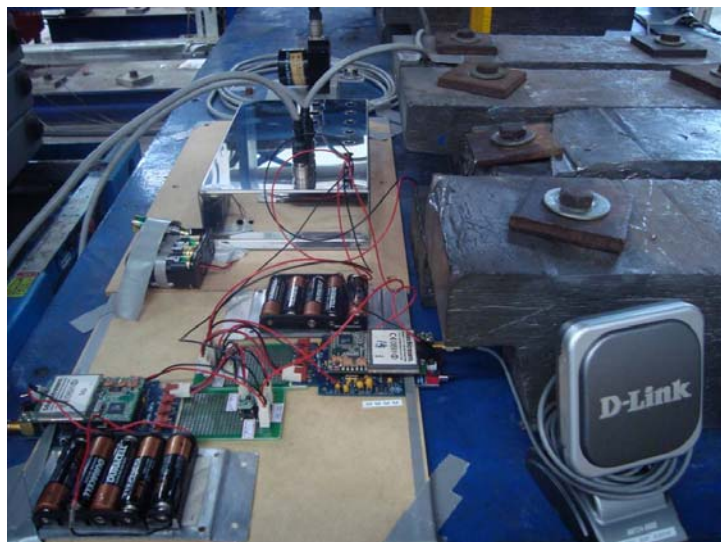
Figure 4-22: Close view of the wireless sensing units, power supply devices, antennas and sensors.

Table 4-17: Specification of the sensors used by the wire-based and wireless systems.

Specification	Setra 141-A	VSE-15A
Maximum Range	±4G	±2G
Sensitivity	0.125V/G	5V/G
Bandwidth	260Hz	0.2 to 70Hz
Resolution	0.4mG	0.1mG

Table 4-18: Cases of experimental study in Section 4.2.3 ("B3" represents the type of connecting plates; "R" represents removing of connecting plates).

Story number	Case Number			
	W1	W2	W3	W4
6	B3	B3	B3	B3
5	B3	B3	B3	B3
4	B3	B3	B3	B3
3	B3	B3	B3	R
2	B3	B3	B3	B3
1	B3	B3	R	R

4.2.3.3. Imbedded Algorithms in the Wireless Sensing Unit

In order to compare the wireless measured data and the FFT results calculated by the wireless sensing units with the wired ones, these data were recorded in the wireless sensing unit and also transmitted wirelessly. Therefore, due to the limited memory of hardware of wireless sensing units described in Section 4.2.3.1, the auto-regression algorithm and auto-correlation algorithm utilized in the experimental validation of FRFC method in Section 4.2.2 were not employed here. Instead, a smoothing algorithm and peak-picking algorithm which require less memory were imbedded in the wireless sensing units.

The operational scheme of Figure 3-2 requires the wireless sensing unit to equip with FFT algorithm, smoothing algorithm and peak-picking algorithm. The Cooley-Tukey FFT algorithm coded by Wang *et al.* (2005) was borrowed here to be embedded in the WSU. The algorithms for smoothing and peak-picking the Fourier spectrum after taking FFT of the measured data are described here. The triangular smoothing with a weighting function was employed as:

$$\hat{Y}_j = \frac{\sum\limits_{i=-n}^{n} Y_{j+i} \times w_i}{\sum\limits_{i=-n}^{n} w_i}$$

(4-6)

where $w_i = n + i + 1$ if $i \leq 0$ and $w_i = i$ if $i > 0$; n denotes the half bandwidth of the weighting function; Y denotes the absolute value of FFT results of the measured data; $\hat{Y}_j$ denotes the absolute value of FFT results after smoothing. The peak of smoothed FFT results $\hat{Y}_j$ was picked if $\hat{Y}_j > \hat{Y}_{j-1}$ and $\hat{Y}_{j+1} > \hat{Y}_j$. For the measured data with length of 4096 points, the half bandwidth of the weighting function n started at 20 and increased by 10 per time if wider bandwidth were required. The bandwidth stopped increasing if 6 peaks or less than 6 peaks were picked. For the 6-story test structure, only the FFT results below 20Hz were smoothed. Note that Y needs to be padded with zeros for the first few freuquencies for the traiangular smoothing algorithm. The smoothed FFT results below 0.2 Hz was eliminated to avoid abnormal value caused by offset of the measured data.

After the peaks of FFT results of each wireless sensing unit transmitted to the host computer, the most probable eigenfrequencies were determined by taking the median of each set of peaks and were broadcasted to each wireless sensing unit afterwards. The adjacent 11 FFT results around the 6 most probable eigenfrequencies were transmitted from wireless sensing unit to host computer to compute the stiffness variation of each story using Eq. (3-38).

4.2.3.4. Quality of the Wireless Sensor Data

The typical time-history of the measured acceleration response of both the wireless system and wired system in Case W2 after zero-mean under El Centro earthquake excitation are shown in Figure 4-23. In general, the wireless-measured data had a good agreement with the wired-measured one. However, take a close look at the data as shown in Figure 4-24; it is evident that the noise ratio in the wireless-measured data is higher than the one in the wired-measured data, especially for the data measured on the ground floor. The extra noise in the wireless measured data may contribute additional

errors to the damage detection results using FRFC method as discussed in numerical studies in Section 4.2.1.2.
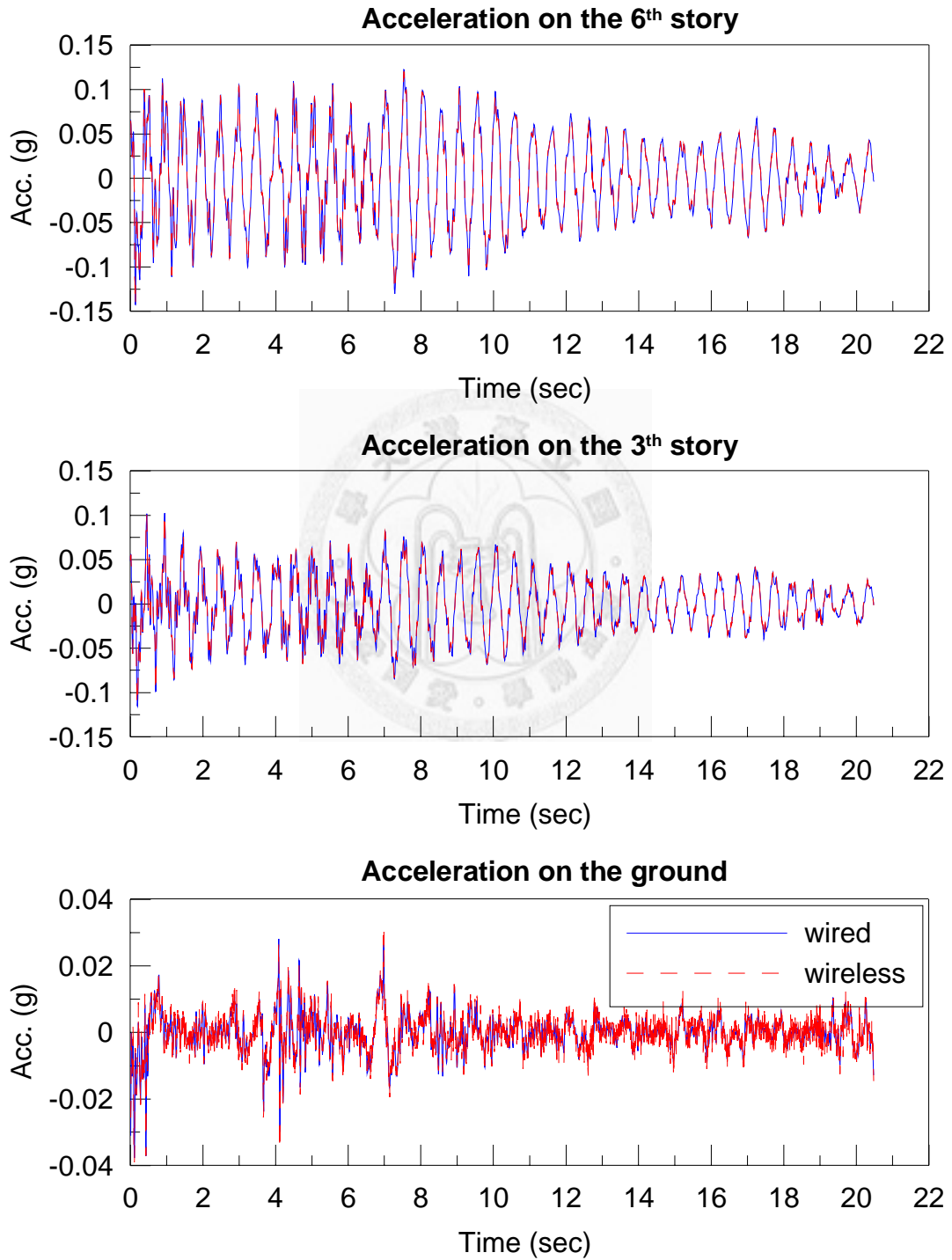
Figure 4-23: Comparison between wireless and wired sensor data – whole time history.
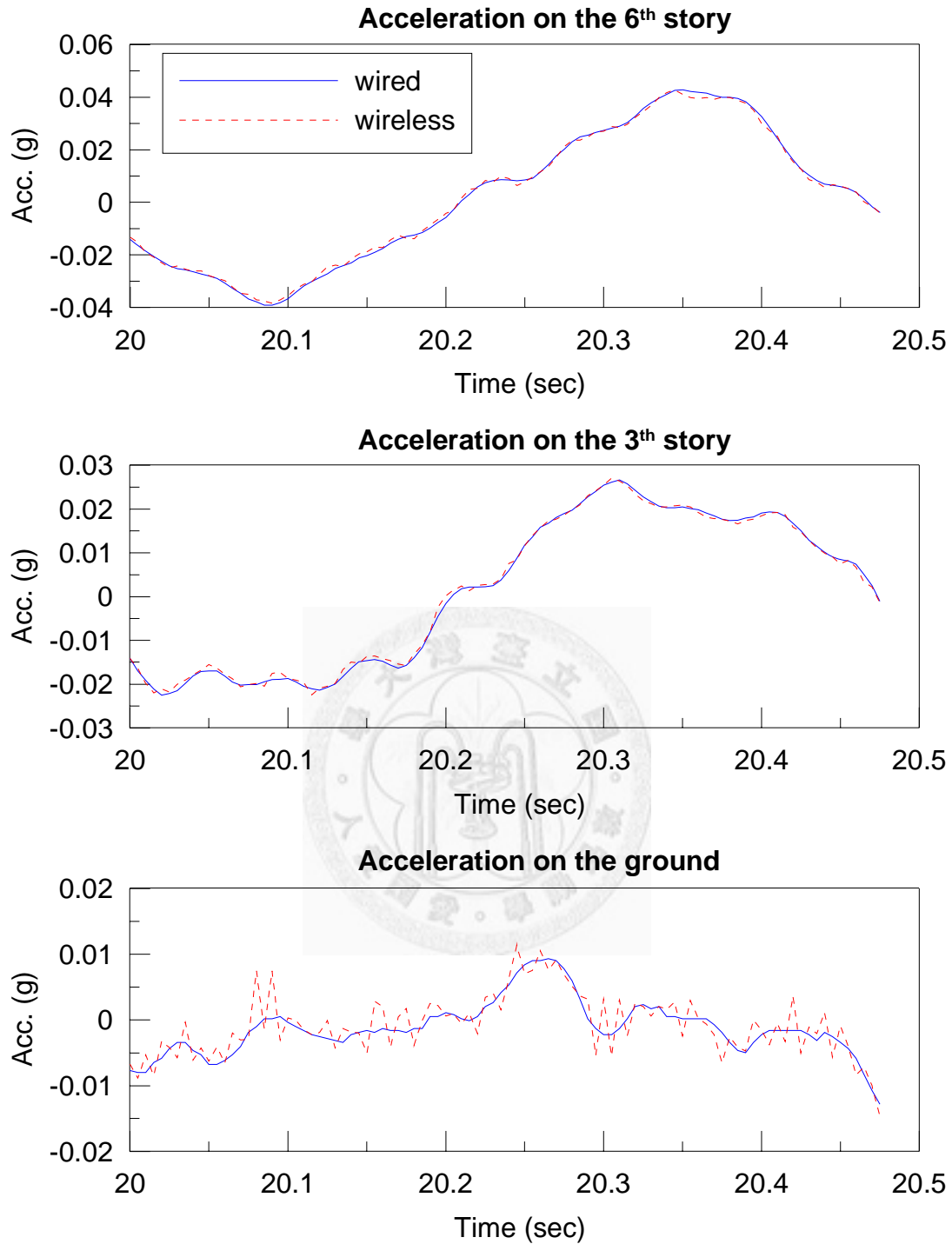
Figure 4-24: Comparison between wireless and wired sensor data – close view.

4.2.3.5. Damage Detection Results of FRFC Method Integrated with WSU

The mass matrix was assumed diagonal with the lumped value of story mass described

in Section 4.2.2.1. The stiffness and damping matrices of the structure in Case W1 were identified using the subspace identification algorithm with the assumed diagonal mass matrix as described in Section 2.1.3. The FRFs of the test structure in Case W1 and also the system matrices of the test structure identified using the data in Case W1 were already written in the host computer. The adjacent 11 FFT results around the 6 most probable eigenfrequencies were utilized to calculate FRFs using Eq. (3-39) right after the host computer received them from wireless sensing units. Therefore, on-line detection of the stiffness reduction ratio of each story was implemented by integrating FRFC method with the wireless sensing systems.

The RSC weighted results of stiffness reduction ratio of each story is plotted in Figure 4-25 with bars marked as "Wireless On-Line". For Case W2 with no damage, no stiffness variations of any story should be identified. For Case W3 and Case W4, stories with connecting plates removed should have stiffness reduction ratio close to the reference value, while other stories should have no stiffness variations. For all the three cases, the damage locations were detected successfully with stiffness reduction ratio about 10% errors. For the bars in Figure 4-25 marked as "Wireless Off-Line", the FRFs of the test structure after damage were obtained using FFT results of the wireless-measured time-history calculated in the host computer, instead of the wireless-calculated FFT results calculated in the wireless sensing units. Little improvement of the results was achieved if FFT results were obtained using the DFT algorithm in the Matlab software. However, if the FRFs of the test structure after damage were obtained using FFT results of the wired-measured time-history in the host computer, the results of damage localization and quantification improved a lot (marked as "Wired Off-Line" in Figure 4-25). Much less error was obtained if wired-measured data were used. The difference between wireless and wired data as shown in Figure 4-25 could mainly contributed by the hardware difference including power supply devices of sensors, type of sensors and data acquisition system, *etc.* Nevertheless, the feasibility of the proposed idea to integrate FRFC method with wireless sensing systems to take advantage of collocated computing resources in wireless sensing units was verified. The energy efficiencies gained from FRFC method integrated with wireless sensing systems are discussed in the next section.
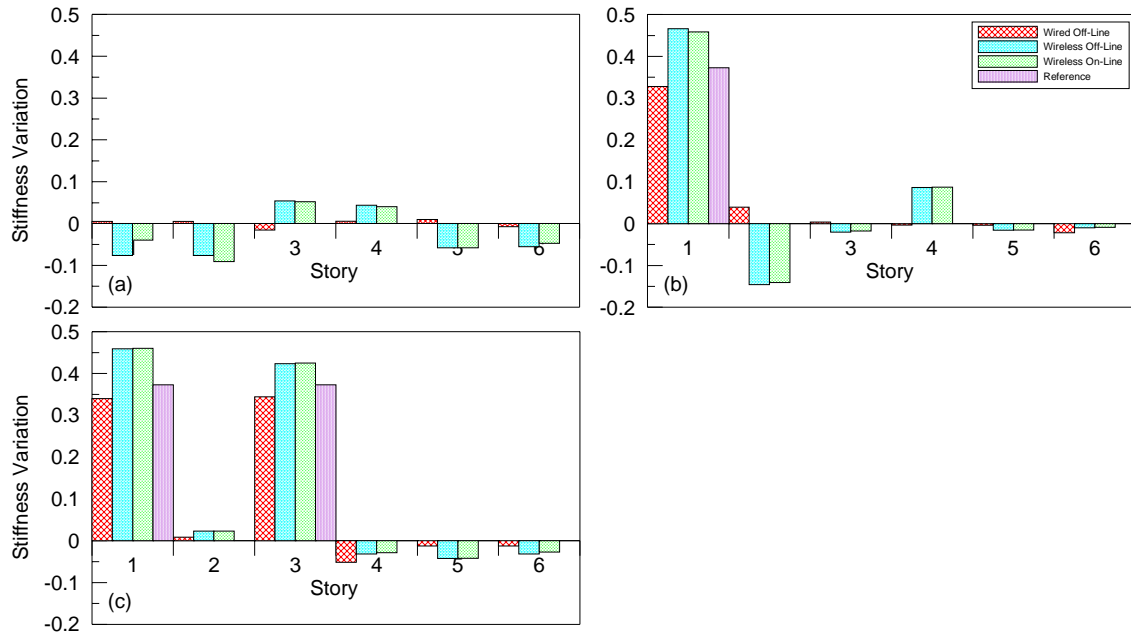
Figure 4-25: Comparison among identified story-stiffness reduction ratio obtained by wireless on-line, wireless off-line and wired off-line. (a) Case W2; (b) Case W3; (c) Case W4.

4.2.3.6. Energy Efficiencies Gained from Integrating FRFC Method with WSS

In this section, the energy consumed by the wireless transmission of raw time-history data E_1 is compared to the total energy E_2 required by FRFC algorithm in WSU (except the energy for recording raw time-history data). If E_2 is less than E_1, then there is an advantage of energy efficiencies contributed by the integration of FRFC method and wireless sensing systems.

Energy consumed by wireless transmission of raw time-history data

The measured time-history and FFT results are stored within the wireless sensing unit memory bank as floating point numbers. With each measurement point requiring 4 byte of memory, a 4096-point time-history record occupies 16,384 bytes of the memory. The 24XStream wireless transceiver is capable of sending data packets with a maximum size of 1462 byte (including 14 byte of overhead per packet). As a results, to wireless transmit these data using the 24XStream wireless transceiver, 12 transmission packets

120

with 16,538 bytes are transmitted wirelessly. The transmission of data takes 6.89 seconds using 24XStream with 19,200 bits/s transfer rate. All the hardware components are internally referenced at 5V. The current consumption of the main components in wireless sensing unit is summarized in Table 4-19 (Wang 2007). The complete current consumption of wireless sensing unit in transmitting mode is 182mA. Therefore, the energy consumed by the wireless transceiver can be determined as follows:

$$E_1 = (5V)(0.182A)(6.89s) = 6.27J \tag{4-7}$$

Table 4-19: Approximate current consumption of the wireless sensing unit.
(modified from Wang 2007)

Component	Active Current
A/D converter ADS8341	1mA
Micro-controller ATmega128 (at 8MHz)	15mA
SRAM CY62128B	15mA
Support electronics	1mA
Wireless transceiver 24XStream	150mA transmitting, 80mA receiving
Complete wireless sensing unit w/o wireless transceiver	32mA
Complete wireless sensing unit w/ wireless transceiver	182mA transmitting, 112mA receiving

Energy consumed by FRFC algorithms in WSU

As shown in Figure 3-2, the operations required by the FRFC method in wireless sensing unit includes: (i) executing FFT, smoothing and peak-picking algorithms to determine 6 peaks of FFT results in the wireless sensing unit; (ii) transmitting of 6 peaks of FFT results from wireless sensing unit to host computer; (iii) receiving of 6 peaks of FFT results determined in host computer; and (iv) transmitting of adjacent 11 FFT results around the 6 peaks from wireless sensing unit to host computer.

The energy consumed by executing FFT, smoothing and peak-picking algorithms to determine the 6 eigenfrequencies, *i.e.* $\bar{\omega}_i$ in Figure 3-2, depends on the time for smoothing and peak-picking. For determining the 6 peaks of FFT results of the test

structure with 4096 points acceleration response, one to five times of both smoothing and peak-picking processes are enough. This means the bandwidth of smoothing is 20 to 60. The time required to calculate FFT is approximately 15 seconds, and the time required to calculate five times of both smoothing and peak-picking is approximately 2 seconds. The complete current consumption of wireless sensing unit without wireless transceiver is 32mA. The energy consumed by the wireless sensing unit for determining the 6 peaks of FFT results can be determined as follows:

$$E_{2c} = (5V)(0.032A)(15s + 2s) = 2.720J \tag{4-8}$$

After the 6 peaks of FFT results are determined, the 6 unsigned integers which represent the array of locations of the 6 peaks are transmitted to the host computer wirelessly. Once the most probable set of the system eigenfrequencies is determined in the host computer, *i.e.* $\bar{\omega}_{system}$ in Figure 3-2, the 6 unsigned short integers which represent the array of locations of $\bar{\omega}_{system}$ are broadcasted to the wireless sensing units. With each unsigned short integer requiring 2 bytes of memory, the array contains 6 locations of FFT peaks occupies 12 bytes memory. The transmission or receiving of data takes 0.0108 seconds using 24XStream with 19,200 bits/s transfer rate. Following similar calculation algorithm, the energy consumed by the wireless sensing unit for transmitting 6 unsigned integers can be determined as follows:

$$E_{2t1} = (5V)(0.182A)(0.0108s) = 0.010J \tag{4-9}$$

And the energy consumed by the wireless sensing unit for receiving 6 unsigned integers (with complete current consumption of wireless sensing unit in receiving mode 112mA) can be determined as follows:

$$E_{2r} = (5V)(0.112A)(0.0108s) = 0.006J \tag{4-10}$$

Once the location of $\bar{\omega}_{system}$ is received by the wireless sensing unit, the adjacent 11 FFT results around the 6 peaks are transmitted to the host computer. Both the real part and imaginary part of the FFT results are stored within the wireless sensing unit memory bank as floating point numbers. With each FFT results point requiring 8 byte of

memory (both real part and imaginary part), a 66-point FFT results occupies 528 bytes memory. To wirelessly transmit these data using the 24XStream wireless transceiver, only one transmission packet with 542 bytes are transmitted wirelessly. The transmission of data takes 0.23 seconds using 24XStream with 19,200 bits/s transfer rate. Similarly, the energy consumed by the wireless transceiver for transmitting the FFT segments can be determined as follows:

$$E_{2t2} = (5V)(0.182A)(0.23s) = 0.206J \qquad (4\text{-}11)$$

As a result, the total energy E_2 required by the FRFC algorithm in WSU is summarized as follows:

$$E_2 = E_{2c} + E_{2t1} + E_{2r} + E_{2t2} = 2.720J + 0.010J + 0.006J + 0.206J = 2.941J \qquad (4\text{-}12)$$

which is about 47% of 6.271J. This means that the energy consumed by the wireless sensing unit to perform necessary actions for the FRFC method is less than half of the energy consumed by the wireless sensing unit in transmitting the raw time-history to a host computer without performing any local data interrogation. This illustrates the advantage of energy efficiencies associated with FRFC methods integrated with wireless sensing systems.

4.3. Local Flexibility Method

The local flexibility method has been applied to numerical cases of damaged isostatic and hyperstatic beams, and experiments involving a reinforced concrete free-free beam in the laboratory and a real three-span prestressed concrete bridge (Reynders and De Roeck 2008; Reynders and De Roeck 2010). The results show that the estimated local stiffness change is generally accurate. Accurate estimation of the damage of a simple-supported beam can be obtained by measuring only one or a few of the lowest modes. More modes are needed to obtain accurate damage detection results if the structure and damage is more complex. However, these numerical and experimental verifications focus on the beam structures and bridge structures. In this section, the feasibility of the local flexibility method to detect damage in building structures are discussed, both numerically and experimentally.

4.3.1. Numerical Validation

4.3.1.1. A 6-story shear building

The first numerical model is the same model of the one in section 4.2.1.1. The stiffness of each story is 955,720 N/m. The mass of each floor is 439.8 kg. The damping matrix is decided Rayleigh damping on the assumption that the damping ratios of the first two modes are 2%. The six eigenfrequencies are 1.79 Hz, 5.26 Hz, 8.43 Hz, 11.11 Hz, 13.14 Hz, and 14.41 Hz. The damage is assumed to be occurred at the first story with 50% loss of stiffness.

The exact eigenfrequencies, damping ratios and mode shapes were used in Eq. (2-46) and Eq. (2-49) to obtain the quasi-static flexibility matrix. Since the building was isostatic, the load configuration of Figure (4-26) is used as both the load system g^1 and load system g^2. The visual displacement vectors of the structure in intact and damaged states under load system g^1 were calculated using Eq. (3-53). Figure (4-27) shows the estimated relative change of bending stiffness $1 - \dfrac{EI + \Delta EI}{EI} = \dfrac{-\Delta EI}{EI}$ calculated by using Eq. (3-52). Note that "plus" value of the estimated relative change of stiffness relates to "decrease" of stiffness. The results using the first load

configuration (count from left side) in Figure (4-26) relates only to the stiffness of the first story because only the stress field between node 1 and node 2 is not zero, while the results using the second load configuration in the same figure relates to the stiffness of both the first and second stories because the stress field between node 1 and node 3 is not zero, and so on. As a result, the exact value of estimated relative change of stiffness using the first and second load configuration should be 0.5 and 0.333, respectively. As can be observed from the results obtained using 6 modes in Figure (4-27), the estimated relative change of stiffness using 6 modes is almost identical to the exact value.

In order to have an idea about how many modes are necessary for applying local flexibility method on this shear building, the estimated relative change of stiffness using different number of modes are also shown in Figure (4-27). The damage localization seems hold quite successful because the estimated ratio of node 2 remains indicating loss of stiffness even if only one mode was used. The quality of damage quantification decreases a lot when fewer numbers of modes were used. The estimated relative change of stiffness has large error if only the first 3 modes or fewer modes are used.
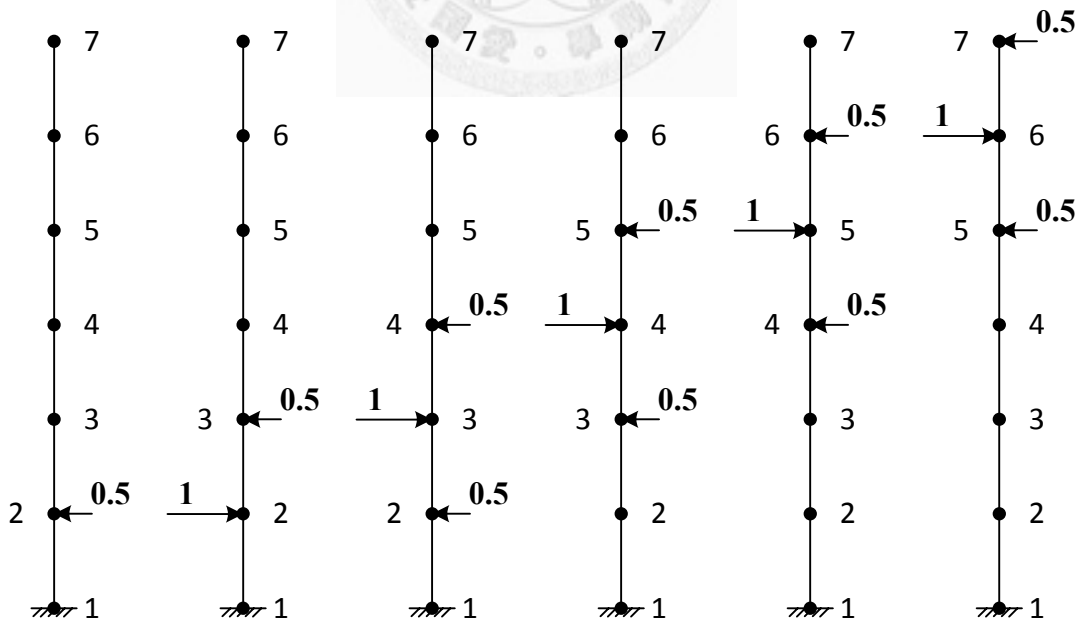
Figure 4-26: Load configurations for the 6-story shear building.
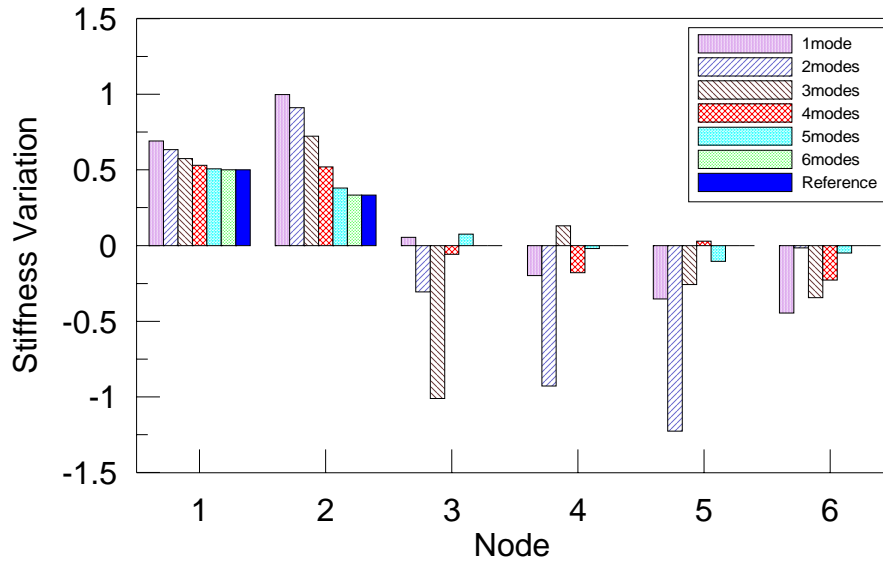
Figure 4-27: Estimated relative change of stiffness of the 6-story shear building using different numbers of modes.

4.3.1.2. A 50-story flexible building

In order to test the feasibility of the local flexibility method for a high-rise flexible building, a numerical model of a 2-span 50-story reinforced concrete 2D frame building structure was constructed as shown in Figure (4-28). In total there were 153 joints, 250 elements and 450 DOFs. The length of each span was 12.5 m and the height of each story as 4 m. The dimension of the column was 1.2m×1.2m; the dimension of girder was 1.8m×1m. The elastic modulus of concrete was $2.3×10^{10}$ M/m^2 with Poisson's ratio equals to 0.3. The lumped mass with 67,824 kg was considered at each joint. The fundamental eigenfrequency of the building was 0.165Hz. The damage was simulated by reducing half of the elastic modulus of elements within the region surrounded by points 4, 8, 100 and 106 (thick lines in Figure 4-28).

Because the number of DOF of the building was large, the original model is simplified to a reduced model using Eq. (2-61) based on the static reduction algorithm. Only the X-translation and Y-rotation DOFs of each joint of the left column were remained in the reduced model; therefore the reduced model had 100 DOFs. The analytical eigenfrequencies and mode shapes were obtained by eigenvalue analysis of the reduced model. Assume only the translation DOFs of every 5 stories were measured, which means only 11 joints were considered in the identification model (ID Model). As a result,

each element between two joints of the ID model represented the contribution of the corresponding 5 stories in the reduced model. This is a practical situation where only some floors of a tall building are equipped with measurement sensors.

To perform damage localization and quantification of the ID model, the analytical eigenfrequencies and partial mode shapes (with 10 measured DOFs) of the reduced model were used in Eq. (2-46) and Eq. (2-49). Since the building was isostatic and quite similar to the 6-story shear building, the load configuration with the same concept in figure (4-26) was used as both the load system g^1 and load system g^2. Figure (4-29) shows the estimated relative change of stiffness $1 - \dfrac{EI + \Delta EI}{EI}$. As can be observed in the results in the same figure, the ratio at node number 1, 2 and 3 estimated using 100 modes equals to 14.6%, 18.6% and 9.5% respectively and the ratio at other joints are all equals to 0%. These results were treated as the best solution for comparing the results obtained using fewer modes.

Again, in order to have an idea about how many modes are necessary for applying local flexibility method on this tall building, the estimated relative change of stiffness using different number of modes are also shown in Figure (4-29). The damage localization seems hold quite successful because the estimated ratio of node 1, 2 and 3 remains indicating loss of stiffness for all the cases, except the case only the first mode was used. The quality of damage quantification also decreases when fewer modes were used. However, it seems that the results obtained using only the first 5 modes are already close to the best solution (remember the reduced model has 100 modes); use more modes can only improve the results a little. This illustrates the benefit of using the flexibility-based method for damage detection. Contrary to the stiffness matrix, the value of the components in the flexibility matrix is mainly controlled by the lower modes as can be observed in Eq. (2-41). The contribution of the modes to the flexibility matrix decreases with ω^{-2}. Moreover, in general, unlike the higher modes which are not easy to identify and always contain more noise, the lower modes are more accurate and reliable.
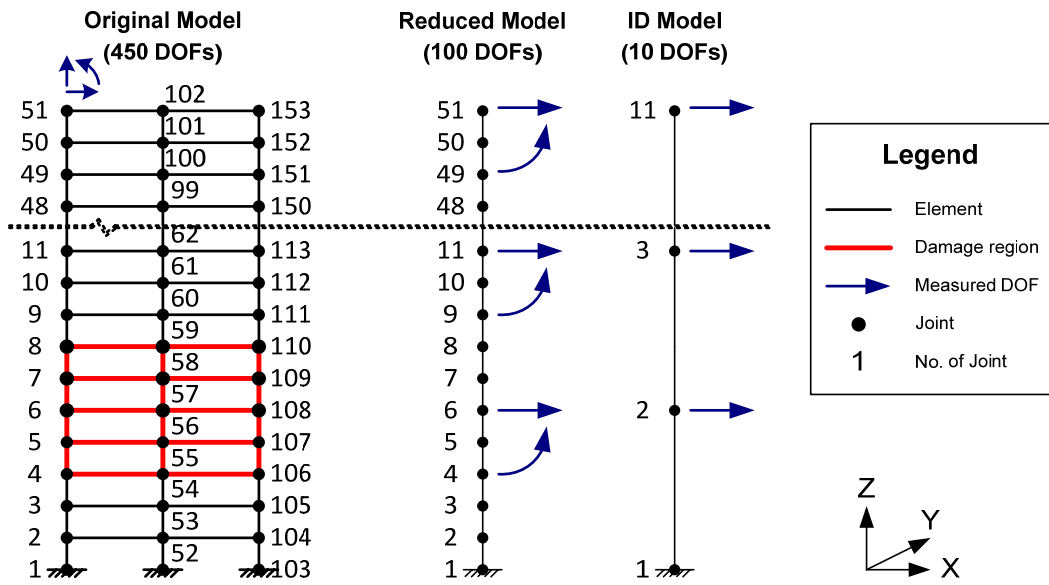
Figure 4-28: A 2-span 50-story reinforced concrete 2D flexible building.
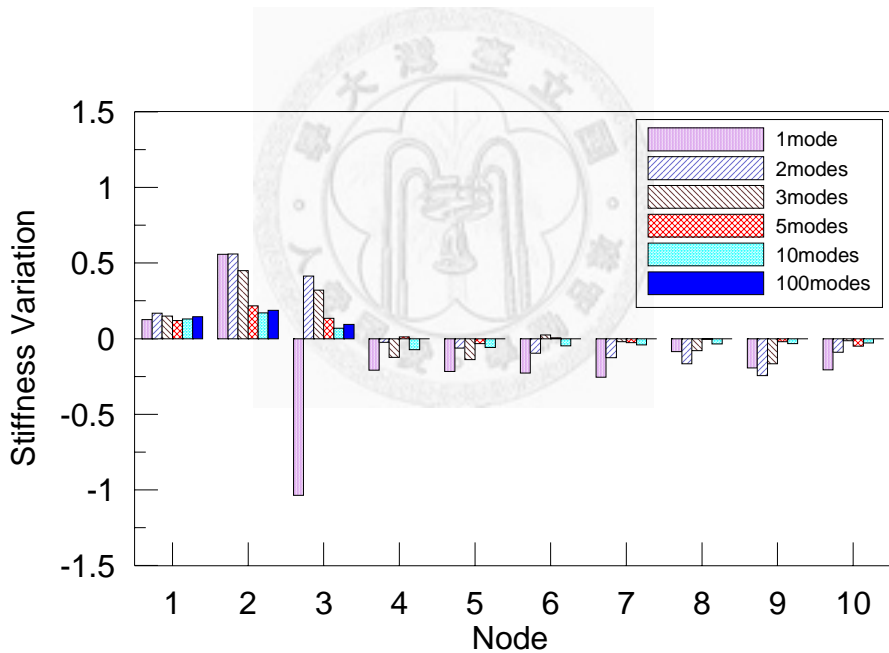
Figure 4-29: Estimated relative change of stiffness of the 2-span 50-story 2D frame
building structure using different numbers of modes.

4.3.2. Experimental Validation

The applicability of local flexibility method was further investigated by experimental studies. The same 6-story steel building structure in section 4.2.2.1 was used again here. The same virtual load configuration used in the 6 story shear building structure in

section 4.3.1.1 as shown in Figure (4-26) was used here. Again, Case R1 was the baseline test and no damage was introduced. Case R2 through R4 simulated the damage occurring in the lower stories. Case R5 was another baseline test to see if the local flexibility method may give false alarm. Case R6 through Case R8 simulated the phenomenon with sparsely distributed damage.

The modal parameters were identified using the SSI technique in Section 2.1.1. Table 4-20 lists the identified modal properties of the 6-story steel building structure in different cases under El Centro earthquake excitation. The quality of all the identified modes was quite good because their MPD values were all less than 6°. Note that these mode shapes identified using the SSI technique in Section 2.1.1 were complex-value. These complex-value mode shapes can be transformed to real-value mode shapes with only amplitude and sign according to the phase between each component and their mean phase. Both the complex-value mode shapes and real-value mode shapes can be used to construct the flexibility matrix.

The mode shape can be mass-normalized using an analytical mass matrix. Alternatively, the mode shapes can be normalized to make the maximum absolute amplitude equal one, *i.e.* non-mass-normalized mode shapes.

The flexibility matrix can be constructed by Eq. (2-41) using mass-normalized real mode shapes. Alternatively, it can also be constructed by Eq. (2-46) and Eq. (2-49) using non-mass-normalized complex mode shapes with the assumption of a distributed diagonal mass matrix.

With the flexibility matrix constructed using the identified modal parameters of the structure both in intact and damaged states, damage detection of the story stiffness variation can be performed using Eq. (3-52).

Table 4-20: Identified modal properties of the 6-story steel building structure in different cases under El Centro earthquake excitation.

Mode	R1			R2			R3			R4		
	f_i (Hz)	ξ_i (%)	MPD (°)	f_i (Hz)	ξ_i (%)	MPD (°)	f_i (Hz)	ξ_i (%)	MPD (°)	f_i (Hz)	ξ_i (%)	MPD (°)
1	1.74	1.4	0.9	1.67	4.1	1.6	1.62	1.7	0.2	1.45	0.9	0.4
2	5.41	1.8	0.9	5.29	1.1	0.4	5.18	0.8	1.5	4.94	0.6	1.7
3	9.10	1.7	1.0	8.91	0.9	1.2	8.80	1.2	1.2	8.40	1.0	0.6
4	12.84	0.8	3.2	12.80	0.7	1.6	12.68	1.0	1.9	12.09	1.4	1.1
5	15.73	0.5	3.3	15.75	0.4	1.5	15.68	0.5	2.2	15.12	0.9	1.6
6	18.26	0.5	0.9	18.24	0.5	2.0	18.19	0.7	5.4	18.07	0.6	1.5

Mode	R5			R6			R7			R8		
	f_i (Hz)	ξ_i (%)	MPD (°)	f_i (Hz)	ξ_i (%)	MPD (°)	f_i (Hz)	ξ_i (%)	MPD (°)	f_i (Hz)	ξ_i (%)	MPD (°)
1	1.75	1.3	0.7	1.46	0.3	0.7	1.45	1.6	0.2	1.56	1.5	0.2
2	5.33	1.2	1.4	4.41	0.4	3.2	4.35	0.6	2.0	4.91	0.8	0.5
3	9.19	1.7	1.5	8.70	0.7	1.3	7.88	0.8	0.8	8.90	0.9	1.0
4	12.82	1.3	1.3	11.26	0.7	0.9	10.85	0.8	1.3	11.58	0.9	1.1
5	15.95	0.8	1.1	15.94	0.5	3.5	15.18	0.6	1.5	15.63	0.4	2.8
6	18.41	0.6	1.5	17.18	0.5	0.9	16.97	0.5	1.2	17.12	0.4	0.5

Using flexibility matrix calculated by Eq. (2-41) with mass-normalized real-value mode shapes

At first, the flexibility matrix was calculated by Eq. (2-41) using 6 real-value mass-normalized modes. The estimated stiffness variation, $1 - \dfrac{EI + \Delta EI}{EI}$, obtained via Eq. (3-52) using the estimated flexibility matrix and all the 6 modes is shown in Figure (4-30). In general, most of the locations and quantity of damage were detected successfully, despite some confusing errors. For example, Case R5 is intact hence no stiffness variations should be identified. However, the results of Case R5 indicate that about 20% errors in maximum of the identified variation of stiffness may be obtained. Comparing these results to the ones obtained by the FRFC method as described in Section 4.2.2, it is observed that the accuracy obtained by LFM is even less than the one obtained by the FRFC method.

If only the first 5 modes were used to construct the flexibility matrix, most of the estimated stiffness variation is still reasonable for both damage localization and quantification, as shown in Figure (4-31), despite the phenomenon of confusing "increasing" of stiffness of the undamaged stories became more serious. At least the

first 4 modes were needed to catch the trend of the true stiffness variation. Using flexibility matrix constructed by less than 3 modes derived worse results of damage localization and quantification. Note that the excitation input of all the cases was El Centro earthquake. Using the mode shapes identified under white noise excitation only changed the results little. Nevertheless, acceptable results were obtained using the flexibility matrix calculated by Eq. (2-41) with 6 modes normalized by the analytical mass matrix.

Using flexibility matrix calculated by Eq. (2-46) with mass-normalized complex-value mode shapes

If the flexibility matrix was calculated by Eq. (2-46) and Eq. (2-49) using mass-normalized complex-value modes, the stiffness variations were acceptable only if all the 6 modes were used (see Figure 4-32). The estimated stiffness variation calculated by Eq. (2-46) and Eq. (2-49) with the fist 5 modes cannot detect the location and extent of the damage with acceptable accuracy (see Figure 4-33). The results using fewer modes were even worse. The flexibility matrix constructed by Eq. (2-46) and Eq. (2-49) using all the 6 modes suffer much less errors than the one constructed by the same equations using fewer modes. This implies that the flexibility matrix calculated by Eq. (2-46) and Eq. (2-49) is more sensitive to the noise in the identified mode shapes than the one calculated by Eq. (2-41). Observing Eq. (2-49), it is found that the there is a term calculated by inversing the matrix constructed by mode shapes and eigenvalue, *i.e.* $(\varLambda_c^H \varPhi^H \varPhi \varLambda_c + \varPhi^H \varPhi)^{-1}$. The inverse of this matrix could induce large errors due to the ill-posed problem especially when noise exists.

Using flexibility matrix calculated by Eq. (2-46) with mass-normalized real-value mode shapes

The stiffness variations obtained by using the flexibility matrix calculated by Eq. (2-46) and Eq. (2-49) using the first 6 or 5 mass-normalized real-value modes is shown in Figure (4-34) and Figure (4-35), respectively. Comparing these two figures to Figure (4-32) and Figure (4-33), it is evident that the quality of damage localization and

quantification improves a lot. While the results using all 6 modes remain almost the same acceptable results, the results using the first 5 modes became much more reasonable. It is concluded that using real-value mode shapes to construct flexibility matrix using Eq. (2-46) and Eq. (2-49) reduces the numerical problem caused by inversing matrix in Eq. (2-49). Comparing Figures (4-34) and (4-35) to Figures (4-30) and (4-31), the quality of damage localization and quantification is quite similar to the one obtained by the flexibility matrix constructed by Eq. (2-41) with mass-normalized real-value mode shapes.

Using "relative" flexibility matrix calculated by Eq. (2-41) with non-mass-normalized real-value mode shapes

Although theoretically the mode shapes used for Eq. (2-41) to construct the flexibility matrix should be mass-normalized, the flexibility matrix with "relative" value still can be obtained if the mass is distributed. These "relative" flexibility matrices of the structure in intact and damaged states can also be used in the local flexibility method. The stiffness variations obtained by using the "relative" flexibility matrix calculated by Eq. (2-41) using the first 6 and 5 non-mass-normalized real-value modes is shown in Figure (4-36) and (4-37), respectively. Comparing Figures (4-36) and (4-37) to Figures (4-30) and (4-31), the quality of damage localization and quantification is almost identical to the one obtained by the flexibility matrix constructed by Eq. (2-41) with mass-normalized real-value mode shapes.

One of the advantage of using Eq. (2-46) and Eq. (2-49) to construct flexibility matrix is to circumvent the construction of an analytical mass matrix, therefore a FE model is not necessary to be constructed for a structure with a distributed diagonal mass matrix; this makes the local flexibility method a non-model-based one. However, as discussed previously, using Eq. (2-49) to construct flexibility matrix could have an numerical problem when inversing a matrix. Fortunately, the concept of using "relative" flexibility matrix in Eq. (3-52) to detect damage is validated for this 6-story steel building structure. This also makes the local flexibility method a non-model-based damage detection method because the "relative" flexibility matrix can be constructed by Eq. (2-41) using non-mass-normalized mode shapes without constructing a FE model. It

should be noted that the mass of each story of this building is almost identical, except the mass on the roof is a little smaller. For a structure with irregular mass distribution, mass-normalized mode shapes are probable still necessary.

In the original paper (Reynders and De Roeck 2010), only the first mode is enough to have a good estimation for damage localization and quantification of a simple-supported beam with one damage location. For a hyperstatic beam with more complex damage, more modes are necessary to have good damage assessment results. It is concluded in the original paper that the results of damage detection depend on factors like the location and extent of the damage. It is the author's opinion that the results of damage detection not only depend on complexity of damage but also on the accuracy of the flexibility matrix constructed by the identified modal parameters. The contribution of a mode to the flexibility matrix is approximately the reciprocal of the square of its circular frequency. For a simple-supported beam, only the first mode can approximate the flexibility matrix with enough accuracy for damage detection using the local flexibility method. For other structures, more modes are necessary to have enough accuracy of flexibility matrix. In the case of this 6-story steel building, the contribution of the lower modes is still big until the 4th mode whose contribution is approximately 1.8% of the contribution of the 1st mode. Therefore, at least the first 4 modes are required to have enough accuracy of the flexibility matrix.

Figure 4-30: Estimated relative change of stiffness of 6-story steel building structure obtained by **Eq. (2-41)** using the first 6 mass-normalized real-value mode shapes from the experimental studies: (a) Case R2; (b) Case R3; (c) Case R4; (d) Case R5; (e) Case R6; (f) Case R7; (g) Case R8.
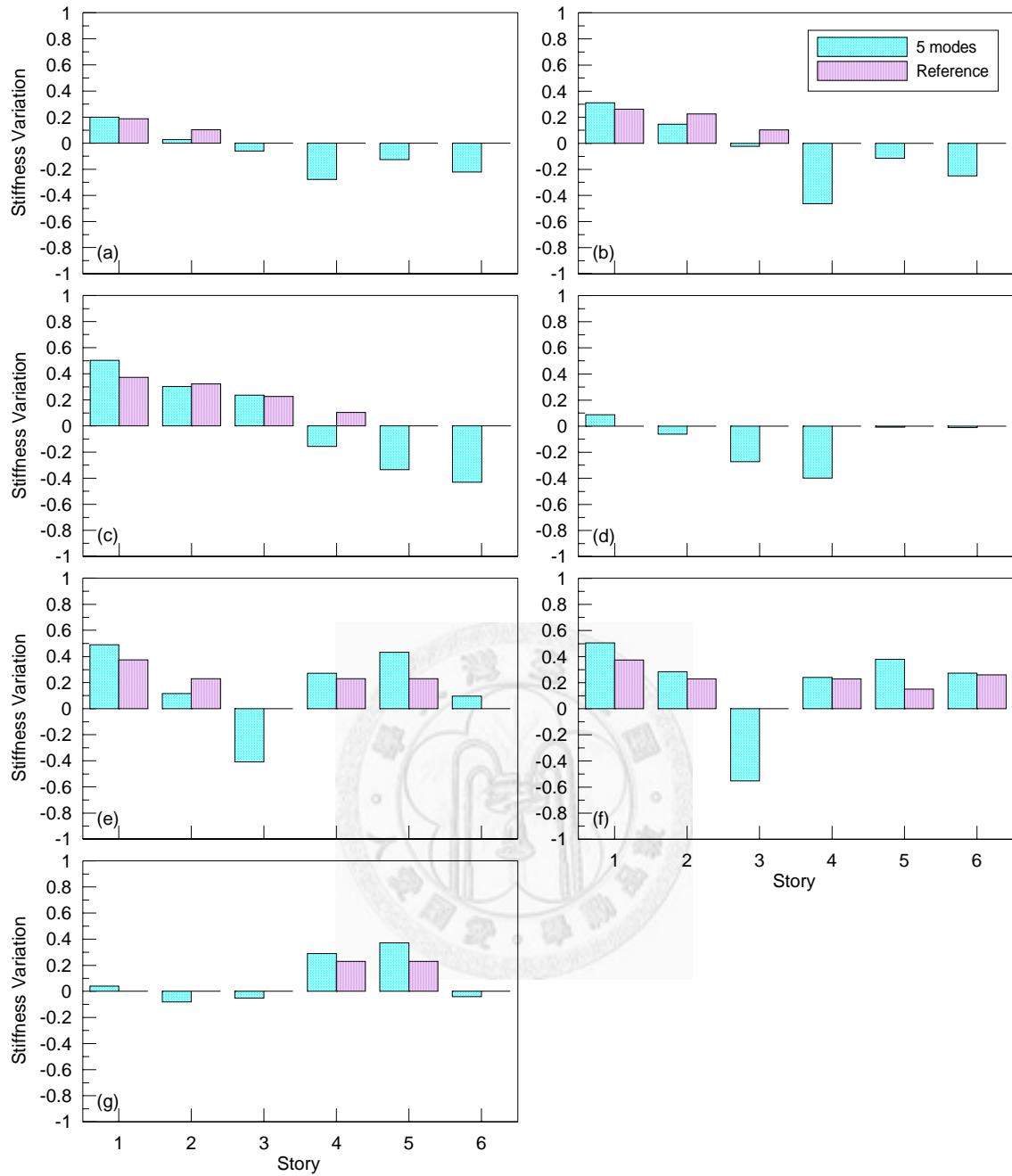
Figure 4-31: Estimated relative change of stiffness of 6-story steel building structure obtained by **Eq. (2-41)** using the first 5 mass-normalized real-value mode shapes from the experimental studies: (a) Case R2; (b) Case R3; (c) Case R4; (d) Case R5; (e) Case R6; (f) Case R7; (g) Case R8.
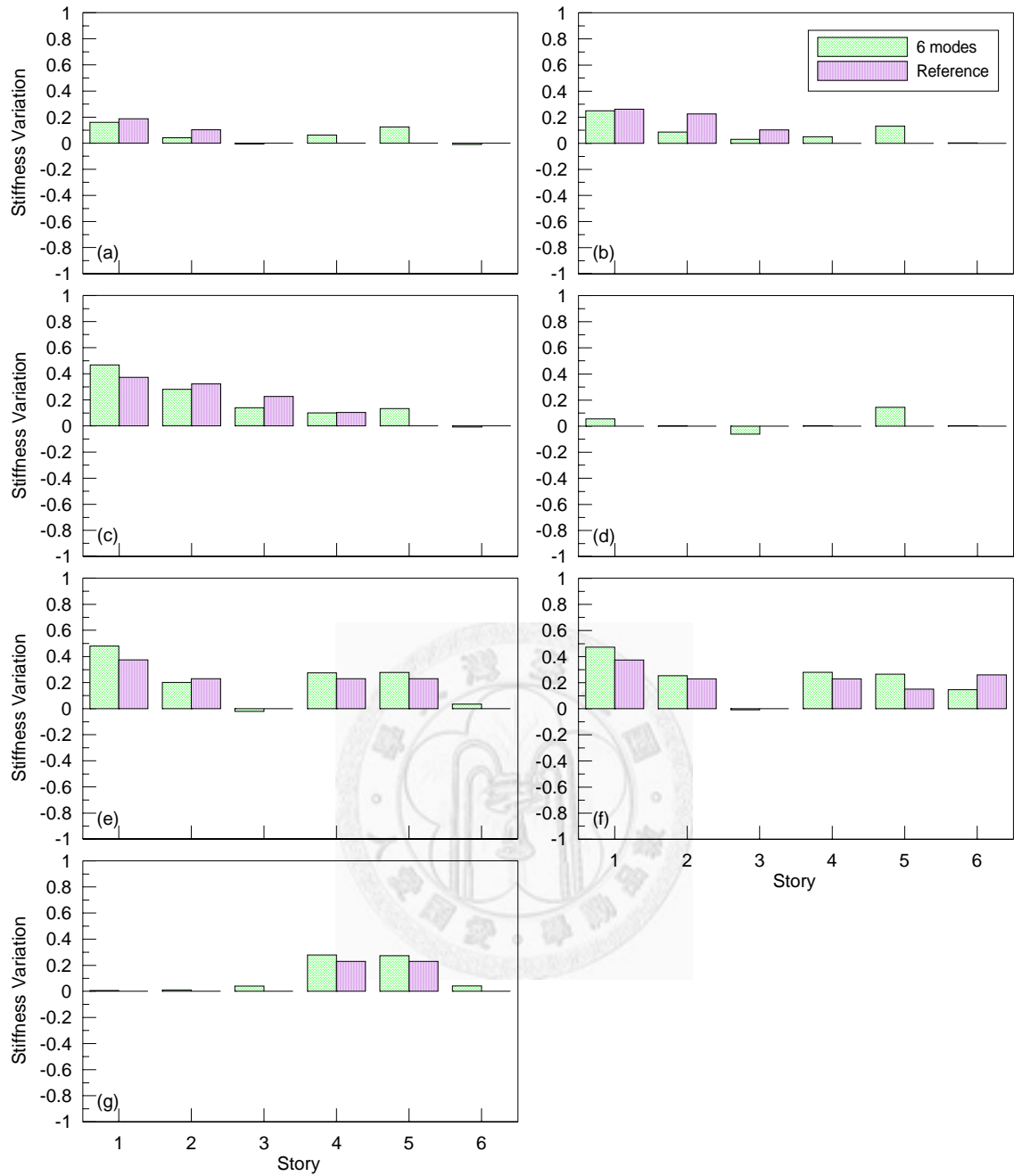
Figure 4-32: Estimated relative change of stiffness of 6-story steel building structure obtained by **Eq. (2-46)** using the first 6 mass-normalized **complex**-value mode shapes from the experimental studies: (a) Case R2; (b) Case R3; (c) Case R4; (d) Case R5; (e) Case R6; (f) Case R7; (g) Case R8.
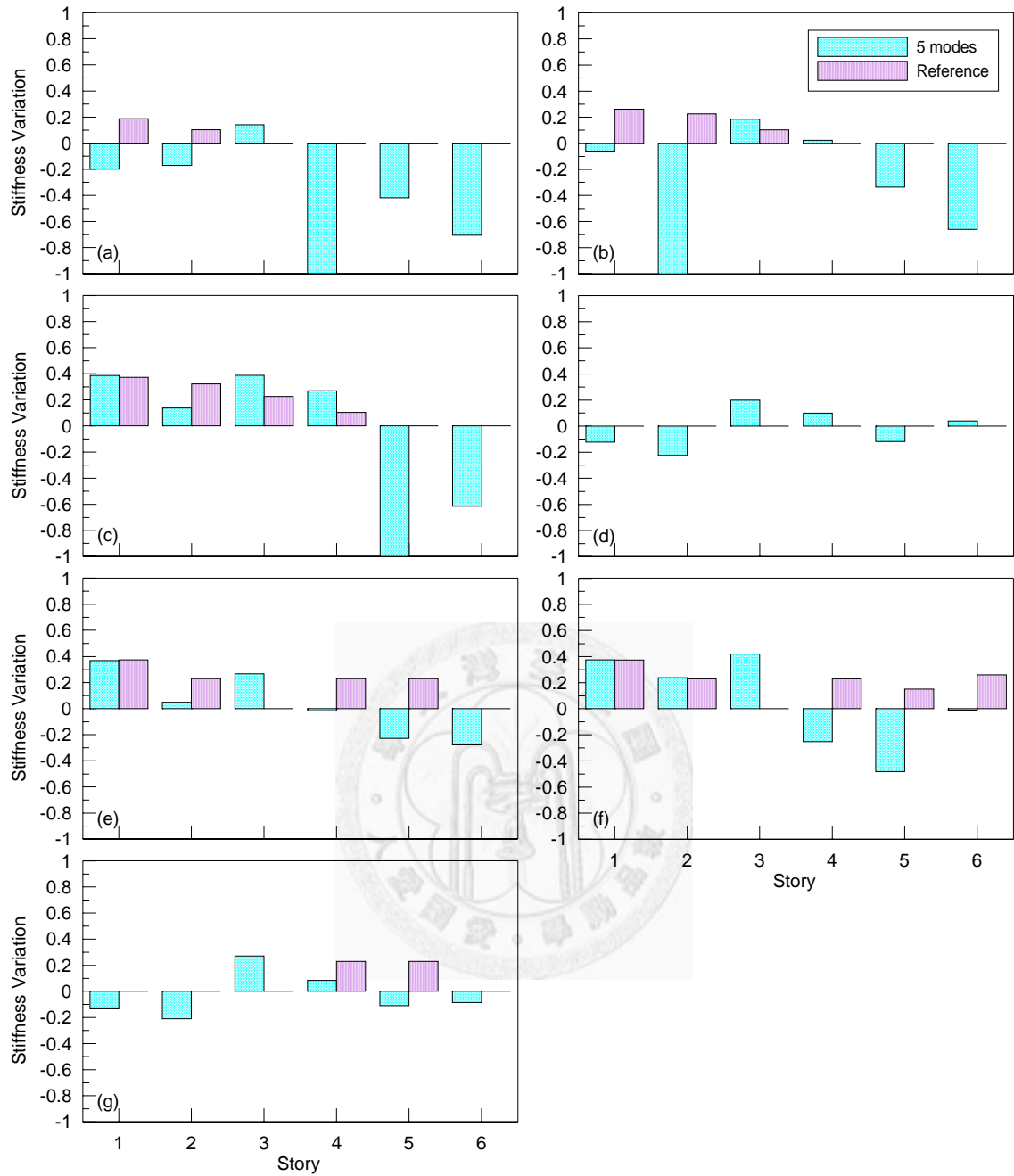
Figure 4-33: Estimated relative change of stiffness of 6-story steel building structure obtained by **Eq. (2-46)** using the first 5 mass-normalized **complex**-value mode shapes from the experimental studies: (a) Case R2; (b) Case R3; (c) Case R4; (d) Case R5; (e) Case R6; (f) Case R7; (g) Case R8.
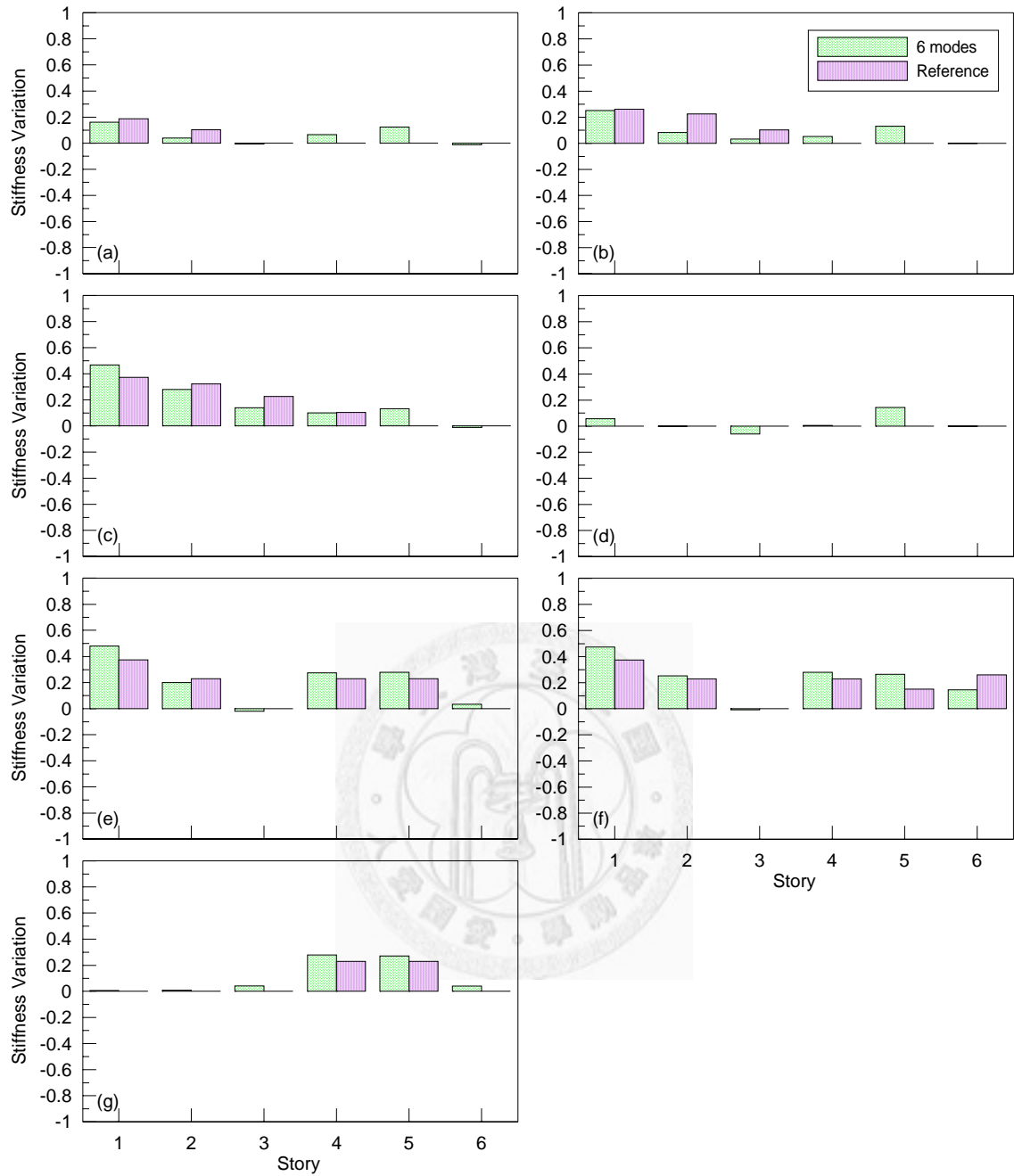
Figure 4-34: Estimated relative change of stiffness of 6-story steel building structure obtained by **Eq. (2-46)** using the first 6 mass-normalized **real**-value mode shapes from the experimental studies: (a) Case R2; (b) Case R3; (c) Case R4; (d) Case R5; (e) Case R6; (f) Case R7; (g) Case R8.
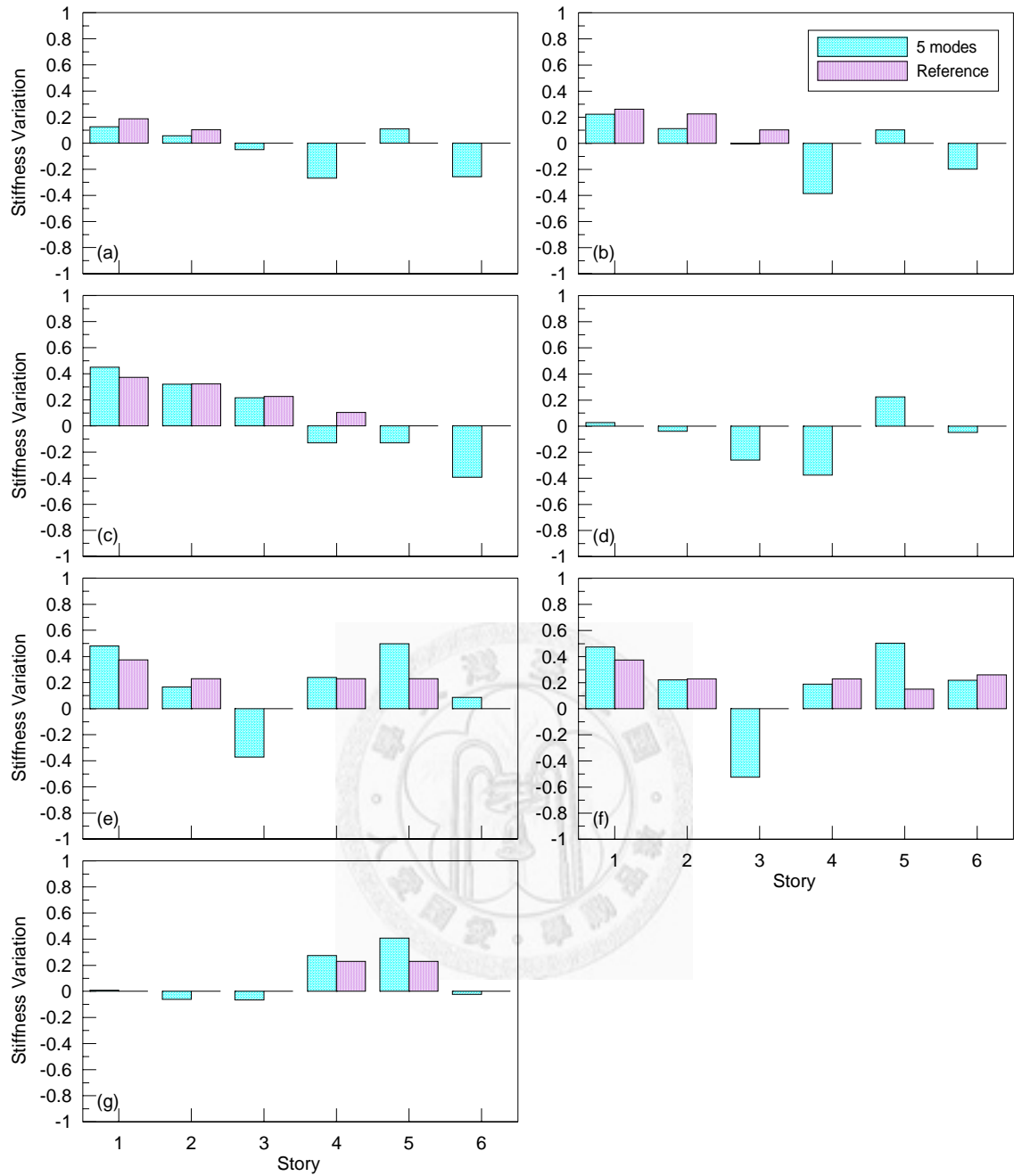
Figure 4-35: Estimated relative change of stiffness of 6-story steel building structure obtained by **Eq. (2-46)** using the first 5 mass-normalized **real**-value mode shapes from the experimental studies: (a) Case R2; (b) Case R3; (c) Case R4; (d) Case R5; (e) Case R6; (f) Case R7; (g) Case R8.
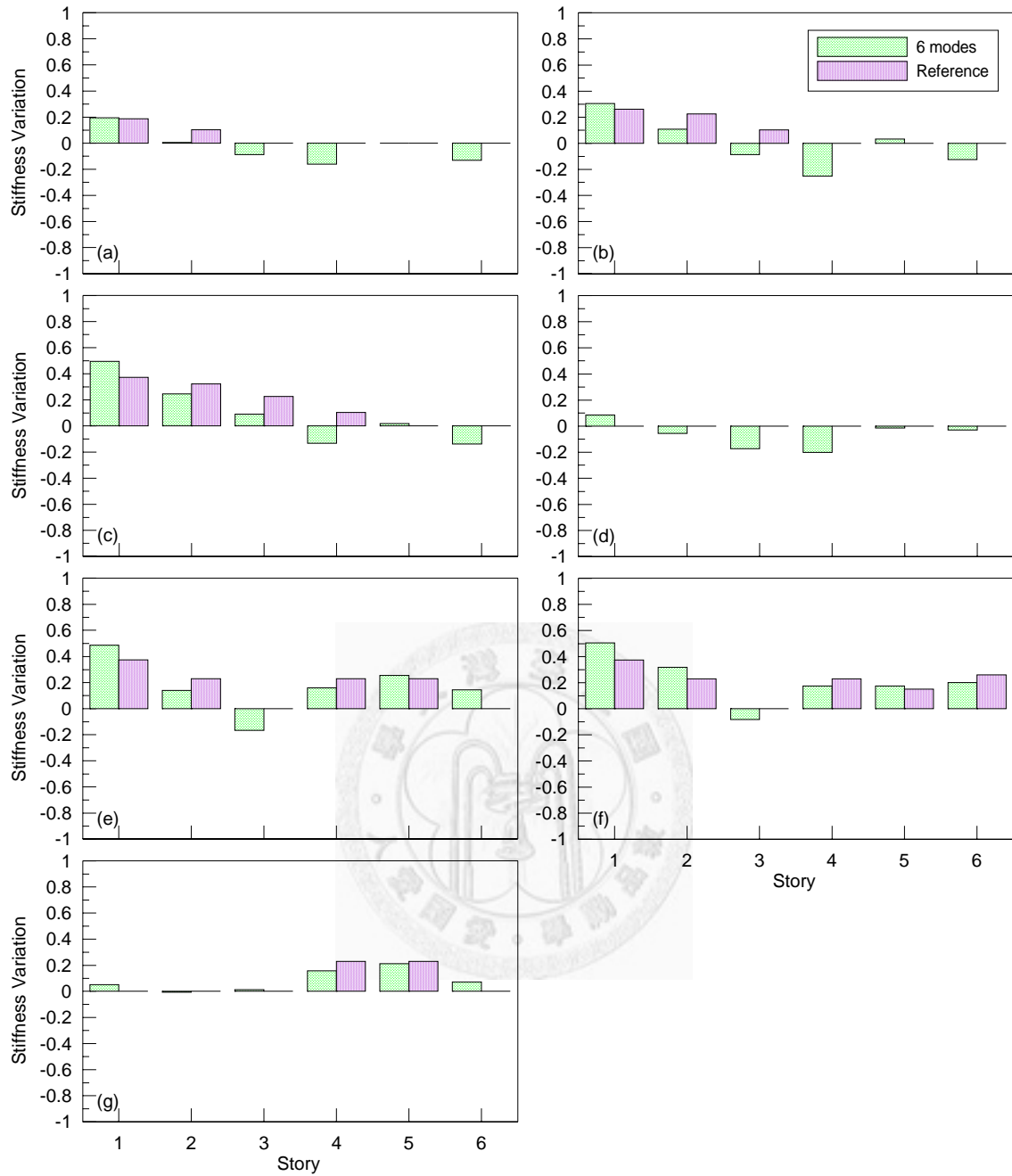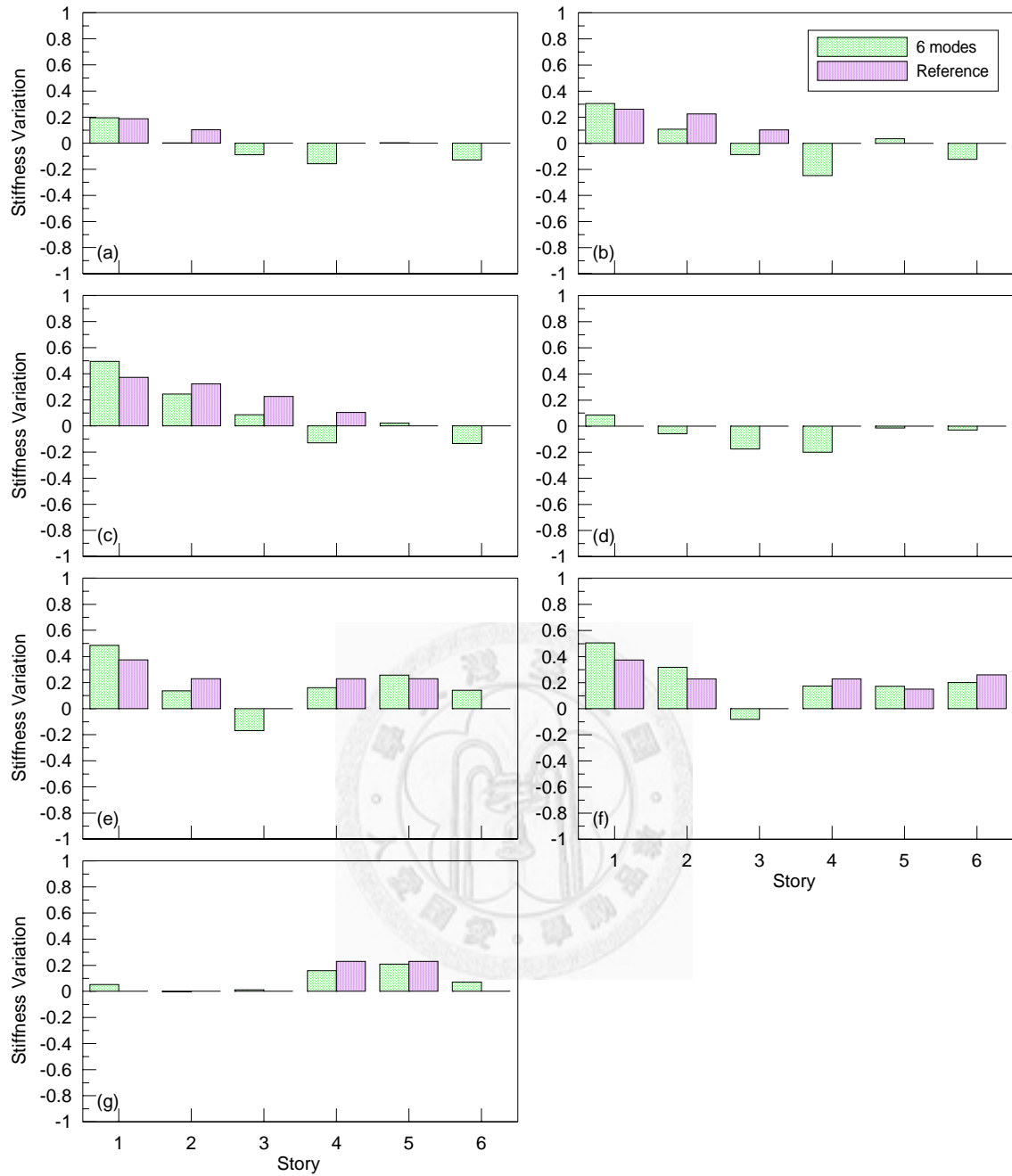
Figure 4-36: Estimated relative change of stiffness of 6-story steel building structure obtained by **Eq. (2-41)** using the first 6 **non-mass-normalized** real-value mode shapes from the experimental studies: (a) Case R2; (b) Case R3; (c) Case R4; (d) Case R5; (e) Case R6; (f) Case R7; (g) Case R8.
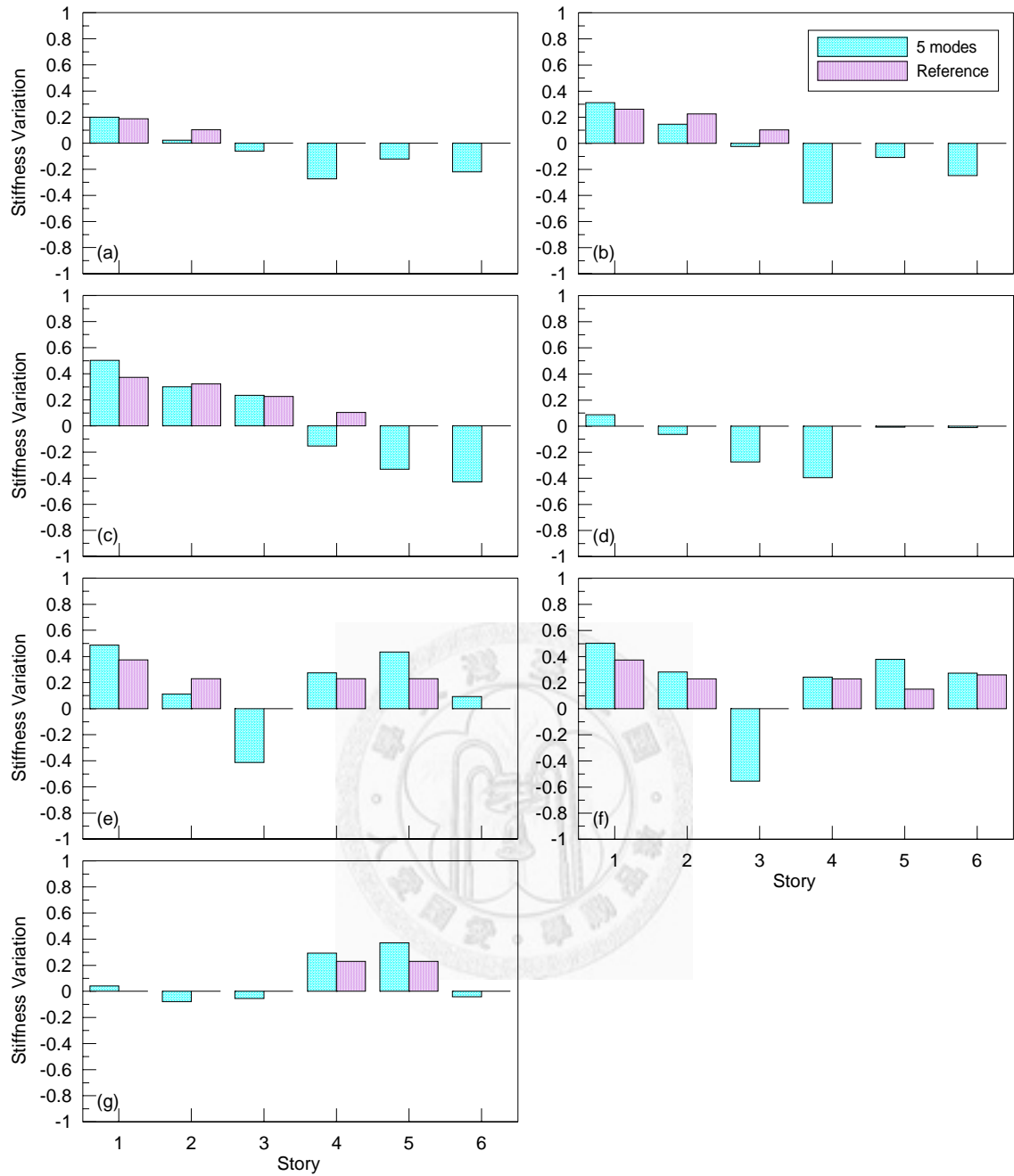
Figure 4-37: Estimated relative change of stiffness of 6-story steel building structure obtained by **Eq. (2-41)** using the first 5 **non-mass-normalized** real-value mode shapes from the experimental studies: (a) Case R2; (b) Case R3; (c) Case R4; (d) Case R5; (e) Case R6; (f) Case R7; (g) Case R8.

5. DAMAGE DETECTION ACCOMMODATING NONLINEAR ENVIRONMENTAL EFFECTS

The damage of a structure may be detected through the variation of the structural features such as eigenfrequencies, modal damping, mode shapes, damage indexes, stiffness matrices, *etc*. However, in most of the previous studies, these identified structural features were assumed under a constant environmental condition. Generally, for case of continuous monitoring the structure behavior is affected by the changing environmental conditions such as temperature, humidity, loading conditions, and boundary conditions. The variation of the identified structural features due to the varying environmental conditions may smear the changes caused by structural damages; therefore, false damage diagnosis can be concluded.

A technique is proposed in this thesis to accommodate nonlinear varying environmental effects in the identified stiffness reduction of structural components (Level-III damage detection) without measuring the environmental factors as a prior. Once the target features are identified or measured under varying environmental conditions, the actual trend caused by the intrinsic unmeasured system variables can be extracted by the nonlinear principal component analysis (NPCA). Then the variation of the features caused by damage is determined more accurately by the proposed prediction model, which is achieved by solving an optimization problem.

In the first section of this chapter, the methodology of NPCA is introduced, and then the optimization problem for applying the prediction model of NPCA is defined and explained using a simple example. The efficiency of the proposed approach is illustrated using a synthetic bridge model with the consideration of the specific element stiffness reduction together with the element stiffness change due to varying environmental conditions including temperature, gradient of temperature, humidity and frozen of supports.

5.1. Methodology

A methodology is proposed to perform damage detection of structural components accommodating nonlinear environmental effects provided that the target features of structural components can be identified. In this thesis, the stiffness of structural components is selected as the key target feature for demonstration. The environmental factors which affect the structural features are not necessary to be measured for damage detection using the proposed methodology. The proposed methodology of NPCA and the associated prediction model are explained in detail in this section.

5.1.1. Nonlinear Principal Component Analysis

The identified stiffness of structural components under varying environmental conditions when the structure is intact is used to conduct NPCA. The environmental factors are not necessary to be measured for this technique. Let $\aleph \in \mathbb{R}^{J \times P}$ represents the matrix whose column vectors κ_p are the stiffness values of the components of the system identified at any particular time t_p, where J is the dimension of data and P is the number of data set. In order to detect the percentile reduction of the stiffness values directly, the matrix $\aleph$ is formed by the data which has been standardized as

$$\kappa_{jp} = \frac{\hat{\kappa}_{jp} - \mu_j}{\mu_j} \times 100 \qquad (5-1)$$

where $\hat{\kappa}_{jp}$ is the non-normalized feature of the jth component at time t_p, and μ_j is the mean of the row vector $\hat{\kappa}_j$.

After the data of structural component stiffness under varying environmental conditions is prepared, the NPCA technique is performed to extract the underlying environmental trend when the system is in its intact condition. These intact data sets will be used for training and validating the neural networks.

Kramer (1991) proposed the NPCA algorithm by applying the auto-associative neural network (AANN) to perform feature extraction. The AANN is a particular class of

neural networks in which the target output pattern is identical to the input pattern. In this thesis the NPCA is used to extract the intrinsic environmental trend causing the variation of structural components stiffness. The architecture of AANN is described as follows.

There are five layers in the typical AANN as illustrated in Figure 5-1, where σ represents sigmoid transfer function and l represents the linear transfer function. The AANN seeks mapping and de-mapping functions simultaneously which are represented as

$$\boldsymbol{Z} = F(\aleph) \tag{5-2}$$

and

$$\hat{\aleph} = G(\boldsymbol{Z}) \tag{5-3}$$

The first half of AANN represents the mapping function F which operates on the rows of $\aleph$ and has J inputs. The mapping layer of F contains M nodes with sigmoid transfer functions and projects the input pattern $\aleph$ into $\boldsymbol{Z}$ feature space with d dimensions. The number of nodes in the bottleneck layer, d, in $\boldsymbol{Z}$ feature space is actually the number of nonlinear principal components and is usually less than M and J. The second half of AANN represents the de-mapping function G which takes the rows of $\boldsymbol{Z}$ as inputs and accordingly has d inputs. The de-mapping layer contains the same M nodes of sigmoid transfer functions and projects the $\boldsymbol{Z}$ feature space back into original $\aleph$ space with J dimensions.

Cybenko (1989) had proved that the function F and G can fit any nonlinear function $z = f(\kappa)$ expressed in the following form

$$z_p = \sum_{j=1}^{N_2} m_{jp}^2 \upsilon(\sum_{i=1}^{N_1} m_{ij}^1 \kappa_i + b_j) \tag{5-4}$$

where z_p and κ_i are the pth and ith components of z and κ respectively; m_{ij}^p represents the weight connecting the ith node in the pth layer to the jth node in the

$(p+1)^{\text{th}}$ layer; b_j is a nodal bias; N_i is the number of nodes in each layer. $\upsilon(x)$ is a continuous and monotonically increasing function with the output range of 0 to 1 for an arbitrary input κ.

Supervised learning is applied to train AANN. Specially, $\aleph$ is both the input and output of AANN. The residual error e_r is measured by $e_r = \aleph - \hat{\aleph}$. The mapping function F and de-mapping function G are computed to minimize Euclidean norm of the residual error, $\|e_r\|$. Thus the AANN is trained to reconstruct the original data and to extract the underlying nonlinear principal components (NLPCs) simultaneously. As a result, the latent relationship between the identified features (*e.g.* structural component stiffness) and the unknown intrinsic features (*e.g.* environmental factors) causing the variations of the identified features is revealed.

Based on the residual error e_r of the validating data of the intact system, the threshold of each component for separating the suspected damage data from those of the intact data can be determined. Provided the residual error e_r of the intact stiffness values is Gaussian distribution, the point with residual error less than mean minus two times of the standard deviation σ is only 2.5% of all data. However, such a threshold level makes about 2.5% of the intact data be identified as the damage case, which means that false alarm may be issued quite frequently. To avoid the false alarm caused by noise or other effect, it is suggested to issue an alarm only when three consecutive residual errors exceed the threshold. If the noise is Gaussian distribution and the system is intact, the possibility for three consecutive residual errors exceeding the threshold is only $(2.5\%)^3=0.001563\%$. Although the reliability of damage alarm can be increased if a lower threshold is chosen, on the contrary the sensitivity of damage extent may be sacrificed. Therefore, determination of threshold depends on engineering judgment.
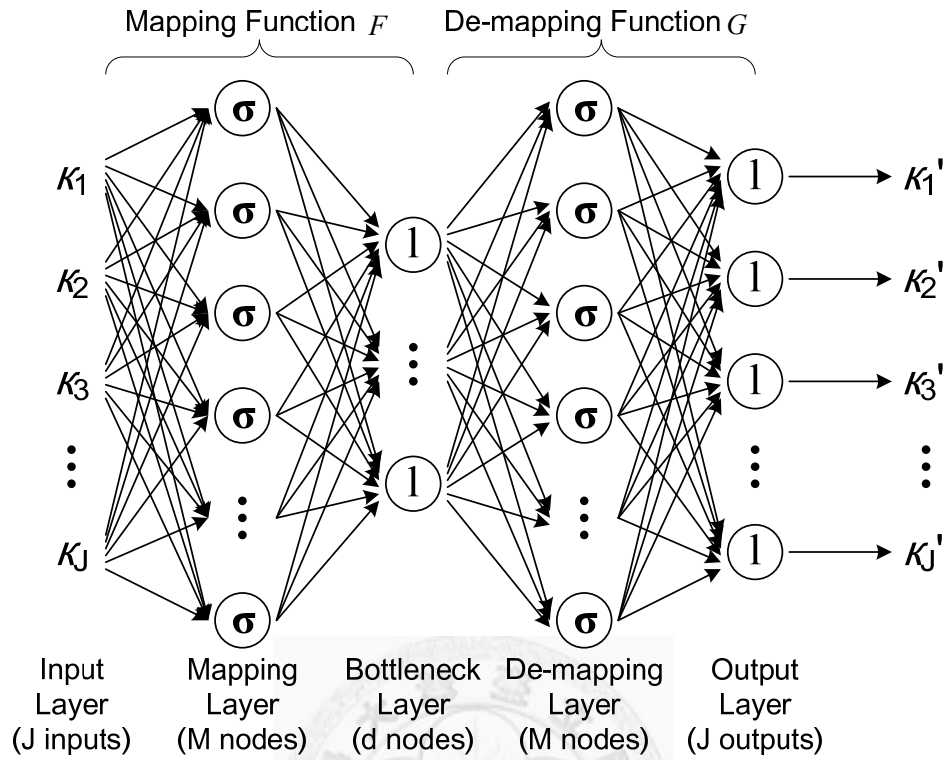
Figure 5-1: Network architecture of AANN for implementation of NPCA.
(modified from Kramer 1991).

5.1.2. Prediction Model

Consider a simple system with two components as an example. If the system is continuously monitored and enough data of the stiffness values (k_1 and k_2) under varying environmental conditions are identified, the NLPCs of these two features, *i.e.* the solid line in Figure 5-2, can be extracted by training the AANN. Note that the stiffness values are semi-normalized by Eq. (5-1) and thus are expressed in percentage.

In this section, a single damaged data point under certain environmental condition is used to demonstrate the concept of the prediction model of NPCA. Assuming this single damage data represents 4% stiffness reduction of the second component, the stiffness values of the system may be identified as the dot point in Figure 5-2(a). This dot point is projected onto the space formed by the NLPCs using Equation (5-2), obtaining the double-circle point in Figure 5-2(a). Afterward, this double-circle point can be transferred back to the original two-dimensional feature space using Eq. (5-3). The

residual error e_r of this data due to the mapping and de-mapping of AANN is actually a vector from the dot point to the double-circle point in Figure 5-2(a). This vector indicates the stiffness values of the first and second components approximately increase by 2% and decrease by 2% respectively. However, since the stiffness values of the damaged structural components should indicate a decreasing value, the increase of stiffness value of the structural component after the system is damaged is physical meaningless. A better result can be obtained by assuming that the first component is not damaged and the second component is damaged. In other words, the damage extent can be obtained more accurately by seeking the true features when the system is intact under the same environmental condition. These true intact features are denoted as a "predicted point" and can be obtained by minimizing the object function Π as defined

$$\Pi = \left\| \tilde{\aleph} - G(F(\tilde{\aleph})) \right\|^2, \quad \tilde{\aleph} = \left\{ \begin{array}{c} \overline{\kappa}_u \\ \kappa_d \end{array} \right\} \tag{5-5}$$

where $\overline{\kappa}_u$ represents the known stiffness variation of the intact components and κ_d represents the unknown stiffness variation of the damaged components. Note the sequence of $\tilde{\aleph}$ is the same as $\aleph$. Thus the predicted damage extent is obtained by

$$e_p = \aleph - \tilde{\aleph} \tag{5-6}$$

In this two-dimensional case, the predicted point is actually the double-circle point in Figure 5-2(b). As a result, the damage extent of the second component is predicted as approximately 4%, which is the same as the designated one.

It should be noted that, as discussed in Section 1.4.4, the variations of structural component stiffness due to damage should behave in different manners from those due to varying environmental conditions, otherwise this approach will fail. Fortunately, the variation of features caused by damage generally departs from the one caused by environmental effects since damage usually occurs at local components while environmental factors usually affect the structure globally. For the circumstance when these two variations of features are analogous, it is suggested to measure the environmental factors and include them in the AANN.
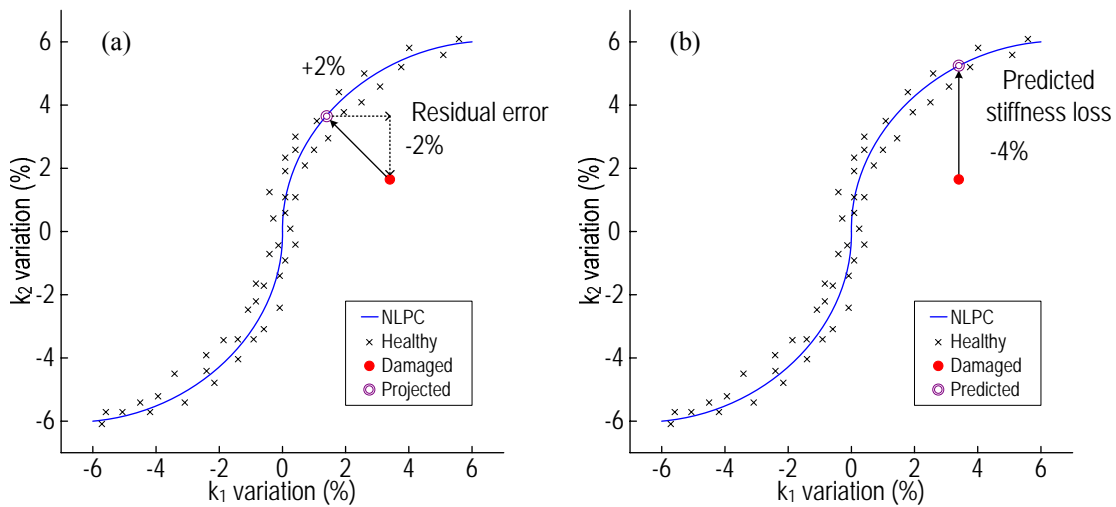
Figure 5-2: Two-dimensional example for demonstration of (a) residual error; (b) predicted stiffness loss.

5.2. Numerical Validation

5.2.1. The Identification Model

The proposed damage detection approach is demonstrated using a synthetic bridge model as illustrated in Figure 5-3. The bridge was composed of 9 components including 4 components of concrete decks, 3 components of steel decks paved with asphalt, and 2 elastic springs to simulate the changing boundary conditions. The length of each deck was $10m$. The Young's modulus of the concrete and steel decks were $2.48 \times 10^{10} N/m^2$ and $2.04 \times 10^{11} N/m^2$, respectively. The moment of inertia of the concrete and steel decks were $8.10m^4$ and $1.28m^4$, respectively. The stiffness of the spring number 1 and 2 were $1 \times 10^9 N/m$ and $2 \times 10^9 N/m$, respectively. The mass was lumped on each node; for concrete element, the translation inertia and rotary inertia was $3.31 \times 10^5 kg$ and $27.6 \times 10^5 kg - m^2$, respectively; for steel element, the translation inertia and rotary inertia was $1.13 \times 10^5 kg$ and $9.44 \times 10^5 kg - m^2$, respectively.
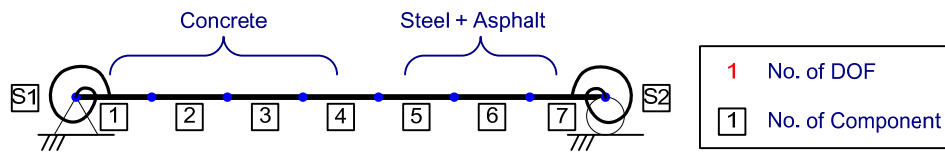
Figure 5-3: A synthetic bridge model.

5.2.2. Synthetic Environmental Effects

This bridge was assumed being monitored under the changes of different environmental conditions including temperature, temperature gradient, humidity, and frozen of supports during a period of continuous monitoring. The hypothetical relationships between the Young's modulus of each kind of structural component and the temperature and humidity are demonstrated in Figure 5-4. It should be noted that the temperature effect when asphalt is under freezing point was simulated to imitate the behavior of Z-24 Bridge (Peeters and De Roeck 2001) as shown in Figure 1-1. The frozen of the supports were simulated by increasing the stiffness of the springs dramatically if the temperature of the adjacent deck was under $0°C$. The frozen of support made the first eigenfrequency of the system increase about 50% maximum. The temperature was generated uniformly random distributed between $-10°C$ and $50°C$. The humidity was generated uniformly random distributed between 60% and 100%. The temperature gradient was considered distributed from the first deck to the last one with random magnitude and with maximum difference of 20 degree, either increasing or decreasing.

5.2.3. Damage Cases

Four cases were studied for the synthetic bridge model. The noise level, damaged components and damage extent of these case studies were listed in Table 5-1. In order to demonstrate the results clearly, only one component was designated damaged in the first case study. The second case study investigated the ability to identify multiple damaged components. The third case study raised the noise level to examine the effect of higher noise level. The forth case study inspected the case with different damage elements and

larger damage extent. For each case study, 600 intact samples and 50 damaged samples were generated. The first 500 of the intact samples were used for training and validating of the AANN. The rest 100 of the intact samples and the 50 damaged samples were used to verify the proposed technique.

In the first case study, only the component No.6 was damaged, and 1% noise was added to the stiffness of each element. For demonstration, only 100 intact and 50 damaged samples are presented. The identified stiffness values of the 5th and 6th components under varying environmental conditions are demonstrated in Figure 5-5. From the data distribution in Figure 5-5 it is not easy to judge reliably and immediately whether the components are damaged or not since the deviation of data caused by environmental effects smears the damage data.
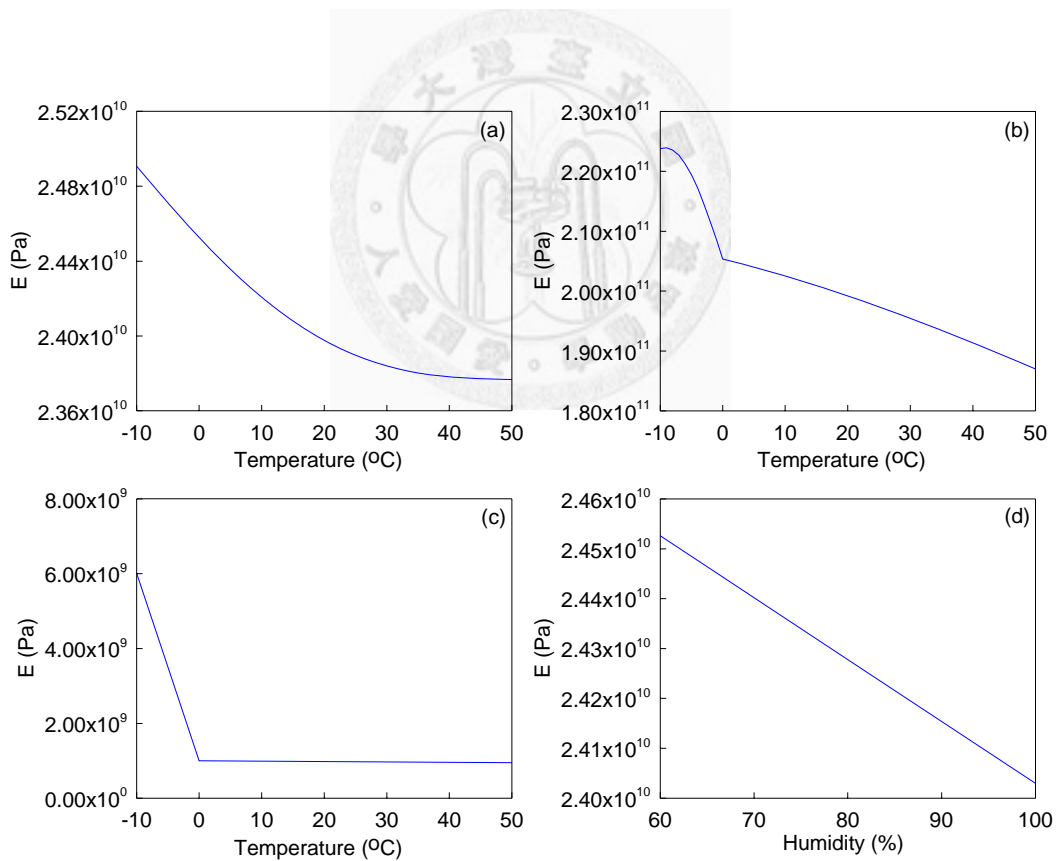

Figure 5-4: Young's modulus of (a) concrete deck vs. temperature when humidity equals 60%; (b) steel deck vs. temperature; (c) spring (s2) vs. temperature; (d) concrete deck vs. humidity when temperature equals $0°C$.

5.2.4. Numerical Results

Before the data set, $\aleph$, is used to train the AANN, normalization using Equation (5-1) is performed. Thus the decreasing value of the data relates directly to the percentage of component stiffness loss. Basically the number of d-nodes of AANN depends on the number of underlying factors in the data. In practice, the number of underlying factors is not known. However, similar to the PCA, the selection of exact number of nonlinear principal components to represent the underlying factors is not very critical (Yan *et al.* 2005a; Giraldo *et al.* 2006). It is recommended to choose a series of d for verification. For all the numerical studies, d was chosen as 2.

It is well known that the number of neurons in the mapping and de-mapping layers relates to the complexity of the nonlinear functions represented by the neural network. Enough number of neurons for mapping is required so as to get satisfying accuracy. On the other hand, over-fitting caused by too many mapping neurons should be avoid otherwise the network may learn the stochastic nature of data rather than the underlying functionalities. Therefore, the Akaike's final prediction error (FPE) (Akaide 1974) is introduced to determine the number of M. For all the numerical studies, M was chosen as 8.

Once the AANN was trained, based on the residual error e_r of the validating data of the intact system, the threshold of each component for separating the suspected damage data from those appears intact was determined as mean minus two times of the standard deviation (*i.e.* $\mu_j - 2\sigma_j$). The damage alarm could be issued when three consecutive residual errors exceed the threshold. Figure 5-6 provides the residual error of the 5th and 6th components for Case N1 study. The threshold for the 5th and 6th component was -2.02% and -1.93% respectively. When the components were intact, only a few intermittent points exceeded the threshold and no false alarm was issued. When the 6th component was damaged, the residual error of the damaged component consecutively exceeded the threshold. The mean value of the residual error of the damaged component was -4.14%, while the designated damage extent is -5%. Figure 5-7 presents the predicted stiffness loss of these two components obtained by Equations (5-5) and (5-6). The mean value of the predicted stiffness loss when the component was damaged was -4.96%. It is evident that the predicted stiffness loss was approximately the same as the

designated one.

Table 5-1 summarizes the results for all N1 to N4 case studies. The mean value of the predicted stiffness loss of 3 consequent data points whose residual error consecutively exceeds the threshold was also listed, as well as the number of samples needed to issue alarm after the true damage occurred. All values of the predicted stiffness loss provided a good estimate of true extent of damage, except the 6th component in Case N3 where noise level was so big that small damage could not be detected. Most of the alarm was issued after only 3 samples were recorded, which indicates that the damage could be detected promptly with high confidence. Furthermore, no false alarm was issued in all the N1 to N4 case studies, indicating high reliability for the proposed technique.

Table 5-1: Summary of the patterns and results of case studies.

Case	Noise Level	Damage Component	Damage Extent	Predicted Stiffness Loss	Samples Needed to Issue Alarm
N1	1.0%	6	5.0%	4.06%	3
N2	1.0%	1	5.0%	4.64%	3
		2	5.0%	4.71%	3
		6	5.0%	5.58%	3
N3	5.0%	1	20.0%	22.63%	3
		2	10.0%	11.65%	8
		6	5.0%	-	-
N4	5.0%	3	10.0%	12.62%	6
		4	20.0%	23.14%	3
		7	50.0%	51.16%	3

Figure 5-5: The original stiffness including 100 intact (first 100 samples) and 50 damaged samples (last 50 samples) of the (a) 5th component; (b) 6th component.

Figure 5-6: The residual error including 100 intact (first 100 samples) and 50 damaged samples (last 50 samples) of the (a) 5th component; (b) 6th component.

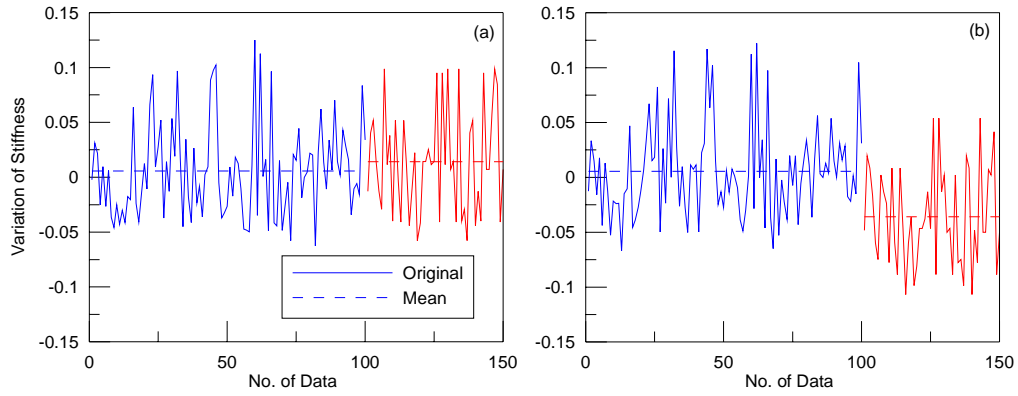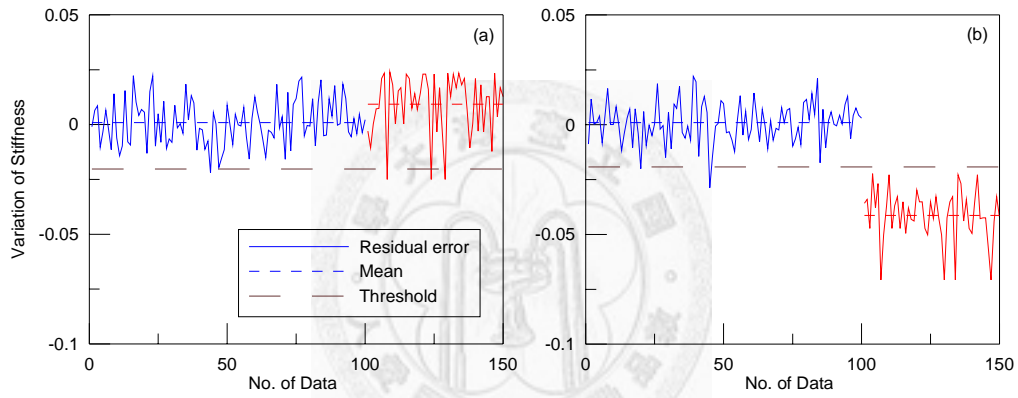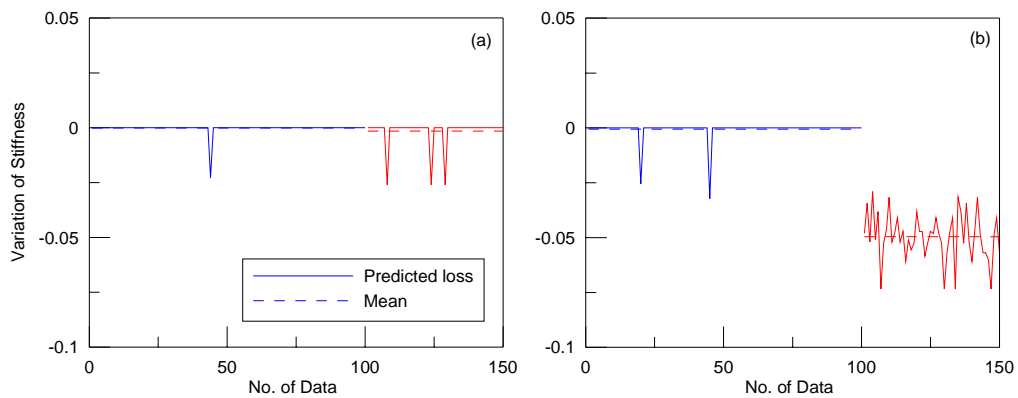Figure 5-7: The predicted stiffness loss including 100 intact (first 100 samples) and 50 damaged samples (last 50 samples) of the (a) 5th component; (b) 6th component.

6. CONCLUSIONS AND FUTURE WORKS

6.1. Conclusions

The objective of this thesis is to develop techniques to localize and quantify damage in civil structures under nonlinear environmental effects. The FRFC method and the modified MSEC method are developed to perform Level-III damage detection. Both algorithms are verified by numerical and experimental studies. The feasibility of the LFM to perform Level-III damage detection of building structures is also studies with numerical and experimental cases. It is assumed that the stiffness variation of the structural components is identified from the measured data within a short duration where environmental factors are constant. In practice, the stiffness variations identified at different time fragments always fluctuate with environmental factors. The stiffness variation caused by damage may be smeared by these environmental effects. To treat the environmental effects, the algorithm using NPCA to extract the underlying environmental trend is proposed. Then the stiffness variations caused by damage is determined more accurately by the proposed prediction model. Numerical studies are conducted to verify this algorithm.

The main conclusions of this thesis are summarized as the followings:

The Modified Modal Strain Energy Change Method

The modified MSEC method is developed to overcome some difficulties when applying MSEC method to the 3D steel building structure with relatively sparse measurement. The following conclusions can be drawn from the numerical studies and experimental studies.

➢ When selecting suspected damage elements according to the MSECR of each element, it is proposed to calculate MSECR without taking absolute MSEC value rather than taking absolute MSEC value. It is illustrated that better localization can be achieved because fewer suspected damage elements are selected without missing the true damaged elements. Selecting fewer suspected

elements is important for reducing ill-posed problem when solving the damage identification equations.

➢ The measured incomplete mode shapes is suggested to be expanded by dynamic expansion algorithm instead of by SEREP algorithm. From the numerical studies, it is found that better damage localization and more accurate damage quantification can be achieved using the dynamic expansion algorithm.

➢ The elements with relatively small MSE may induce abnormal MSECR. It is suggested to avoid the abnormal MSECR by setting a threshold of MSE. From the numerical studies, it is observed that more accurate damage localization can be achieved with employing the threshold of MSE.

➢ In addition to the sensitivity equations of MSEC respect to elemental stiffness change in the damage identification equations of the original MSEC method, the sensitivity equations of eigenvalue respect to elemental stiffness change are also considered in the damage identification equations. Through the numerical studies and experimental studies on a 3D 3-story steel building structure, it is proved that the ill-posed problem when solving the identification equations is suppressed by adding these equations.

➢ The damage identification equations are expanded from considering sensitivity of "lump elemental stiffness variation ratios" to considering sensitivity of "elemental sectional property variation ratios". The numerical studies and experimental studies indicate that more reliable and consistent results are obtained if the expanded damage identification equations are employed.

➢ For the MSEC method, the measured mode shapes with incomplete DOFs are expanded to complete mode shapes according to the analytical FE model of the structure. The target MSEC in the iteration process is calculated based on these complete mode shapes. A new iteration process which updates the target MSEC according to the mode shapes expanded based on the stiffness matrix obtained in the last step is proposed. The new iteration process will be terminated according to the proposed convergence criterion based on MAC between each mode. The numerical studies illustrates that the accuracy can be improved by using the proposed iteration process.

➢ Less measurement increases the difficulty of vibration-based damage detection. This is illustrated by the numerical studies of the 3D building structure. While all modes with complete analytical DOFs are capable to detect damage, only a

few lowest modes expanded from sparse DOFs are capable to detect damage. The experimental studies of the 3D building structure with relatively sparse measurement present that damage quantification of the truly damaged sectional properties can be fairly identified even though the stiffness reduction factors of other properties seem to be contaminated. The errors are attributed mainly to modal expansion from limited numbers of DOFs, as well as to the combination of modal expansion, modeling error and measurement noise.

The Frequency Response Function Change Method

The FRFC method to perform Level-III damage detection based on the change of the FRFs of a linear structure under ground excitation is proposed in this thesis. The FRFC method uses the geometry information of the structure to circumvent ill-posed problem when solving the variation of stiffness matrix from the damage identification equations. This idea is illustrated by applying it to a shear building structure. The information required for the FRFC method includes: (i) FRFs of the structure both prior and posterior to damage and (ii) a well-estimated dynamic stiffness matrix when the structure is intact.

The FRFs at frequencies with higher signal-to-noise ratio, *e.g.* frequencies close to the eigenfrequencies of the structure, are suggested to be utilized to reduce the errors caused by measurement noise. Because the least-square solution of the damage identification equations depends on the magnitude of coefficient in each equation; therefore the damage identification equations are solved using the frequencies close to each eigenfrequency of the structure separately. The results obtained with different set of frequencies are suggested to be weighted according the proposed results similarity criterion. The numerical studies illustrate that the results similarity criterion can reduce the errors caused by both measurement noise and modeling error.

The dynamic stiffness matrix of the intact structure identified using subspace identification techniques with a known mass matrix can be utilized to replace the analytical one constructed from a FE model; this circumvents the troublesome process of FE model-updating and at the same time makes the FRFC method much less model-dependent. If the mass matrix of a shear building structure is diagonal, it is

illustrated that the stiffness variation ratio of each story can be obtained without knowing the value of the mass matrix. In this case, the FRFC method is almost non-model-based.

According to the results of numerical studies which consider measurement noise and modelling error, the proposed FRFC method is proved realistic. It is observed that the modeling error causes unbiased error while the measurement noise causes biased error. The experimental studies using the 1/4-scale 6-story steel building structure with several damage cases reveals that the proposed FRFC method is feasible to detect the damage with acceptable accuracy.

An operational scheme is proposed to integrate the FRFC method with wireless sensing systems to take the advantage of collocated computing resources of wireless sensing systems and reduce the energy consumed by wireless sensing units at the same time. Necessary algorithms for FRFC method are imbedded into the wireless sensing units to realize the proposed operational scheme. On-line Level-III damage detection of the same 6-story steel building structure using the FRFC method integrated with the wireless sensing systems is successfully accomplished.

The Local Flexibility Method

Numerical studies on the feasibility of the LFM are conducted with a shear-type low-rise building structure and a flexible high-rise frame building structure. For the shear-type low-rise building structure, 4 modes out of 6 modes are required to obtain a reasonable result. For the flexible high-rise frame building structure, only 5 modes out of 100 modes are required to obtain a reasonable result. Combining the results of the LFM applying to beam structures and bridges in the literature and results in this thesis, it seems that only the lowest few modes may be enough for the LFM to detect damage with acceptable accuracy, especially for a flexible structure like a high-rise building, a beam structure and a bridge.

The LFM is also verified by experimental studies on the 1/4-scale 6-story steel building structure with several damage cases. It is found that the algorithm to construct a

flexibility matrix using Eq. (2-46) may have ill-posed problem with truncated modes. A suggestion is made to use another algorithm, *i.e.* Eq. (2-41), to avoid ill-posed problem while constructing a flexibility matrix. Theoretically, the mode shapes utilized in Eq. (2-41) should be mass-normalized. However, it is illustrated by the experimental studies that the "relative" flexibility matrices constructed using non-mass-normalized mode shapes by Eq. (2-41) are possible to be used for the LFM if the structure is mass-distributed. By doing so, the troublesome work of obtaining a mass matrix by establishing a finite element model can be circumvented.

The Method Treating Nonlinear Environmental Effects

A new method which deals with environmental effects on the identified structural features, *e.g.* damage extent of each component, without measuring the environmental factors is proposed, especially for nonlinear environmental effects. The underlying environmental factors can be extracted by nonlinear principal component analysis using auto-associative neural network. The residual error due to mapping and de-mapping of the auto-associative neural network when the structure is intact is used to decide the threshold for separating suspected damaged samples from the intact one. Then the extent of stiffness loss is calculated by the prediction model of NPCA through solving an optimization problem.

The proposed methodology for treating environmental effects is verified by a synthetic bridge model which considers a specific element stiffness reduction together with the change due to environmental conditions including temperature, gradient of temperature, humidity and frozen of the supports. Results show that the extent of stiffness loss can be quantified accurately and promptly after the damage is introduced.

One of the benefits of this approach is that the environmental factors are not necessary to be measured. Note that the application of this technique is not limited to the identified stiffness value. The structural features with the variation that is non-decreasing or non-increasing, *e.g.* damage index, when damage occurs are also valid for this technique.

Note that enough data when the system is intact are required to perform NPCA for training the AANN. If the environmental conditions depart significantly from the exposure history during the data collection, the proposed technique may fail. Fortunately, the most important environmental factor, *i.e.* temperature, is almost periodic in one year of view. The highest and lowest temperatures of each year do not change significantly. However, for those environmental effects which are not known well, preliminary observations and studies are necessary. Otherwise, one needs to update the training database once the false-positive alarm due to obscure environmental effect is observed.

It should be noted that the variations of structural component stiffness due to damage should behave in different manners from those due to varying environmental conditions, otherwise this approach will fail. Fortunately, the variation of features caused by damage generally departs from the one caused by environmental effects since damage usually occurs at local components while environmental factors usually affect the structure globally. For the circumstance when these two variations of features are analogous, it is suggested to measure the environmental factors and include them in the AANN.

6.2. Future work

It is found that large error is introduced to the MSEC method if mode shapes are obtained from expanding from relatively sparse measurement. Therefore, it might be appropriate to develop an algorithm to determine the optimal DOFs to be measured to perform damage detection with less error attributed to inadequate sensor locations. Besides, as cost of sensors may continue to lower, more sensors are possible to be installed in a structure; this benefits the results of vibration-based damage detection. Since the number of sensors is not constraint to budget so hardly in the near future, it might also be appropriate to develop an algorithm to determine the cost-effective number of sensors to be installed in a structure to perform damage detection.

Although the theoretical basis of the local flexibility method is general to any structure

type, to date, it is only applied to the estimation of changes of bending stiffness of beam structures. It might be appropriate to expand the local flexibility method to other type of structures such as plate structures. However, one of the main difficulties is to find the load configuration which only induces local stress within a portion of the plate structure.

The results of damage detection are always contaminated by errors caused by many reasons such as measurement noise, modelling error and numerical errors etc. Therefore, it might be appropriate to associate a uncertainty measurement with the identified damage. The confidence of the identified damage could be indicated by an index which may help increase the accuracy of judgment. For instance, when performing NPCA by training AANN with the identified stiffness variations of elements, residual error of each identified stiffness variation could be weighted according to the corresponding confidence index.

The methodologies studied in this thesis focus on Level-III damage detection. Although compressive studies on the extent of errors in the identified stiffness variations using these damage identification methodologies have not been done, it seems that moderate errors are inevitable which causes damage qualification not so reliable, even in the laboratory tests. However, while efforts are devoted for Level-III damage detection, the reliability of Level-I and Level-II damage detection might also increase. Knowing the existing of damage and possible locations of damage has already contributed critical information for structural health monitoring purpose. Detail examination can be conducted to find exact location and severity of the damage of a structure. Therefore, more efforts are required to develop approaches to increase the reliability of Level-III damage detection. Specially, there are few literatures studying the environmental effects on the identified elemental stiffness variations in a real structure under long term continuous monitoring. For practical application purpose, further studies are necessary to verify existing Level-III damage detection algorithms on real structures under varying environmental conditions in a continuous way.

REFERENCE

1. Akaike H., (1974) "A new look at the statistical model identification." *IEEE Transactions on Automatic Control*, 19, 716-723.
2. Aktan A.E., Lee K.L., Chuntavan C., Aksel T., (1994) "Modal testing for structural identification and condition assessment of constructed facilities," *Proceedings of 12th International Modal Analysis Conference*, Honolulu, HI, pp.462–468.
3. Allemang R. J., (1980) *Investigation of Some Multiple Input/Output Frequency Response Function Experimental Modal Analysis Techniques.* Doctor of Philosophy Dissertation, University of Cincinnati, Department of Mechanical Engineering, pp. 141-214.
4. Alampalli S., (1998) "Influence of in-service environment on modal parameters." *Proceedings of the 16th International Modal Analysis Conference (IMAC-XVI)*, Santa Barbara, California, 1, 111–116.
5. Allemang R. J., (1999) *Vibrations: Experimental Modal Analysis*, Course Notes, Seventh Edition, Structural Dynamics Research Laboratory, University of Cincinnati, OH.
6. Araujo dos Santos J. V., Mota Soares C. M., Mota Soares C. A., Maia N. M. M., (2005) "Structural damage identification in laminated structures using FRF data." *Composite Structures*, 67, 239-249.
7. Askegaard V. and Mossing P., (1988) "Long term observation of RC-bridge using changes in eigenfrequencies." *Nordic Concrete Research*, 7, 20-27.
8. Bendat J. S. and Piersol A. G., (1980) *Engineering Applications of Correlation and Spectral Analysis*. Wiley, New York.
9. Bernal D., (2002) "Load Vectors for Damage Localization," *Journal of Engineering Mechanics*, Vol. 128, No. 1, pp. 7-14.
10. Caicedo J. M., (2003) *Structural health monitoring of flexible civil structures.* PhD Thesis, Washington University
11. Caicedo J.M., Dyke S.J., Johnson E.A., (2004) "NExT and ERA for phase I of the IASC-ASCE benchmark problem." *Journal of Engineering Mechanics (ASCE)*, 130(1), 49–60.
12. Carden E. P. and Paul F., (2004) "Vibration Based Condition Monitoring: A Review," *Structural Health Monitoring*, 3(4), 335-377.
13. Chang C. P., Flatau A. and Liu S. C., (2003) "Review Paper: Health Monitoring of Civil Infrastructure," *Structural Health Monitoring*, 2(3), 257-267.
14. Cybenko G., (1989) "Approximation by superpositions of a sigmoidal function." *Math. Control Signals System*, 2, 303–14.
15. Doebling S. W., Farrar C. R., Prime M. B., and Shevitz D. W., (1996) *Damage identification and health monitoring of structure and mechanical systems from changes in their vibration characteristics: A literature review.* Research Rep. No. LA-13070-MS, ESA-EA, Los Alamos National Laboratory, Los Alamos, N.M.
16. Doebling S. W., Hemez F. M., Peterson L. D., and Farhat C. (1997). "Improved damage location accuracy using strain energy based on mode selection criteria." *AIAA J.*, 35(4), 693–699.
17. Ewins D. J., (2000) *Modal Testing: Theory, Practice and Application.* Research Studies Press, Baldock, Hertfordshire, UK.
18. Farrar C.R. and Doebling S.W., (1999) Damage detection II: field applications to large structures. In: Silva, J.M.M. and Maia, N.M.M. (eds.), *Modal Analysis and*

Testing, Nato Science Series. Dordrecht, Netherlands: Kluwer Academic Publishers.

19. Fox R. L., and Kapoor M. P., (1968) "Rates of Change of Eigenvalues and Eigenvectors," *AIAA J.*, 6(12), 2426-2429.

20. Friswell M.I. and Penny J.E.T., (1997) "Is damage location using vibration measurements practical?" In: *Structural Damage Assessment Using Advanced Signal Processing Procedures, Proceedings of DAMAS'97*, University of Sheffield, UK, Sheffield Academic Press Ltd., pp. 351–362.

21. Fritzen C.P. and Jennewein D. (1998). "Damage detection based on model updating methods," *Mechanical Systems and Signal Processing*, 12(1), 163–186.

22. Furukawa A., Kiyono J., Iemura H. and Otsuka H., (2005) "Damage identification method using harmonic excitation force considering both modelling and measurement errors." *Earthquake Engineering and Structural Dynamics*, 34,1285-1304.

23. Giraldo D. F., (2006) *A Structural Health Monitoring Framework for Civil Structures*, PhD Thesis, Washington University.

24. Giraldo D. F., Dyke S. J., Caicedo J. M., (2006) "Damage detection accommodating varying environmental conditions." *Structural Health Monitoring*, 5, 155-172.

25. Guyan R., (1965), "Reduction of Mass and Stiffness Matrices." *AIAA Journal*, Vol. 3, pp. 380.

26. Hermans L., and Van der Auweraer H., (1999) "Modal testing and analysis of structures under operational conditions: industrial applications," *Mech. Syst. Signal Process.*, 13, No. 2, pp. 193–216.

27. Heylen W., Lammens S., and Sas P., (1997) *Modal analysis theory and testing.* Department of Mechanical Engineering, Katholieke Universiteit Leuven, Leuven, Belgium.

28. Holland J., (1975) *Adaptation in Natural and Artificial Systems*, University of Michigan Press, Ann Arbor, MI.

29. Hsu T.Y. and Loh C.H., (2008) "Damage Diagnosis of Frame Structures Using Modified Modal Strain Energy Change Method", Journal of Engineering Mechanics, Vol.134, No.11, pp.1000-1012. [SCI,EI]

30. Hsu T. Y. and Loh C. H., (2009) "Damage detection using frequency response functions under ground excitation." *Proc. of the 16th Int'l SPIE Symposium on Smart Structures and Materials and Nondestructive Evaluation and Health Monitoring*, March 2009, San Diego, CA, USA.

31. Hsu T.Y. and Loh C.H., (2010) "Damage Detection Accommodating Nonlinear Environmental Effects by Nonlinear Principal Component Analysis", Journal of Structural Control & Health Monitoring, Vol. 17, Issue 3, pp. 338-354. [SCI,EI]

32. Juang J.N., (1996) *Applied System Identification*. Prentice-Hall, Englewood Cliffs,

33. Kidder R., (1973) "Reduction of Structural Frequency Equations." *AIAA Journal*, Vol. 11, No. 6.

34. Kim C.Y. Jung D.S. Kim N.S. & Yoon J.G., (1999) "Effect of vehicle mass on the measured dynamic characteristics of bridges from traffic-induced test." *Proceedings of the 19th International Modal Analysis Conference (IMAC XIX)*, Kissimmee, FL, pp.1106-1110

35. Kramer M.A., (1991) "Nonlinear principal component analysis using auto-associative neural networks." *AIChE Journal*, 37, 233–243.

36. Kullaa J., (2001) "Elimination of environmental influences from damage-sensitive features in a structural health monitoring system." in: Fu-Kuo Chang (Ed.), *Structural Health Monitoring—the Demands and Challenges*, CRC Press, Boca

Raton, FL, 742–749.

37. Lee U. and Shin J., (2002) "A frequency-domain method of structural damage identification formulated from the dynamic stiffness equation of motion." *Journal of Sound Vibration*, 257(4), 615-634.

38. Lim T. W., and Kashangaki T. A. L., (1994) "Structural damage detection of space truss structures using best achievable eigenvectors." *AIAA J.*, 32(5), 1049–1057.

39. Lin R. M. and Ewins D. J., (1994) "Analytical model improvement using frequency response functions." *Mechanical Systems and Signal Processing*, 8(4), 437-458.

40. Lu K.C., Loh C.H., Yang J.N., Lin P.Y., (2008) "Decentralized Sliding Mode Control of Building Using MR-Dampers," *Smart Material and Structures*, 17(5), 055006.

41. Lu K.C., Loh C.H., Yang Y.S., Lynch J.P., Law K. HJ., (2008) "Real-time structural damage detection using wireless sensing and monitoring system," Smart Structures and Systems, Vol. 4, No. 6, 759-778.

42. Lynch J. P. and Loh K. J., (2006) "A Summary Review of Wireless Sensors and Sensor Networks for Structural Health Monitoring," *The Shock and Vibration Digest*, 38(2), 91-128.

43. Manson G., (2002) "Identifying damage sensitive, environmental insensitive features for damage detection." *In 3rd Int. Conf. Identification in Engineering Systems*, University of Wales Swansea, UK.

44. Mayes R.L., (1995) "An experimental algorithm for detecting damage applied to the i-40 bridge over the Rio Grande," *Proceedings of the 13th International Modal Analysis Conference*, Nashville, TN, February 13–16, pp.219–225.

45. Marple Jr. S.L., (1987) *Digital Spectral Analysis with Applications*. Prentice Hall, Englewood Cliffs, Chapter 8.

46. Orfanidis S.J., (1996) *Optimum Signal Processing: An Introduction*. 2nd Edition, Prentice-Hall, Englewood Cliffs, NJ.

47. O'Callahan J., Avitabile P. and Riemer R., (1989) "System Equivalent Reduction Expansion Process (SEREP)," *IMAC VII*, pp. 29–37.

48. Pandey A.K., Biswas M. and Samman M.M., (1991) "Damage detection from changes in curvature mode shapes," *Journal of Sound and Vibration*, 145(2), 321–332.

49. Peeters B. and De Roeck G., (2001) "One-year monitoring of the Z24-Bridge: environmental effects versus damage events." *Earthquake Engineering and Structural Dynamics*, 30, 149-171.

50. Peeters B. and Ventura C. E., (2003) "Comparative Study of Modal Analysis Techniques for Bridge Dynamic Characteristics," *Mechanical Systems and Signal Processing*, 17(5), 965-988.

51. Ren W. X. and Roeck G. D., (2002) "Discussion of "Structural damage detection from elemental modal strain energy change" by Z. Y. Shi. S. S. Law, and L. M. Zhang." *J. Eng. Mech.*, Vol. 128, No. 3, 376–377.

52. Reynders E. and De Roeck G., (2008) "The Local Flexibility Method for Vibration-based Damage Localization and Quantification." *In Proceedings of the 26th International Modal Analysis Conference (IMCA XXVI)*, Orlando, FL, February 4~7.

53. Reynders E. and De Roeck G., (2010) "A Local Flexibility Method for Vibration-based Damage Localization and Quantification." *Journal of Sound and Vibration*, Volume 329, Issue 12, pp. 2367-2383.

54. Ricles J. M., and Kosmatks J. B., (1992) "Damage detection in elastic structures

using vibratory residual forces and weighted sensitivity." *AIAA J.*, 30(9), 2310–2316.

55. Rohrmann R.G., Baessler M., Said S., Schmid W., Ruecker W.F., (2000) "Structural causes of temperature affected modal data of civil structures obtained by long time monitoring." *Proceedings of the 18th international modal analysis conference*, Sun Antinio, TX, USA, 1–7.

56. Rushton A, Pearson A.J., Roberts G.P., (1999) *Brite-EuRam project SIMCES, task 1, environmental monitoring of Z24-Bridge*. Technical Report AM3548/R004, WS Atkins, Bristol, UK.

57. Rytter A. (1993) *Vibration based inspection of civil engineering structures*. PhD. Thesis, Alborg University, Denmark.

58. Shi Z. Y., Ding X. H., and Gu H. Z., (1995) "A new model reduction and expansion method." *Proc., Int. Conf. on Struct. Dyn., Vibration, Noise and Control*, 847–852.

59. Shi Z. Y., Law S. S., and Zhang L. M., (1998) "Structural damage localization from modal strain energy change." *J. Sound Vib.*, 218(5), 825–844.

60. Shi Z. Y., Law S. S., and Zhang L. M., (2000) "Structural damage detection from elemental modal strain energy change." *J. Eng. Mech.*, 126(12), 1216–1223.

61. Shi Z. Y., Law S. S., and Zhang L. M., (2002) "Improved Damage Quantification from Elemental Modal Strain Energy Change." *J. Eng. Mech.*, 128(5), 521–529.

62. Sohn H., Dzwonczyk M., Straser E.G., Kiremidjian A.S., Law K.H., Meng T., (1999) "An experimental study of temperature effect on modal parameters of the Alamosa Canyon Bridge." *Earthquake Engineering and Structural Dynamics*, 28, 879–897.

63. Sohn H., Worden K., Farrar C.F., (2001) "Novelty detection under changing environmental conditions." *SPIE's Eighth Annual International Symposium on Smart Structures and Materials*, Newport Beach, CA. (LA-UR-01-1894).

64. Sohn H., Farrar C.R., Hemez F.M., Shunk D.D., Stinemates D.W., Nadler B.R., (2004) "A review of structural health monitoring literature: 1996–2001", *Report LA-13976-MS*, Los Alamos National Laboratory, Los Alamos, NM.

65. Sohn H., Park G., Wait J. R., Limback N. P. & Farrar C. R., (2003) "Wavelet-based active sensing for delamination detection in composite structures." *Smart Mater. Struct.* 13, 153–160.

66. Stubbs N., and Kim J. T., (1996). "Damage localization in structures without base-line modal parameters." *AIAA J.*, 34(8), 1644–1649.

67. Toksoy T. and Aktan A.E., (1994) "Bridge-condition assessment by modal flexibility, *Experimental Mechanics*, 34(3), 271–278.

68. Teughels A., De Roeck G., Suykens J.A.K., (2003) "Global optimization by coupled local minimizers and its application to FE model updating," *Computers and Structures*, 81 (24–25), 2337–2351.

69. Thomas R. S., Charles J. C. Joanne L. W. Howard M. A. (1988). "Comparison of Several Methods for Calculating Vibration Mode Shape Derivatives." *AIAA J.*, 26(12), 1506–1511.

70. Van Overschee P. and De Moor B., (1996) *Subspace Identification for Linear Systems: Theory - Implementation - Applications*, Kluwer Academic Publishers, Dordrecht, The Netherlands.

71. Wahab M.M.A. and De Roeck G., (1999) "Damage detection in bridges using modal curvatures: applications to a real damage scenario," *Journal of Sound and Vibration*, 226(2), 217–235.

72. Wang Y., Lynch J.P. and Law K.H., (2005) "Wireless structural sensors using reliable communication protocols for data acquisition and interrogation,"

Proceedings of the 23rd International Modal Analysis Conference (IMAC XXIII), Orlando, FL, January 31 - February 3.

73. Wang Y., (2007) *Wireless Sensing and Decentralized Control for Civil Structures: Theory and Implementation*. Ph. D. Thesis, Stanford University.

74. Wang Z., Lin R. M., Lim M. K., (1997) "Structural damage detection using measured FRF data." *Computer Methods in Applied Mechanics and Engineering*, 147, 187-197

75. Watson D.K. and Rajapakse R.K.N.D., (2000) "Seasonal variation in material properties of a flexible pavement." *Canadian Journal of Civil Engineering*, 27(1), 44-54.

76. Weng J.H., Loh C.H., Lynch J.P., Lu K.C., Lin P.Y., Wang Y., (2008) "Output-Only Modal Identification of a Cable-Stayed Bridge Using Wireless Monitoring Systems," *J. of Engineering Structure*, 30 (2), 1802-1830.

77. Weng J.H., (2010) *Application of Subspace Identification in System Identification and Structural Damage Detection*, Ph.D. Dissertation, National Taiwan University.

78. Wood M. G., (1992) *Damage analysis of bridge structures using vibrational techniques*. PhD. Thesis, Department of Mechanical and Electrical Engineering, University of Aston, Birmingham, UK.

79. Xia Y., Hao H., Zanardo G., Deeks A., (2006) "Long term vibration monitoring of an RC slab: Temperature and humidity effect." *Engineering Structures*, 28, 441-452.

80. Xiao H., Bruhns O. T., Waller H. Meyers A., (2001) "An input/output-based procedure for fully evaluating and monitoring dynamic properties of structural systems via a subspace identification method." *Journal of Sound and Vibration*, 246(4), 601-623.

81. Yan A.M., Kerschen G., De Boe P., Golinval J.C., (2005a) "Structural damage diagnosis under changing environmental conditions—Part I: A linear analysis." *Mechanical Systems and Signal Processing*, 19, 847-864.

82. Yan A.M., Kerschen G., De Boe P., Golinval J.C. (2005b) "Structural damage diagnosis under changing environmental conditions—Part II: local PCA for non-linear cases." *Mechanical Systems and Signal Processing*, 19, 865-880.

83. Zhang Z. and Aktan A.E. (1995) "The damage indices for the constructed facilities," *Proceedings of the 13th International Modal Analysis Conference*, Nashville, TN, February 13–16, pp.1520–1529.

CURRICULUM VITAE

Personal data

Ting-Yu Hsu   Born in Taipei, Taiwan, ROC., January 14, 1975

Education

1990-1993   Taipei Municipal Jianguo High School

1993-1997   Bachelor Degree of Civil Engineering, National Cheng Kung University

1997-1999   Master Degree in Structural Division of Construction Engineering, National Taiwan University of Science and Technology

Work

2000-2010   Assistant Research Fellow, National Center for Research on Earthquake Engineering

1999-2010   Visiting Scholar, Structural Mechanics Division of Department of Civil Engineering, K.U. Leuven, Belgium

Certification

1997   Structural Engineer, Taiwan, ROC.

2001   Civil Engineer, Taiwan, ROC.

Journal paper

1. Loh C.H., Hsu T.Y. and Chen C.H., "Application of Advanced Statistical Methods for Extracting Long-term Trends in Static Monitoring Data from A Arch Dam" , *Structural Health Monitoring*, (Accepted).
2. Hsu T.Y. and Loh C.H., (2010) "Damage Detection Accommodating Nonlinear Environmental Effects by Nonlinear Principal Component Analysis", *Journal of Structural Control & Health Monitoring*, Vol. 17, Issue 3, pp. 338-354. [SCI,EI]
3. Hsu T.Y. and Loh C.H., (2008) "Damage Diagnosis of Frame Structures Using Modified Modal Strain Energy Change Method", *Journal of Engineering Mechanics*, Vol.134, No.11, pp.1000-1012. [SCI,EI]
4. Hwang J.S. and Hsu T.Y., (2001) "A Fractional Derivative Model to Include Effect of Ambient Temperature on HDR Bearings." *Engineering Structures, the Journal of Earthquake, Wind and Ocean Engineering*, Vol. 23, No. 5, pp.484-490. [SCI,EI]
5. Hwang J.S. and Hsu T.Y., (2000) "Experimental Study of An Isolated Building Subjected to Tri-Axial Ground Motions." *Journal of Structural Engineering, ASCE*, Vol. 126, No. 8, pp. 879-886. [SCI,EI]